



National Library
of Canada

Acquisitions and
Bibliographic Services Branch

395 Wellington Street
Ottawa, Ontario
K1A 0N4

Bibliothèque nationale
du Canada

Direction des acquisitions et
des services bibliographiques

395, rue Wellington
Ottawa (Ontario)
K1A 0N4

Your file *Votre référence*

Our file *Notre référence*

NOTICE

The quality of this microform is heavily dependent upon the quality of the original thesis submitted for microfilming. Every effort has been made to ensure the highest quality of reproduction possible.

If pages are missing, contact the university which granted the degree.

Some pages may have indistinct print especially if the original pages were typed with a poor typewriter ribbon or if the university sent us an inferior photocopy.

Reproduction in full or in part of this microform is governed by the Canadian Copyright Act, R.S.C. 1970, c. C-30, and subsequent amendments.

AVIS

La qualité de cette microforme dépend grandement de la qualité de la thèse soumise au microfilmage. Nous avons tout fait pour assurer une qualité supérieure de reproduction.

S'il manque des pages, veuillez communiquer avec l'université qui a conféré le grade.

La qualité d'impression de certaines pages peut laisser à désirer, surtout si les pages originales ont été dactylographiées à l'aide d'un ruban usé ou si l'université nous a fait parvenir une photocopie de qualité inférieure.

La reproduction, même partielle, de cette microforme est soumise à la Loi canadienne sur le droit d'auteur, SRC 1970, c. C-30, et ses amendements subséquents.

Canada

Determination of the Relationship Between
Thermal Contact Resistance and Contact Pressure
Based on Their Distributions

by

Wei Li

This thesis is submitted to the Faculty of Graduate Studies and Research in partial fulfillment of the requirements for the Master of Engineering degree.

Department of Mechanical Engineering
McGill University
Montréal, Québec, Canada

© Wei Li, Montréal, Canada, November 1993.



National Library
of Canada

Bibliothèque nationale
du Canada

Acquisitions and
Bibliographic Services Branch

Direction des acquisitions et
des services bibliographiques

395 Wellington Street
Ottawa, Ontario
K1A 0N4

395, rue Wellington
Ottawa (Ontario)
K1A 0N4

Your file *Votre référence*

Our file *Notre référence*

THE AUTHOR HAS GRANTED AN IRREVOCABLE NON-EXCLUSIVE LICENCE ALLOWING THE NATIONAL LIBRARY OF CANADA TO REPRODUCE, LOAN, DISTRIBUTE OR SELL COPIES OF HIS/HER THESIS BY ANY MEANS AND IN ANY FORM OR FORMAT, MAKING THIS THESIS AVAILABLE TO INTERESTED PERSONS.

L'AUTEUR A ACCORDE UNE LICENCE IRREVOCABLE ET NON EXCLUSIVE PERMETTANT A LA BIBLIOTHEQUE NATIONALE DU CANADA DE REPRODUIRE, PRETER, DISTRIBUER OU VENDRE DES COPIES DE SA THESE DE QUELQUE MANIERE ET SOUS QUELQUE FORME QUE CE SOIT POUR METTRE DES EXEMPLAIRES DE CETTE THESE A LA DISPOSITION DES PERSONNE INTERESSEES.

THE AUTHOR RETAINS OWNERSHIP OF THE COPYRIGHT IN HIS/HER THESIS. NEITHER THE THESIS NOR SUBSTANTIAL EXTRACTS FROM IT MAY BE PRINTED OR OTHERWISE REPRODUCED WITHOUT HIS/HER PERMISSION.

L'AUTEUR CONSERVE LA PROPRIETE DU DROIT D'AUTEUR QUI PROTEGE SA THESE. NI LA THESE NI DES EXTRAITS SUBSTANTIELS DE CELLE-CI NE DOIVENT ETRE IMPRIMES OU AUTREMENT REPRODUITS SANS SON AUTORISATION.

ISBN 0-315-99972-1

Canada

**Relationship Between Thermal Contact
Resistance and Contact Pressure**

by

Wei Li

This thesis is submitted to the Faculty of Graduate Studies and Research in partial fulfillment of the requirements for the Master of Engineering degree.

Department of Mechanical Engineering
McGill University
Montréal, Québec, Canada

© Wei Li, Montréal, Canada, November 1993.

TO MY PARENTS AND SISTER -

for their love and understanding

Abstract

Loading conditions in a machine structure usually cause the contact pressure at the joints to take the form of a distribution, which in turn causes thermal contact resistance to be position-dependent also.

In the experiments described in this thesis, two thin-plate specimens of steel under plane-stress loading conditions generating contact pressure distributions of various profiles at the interface, were subjected to a thermal field. Temperature measurements served as reference for the finite element modelling which, through consecutive iterations, provided the values for the thermal contact resistance distributions. Combined mechanical contact pressure and thermal contact stress distributions were considered at the interface.

The function representing the relationship between thermal contact resistance and contact pressure for various distributions was defined using the least squares method. It was revealed that although this relationship can be expressed by the single function for the whole experimental range, the deviations experienced for different slopes and forms of distributions (convex and concave), particularly noticeable for steep slopes at high contact pressure levels, could indicate the effect of macro-constriction resistance, however small its values according to the theoretical calculations might be.

Résumé

Les conditions de charge dans une structure de machine font en sorte que normalement la pression de contact aux joints prenne la forme d'une distribution qui à son tour cause la résistance de contact thermique d'être dépendante de la pression.

Dans les expériences décrites dans cette thèse, deux spécimens de plaque mince en acier sous des conditions de charge planaires créant des distributions variées de pression de contact à l'interface, ont été assujettis à un champ thermique. Les mesures de température ont servi comme références pour le modèle des éléments finis, qui, par l'intermédiaire d'itérations consécutives, a fourni les valeurs pour les distributions de résistance au contact thermique. Une combinaison des distributions de pression de contact mécanique et de contrainte de contact thermique a été considérée à l'interface.

La fonction qui représente la relation entre la résistance de contact thermique et la pression de contact pour diverses distributions a été définie en utilisant la méthode des moindres carrés. Il a été révélé que même si la relation peut être exprimée par une fonction simple pour toute la gamme expérimentale, les déviations expérimentées pour les différentes pentes et formes de distribution (concave ou convexe), particulièrement pour des pentes escarpées à un haut niveau de pression de contact, peut indiquer l'effet de résistance de macro-constriction, même pour des petites valeurs en accord avec les calculs théoriques.

Statement of Originality and Contribution to Knowledge

The author of this thesis claims originality for the following contributions to the understanding of the effect of contact pressure distribution on thermal contact resistance distribution, and to the method by which the latter is determined:

1. Formulation of the relationship between the thermal contact resistance and contact pressure for their various distributions, expressed by the single function, the deviations from which, experienced for different slopes and forms of distributions (convex and concave), could indicate the effect of macro-constriction resistance.

The function was defined for specimens of specific material, surface roughness and interface size.

2. Extension of analytical and numerical approaches used to determine thermal contact resistance and thermal contact conductance in one-dimensional experiments, to a two-dimensional case, where an iterative experimental and finite element modelling data correlation provided the values of thermal contact resistance distribution along the interface. This approach permitted also to define the distribution of thermal contact resistance as a function of contact pressure which combines both mechanical contact pressure and thermal contact stress distributions.

Present approach may also be applied to determine the thermal contact resistance distribution in a three-dimensional case.

Acknowledgements

The author wishes to express his deep gratitude and appreciation to his research supervisor, Professor L. Kops, for his thoughtful suggestions and constructive guidance, and for his continuous encouragement throughout the course of this research.

The author is deeply grateful to Professor R. Baliga for the fruitful discussions and valuable suggestions, and for the technical support obtained from his Heat Transfer Laboratory. Sincere thanks go to Dr. M. H. Attia for his constructive comments and helpful discussions on various aspects of this research.

Thanks are also due to Mr. A. Clement and his colleagues for machining the test pieces, as well as to Mr. J. Kelly, Mr. G. Dedic and Mr. G. Tewfik for providing necessary instruments for the experiments.

A debt of gratitude is owed to Mr. N. Stathopoulos for his kind help on the thermocouple calibration, to Mr. B. Tian and Ms. M. Nixon for their suggestions on the use of computer software, and to Mr. G. Jaar for his help on the French translation of the abstract. The author is grateful to Ms. M. Gordon for her diligence in proof reading, and to Ms. M. Nixon for a thorough linguistic review of the text.

Contents

Abstract	ii
Résumé	iii
Statement of Originality and Contribution to Knowledge	iv
Acknowledgements	v
List of Figures	vii
List of Tables	xi
Nomenclature	xv
1 Introduction	1
1.1 The Role of Contact Pressure and Thermal Contact Resistance Distributions in Fixed Joints on Thermal Deformation of Machine Tools	1
1.2 Outline of the Thesis	3
2 Thermal and Mechanical Behaviour of a Machine Joint	5
2.1 Thermal Contact Resistance Distribution along the Machine Joint	5
2.2 Nonuniformity of the Contact Pressure Distribution along the Machine Joint	8

CONTENTS

vii

2.3	Review of Previous Work	10
3	Experiment	15
3.1	Objective and Approach	15
3.2	Generation of Nonuniform Contact Pressure Distribution	17
3.3	The Distribution, Calibration and Installation of the Thermocouples .	19
3.4	Experimental Apparatus	22
3.5	Experimental Procedure	24
4	Finite Element Analysis	26
4.1	Objective and Approach	26
4.2	Introduction to ALGOR	27
4.3	Creating the Finite Element Model	29
4.4	FEA Determination of the Thermal Conductivity and Pressure Distri- butions	32
5	Results and Discussion	37
6	Conclusions and Recommendations	49
6.1	Conclusions	49
6.2	Recommendations for Future Studies	51
	References	52
A	Figures	56
B	Tables	97

List of Figures

1.1	Schematic representation of the time-dependent closed-loop interaction at machine joint [3].	56
2.1	Contact configuration and heat flow constriction across the joint.	57
2.2	Temperature distribution across the interface.	57
2.3	Representation of the disc-constriction model: a - bodies in real contact; b - idealized unit cell; c - thermal boundary conditions [14].	58
3.1	Contact pressure distributions along the interface with different h/ℓ ratios.	58
3.2	Experimental thermocouple distribution for $h/\ell = 0.5$	59
3.3	Experimental thermocouple distribution for $h/\ell = 2.0$	60
3.4	Schematic representation of the test rig.	61
3.5	Side view of the test rig.	62
4.1	Schematic representation of the closed-loop computer iteration	63
4.2	Finite element analysis procedure in ALGOR	64
4.3	Finite element model for $h/\ell = 0.5$	65
4.4	Finite element model for $h/\ell = 2.0$	66

4.5	Model of one-dimensional channel temperature distribution across the interface.	67
5.1	Temperature field on the finite element model for $h/\ell = 0.5$ $F = 294$ N.	68
5.2	Temperature field on the finite element model for $h/\ell = 2.0$ $F = 294$ N.	69
5.3	Interface area of finite element model.	70
5.4	Mechanical contact pressure distribution along the half-length interface from the axis of symmetry for $h/\ell = 0.5$	71
5.5	Mechanical pressure distribution along the half-length interface from the axis of symmetry for $h/\ell = 2.0$	72
5.6	Close view of the stress field of the interface area for $h/\ell = 0.5$	73
5.7	Close view of the stress field of the interface area for $h/\ell = 2.0$	74
5.8	Combined (mechanical and thermal) contact pressure distribution along the half-length interface from the axis of symmetry for $h/\ell = 0.5$	75
5.9	Combined (mechanical and thermal) contact pressure distribution along the half-length interface from the axis of symmetry for $h/\ell = 2.0$	76
5.10	Comparison of combined contact pressure distribution and mechanical-only pressure distribution $h/\ell = 0.5$	77
5.11	Comparison of combined contact pressure distribution and mechanical-only pressure distribution $h/\ell = 2.0$	78
5.12	Thermal stress distribution along the half-length interface from the axis of symmetry $h/\ell = 0.5$	79
5.13	Thermal stress distribution along the half-length interface from the axis of symmetry $h/\ell = 2.0$	80

5.14	Thermal conductivity distribution in the disturbed zone for $h/\ell = 0.5$.	81
5.15	Thermal conductivity distribution in the disturbed zone for $h/\ell = 2.0$.	82
5.16	Thermal contact resistance distribution along the half-length interface from the axis of symmetry for $h/\ell = 0.5$.	83
5.17	Thermal contact resistance distribution along the half-length interface from the axis of symmetry for $h/\ell = 2.0$.	84
5.18	Thermal contact resistance distribution and combined contact pressure distribution for $h/\ell = 0.5$ $F = 98$ N.	85
5.19	Thermal contact resistance distribution and combined contact pressure distribution for $h/\ell = 0.5$ $F = 294$ N.	86
5.20	Thermal contact resistance distribution and combined contact pressure distribution for $h/\ell = 0.5$ $F = 882$ N.	87
5.21	Thermal contact resistance distribution and combined contact pressure distribution for $h/\ell = 2.0$ $F = 98$ N.	88
5.22	Thermal contact resistance distribution and combined contact pressure distribution for $h/\ell = 2.0$ $F = 294$ N.	89
5.23	Thermal contact resistance distribution and combined contact pressure distribution for $h/\ell = 2.0$ $F = 882$ N.	90
5.24	Relationship between the thermal contact resistance and the contact pressure for convex contact pressure distributions, $h/\ell = 0.5$.	91
5.25	Relationship between the thermal contact resistance and the contact pressure for concave contact pressure distributions, $h/\ell = 2.0$.	92
5.26	General relationship between the thermal contact resistance and the contact pressure for convex and concave pressure distributions.	93

LIST OF FIGURES

5.27	General relationship in log-log coordinates.	94
5.28	Profile of the contact surface.	95
5.29	Graph of thermal contact conductance vs. contact pressure in [19] with added general functions obtained in this study.	96

List of Tables

3.1	Calibration results of the thermocouples (TC) on upper specimen for $h/\ell = 0.5$;	97
3.2	Calibration results of the thermocouples (TC) on upper specimen for $h/\ell = 2.0$;	98
3.3	Calibration results of the thermocouples (TC) on lower specimen . . .	99
5.1	Experimental temperatures on upper specimen, $h/\ell = 0.5$, $F = 98 N$;	100
5.2	Experimental temperatures on lower specimen, $h/\ell = 0.5$, $F = 98 N$;	101
5.3	Experimental temperatures on upper specimen, $h/\ell = 0.5$, $F = 294 N$;	102
5.4	Experimental temperatures on lower specimen, $h/\ell = 0.5$, $F = 294 N$;	103
5.5	Experimental temperatures on upper specimen, $h/\ell = 0.5$, $F = 882 N$;	104
5.6	Experimental temperatures on lower specimen, $h/\ell = 0.5$, $F = 882 N$;	105
5.7	Experimental temperatures on upper specimen, $h/\ell = 2.0$, $F = 98 N$;	106
5.8	Experimental temperatures on lower specimen, $h/\ell = 2.0$, $F = 98 N$;	107
5.9	Experimental temperatures on upper specimen, $h/\ell = 2.0$, $F = 294 N$;	108
5.10	Experimental temperatures on lower specimen, $h/\ell = 2.0$, $F = 294 N$;	109
5.11	Experimental temperatures on upper specimen, $h/\ell = 2.0$, $F = 882 N$;	110
5.12	Experimental temperatures on lower specimen, $h/\ell = 2.0$, $F = 882 N$;	111

5.13	Temperature distribution below the heating surface, $h/\ell = 0.5$;	112
5.14	Temperature distribution below the heating surface, $h/\ell = 2.0$;	112
5.15	Temperature drop caused by the interface, $h/\ell = 0.5$;	113
5.16	Temperature drop caused by the interface, $h/\ell = 2.0$;	113
5.17	Mechanical contact pressure distribution of nodes along the interface, $h/\ell = 0.5$;	114
5.18	Mechanical contact pressure distribution of nodes along the interface. $h/\ell = 2.0$;	114
5.19	Mechanical contact pressure distribution of elements along the inter- face, $h/\ell = 0.5$;	114
5.20	Mechanical contact pressure distribution of elements along the inter- face, $h/\ell = 2.0$;	114
5.21	Combined mechanical and thermal contact pressure distribution of nodes along the interface, $h/\ell = 0.5$;	115
5.22	Combined mechanical and thermal contact pressure distribution of nodes along the interface, $h/\ell = 2.0$;	115
5.23	Combined mechanical and thermal contact pressure distribution of el- ements along the interface, $h/\ell = 0.5$;	115
5.24	Combined mechanical and thermal contact pressure distribution of el- ements along the interface, $h/\ell = 2.0$;	115
5.25	Thermal stress distribution of elements along the interface, $h/\ell = 0.5$;	116
5.26	Thermal stress distribution of elements along the interface, $h/\ell = 2.0$;	116
5.27	The effect of thermal stress on mechanical pressure along the interface, $h/\ell = 0.5$;	116

5.28	The effect of thermal stress on mechanical pressure along the interface, $h/\ell = 2.0$;	116
5.29	First assumption of thermal conductivity distribution along the inter- face, $h/\ell = 0.5$;	117
5.30	First assumption of thermal conductivity distribution along the inter- face, $h/\ell = 2.0$;	117
5.31	Thermal conductivity distribution along the interface, $h/\ell = 0.5$; . . .	117
5.32	Thermal conductivity distribution along the interface, $h/\ell = 2.0$; . . .	117
5.33	Thermal contact resistance distribution along the interface, $h/\ell = 0.5$;	118
5.34	Thermal contact resistance distribution along the interface, $h/\ell = 2.0$;	118

Nomenclature

Symbol	Description
a	Parameter of general curve fitting function
A_a	Apparent contact area, mm^2
b	Parameter of general curve fitting function
c	Distance between thermocouples, mm
C	Proportional coefficient
d	Depth of the disturbed zone along the interface, mm
D	Diameter of thermocouple installation hole, mm
E	Young's modulus, kPa
F	Concentrated load, N
F_u	Distributed load, N
g	Temperature gradient of the undisturbed temperature field, $^{\circ}C/mm$
h_c	Thermal conductance, $W/m^2 \text{ } ^{\circ}C$
h/ℓ	Height-to-length ratio of specimen
H_B	Brinell hardness
I	Moment of inertia, m^4
k	Thermal conductivity, $W/m \text{ } ^{\circ}C$
k_f	Modulus of foundation, kPa/m
ℓ	Length of the contact, mm
L	Length of the half interface, mm

M_0	Bending moment, Nm
p	Uniformly distributed loading, kPa
p_a	Apparent contact pressure, kPa
p_c	Contact pressure, kPa
p_{mech}	Mechanical contact pressure, kPa
P	Concentrated loading over a machine joint, N
q	Heat flux, kW/m^2
Q	Heat flow rate, kW
r	Radius of curvature of the surface asperity, μm
r_c	Average radius of micro-contact, μm
R	Thermal resistance of the disturbed zone, $m^2 \text{ }^\circ C/kW$
R_a	Average roughness of the surface, μm
R_c	Thermal contact resistance, $m^2 \text{ }^\circ C/kW$
R_1	Local microscopic thermal contact resistance, $m^2 \text{ }^\circ C/kW$
R_2	Local macroscopic thermal contact resistance, $m^2 \text{ }^\circ C/kW$
R_f	Local thermal resistance of surface film, $m^2 \text{ }^\circ C/kW$
R_i	Local thermal resistance of interstitial medium, $m^2 \text{ }^\circ C/kW$
s_{th}	Thermal stress, kPa
T	Temperature, $^\circ C$
T_a	Temperature above the disturbed zone, $^\circ C$
T_b	Temperature below the disturbed zone, $^\circ C$
ΔT	Temperature drop, $^\circ C$
$\Delta T'$	Average temperature drop along the centre line, $^\circ C$
$(\Delta T)_i$	Pseudo temperature drop at the interface, $^\circ C$

$y(x)$	Profile of the deflection of the beam, μm
α_c	Thermal expansion coefficient, $^{\circ}C^{-1}$
α_d	Diffusivity, m^2/s
ρ	Density, kg/m^3
ν	Poisson Ratio
Φ	The effect of the thermal stress on the mechanical pressure distribution
σ_c	Standard deviation of contacting surface, μm
$\tan \Theta$	Mean absolute slope of surface irregularities
λ	Standard characteristic of system, $\lambda = \sqrt{\frac{k_f}{4EI}}$

Chapter 1

Introduction

1.1 The Role of Contact Pressure and Thermal Contact Resistance Distributions in Fixed Joints on Thermal Deformation of Machine Tools

One of the most important aspects of the performance of machine tools is the accuracy which depends on the relative position of the cutting tool and the workpiece. The relative position is subject to undesired changes caused by the deformation of one or several structural elements of the machine tool.

Deformation of machine tool structures is a result of both the mechanical and the thermal loading. As pointed out by Zawistowski [1], under certain working conditions thermal deformation of machine tools may contribute to more than 50% of the machining error.

Heat sources which cause the thermal deformation in the machine tool structure can be classified into two groups: internal and external sources. The internal sources are various elements of the drive and power transmission system (e.g., motors, gears,

bearings, pumps, hydraulic oil, etc.) as well as the machining process itself. It has been indicated by Spur [2], that more than 60% of the electrical energy fed into a centre lathe is transformed into heat energy within the drive and power transmission system. Heat received from external sources is in the form of radiation or convection. The latter is due to the air current and instability in the temperature of the workshop environment.

While the internal heat sources are always inherent to the machine tool operation, the external sources are independent of the machine tool; hence, they can generally be controlled in such a way that they will play an insignificant role in the thermal deformation of the structure.

In the studies on the thermal deformation of machine tool structures, the role of the fixed joint is considered to be very important. The two contact elements of the joint interact thermally and mechanically. The interaction represents both mechanical and thermal loading. Thermal interaction can be seen as a heat transfer which is affected by the conditions at the interface. The joint acts both as a heat source for one element and a heat sink for the other. In fact, the thermal field depends substantially on the distribution of heat flux along the joint. The local values of heat flux depend on the distribution of the thermal contact resistance, which is affected by the contact pressure distribution along the joint. Thermally deformed structural elements caused by thermal stresses at the joint will modify existing contact pressure distribution. As a result, the distribution of the thermal contact resistance changes and a new heat flux distribution is in effect. This cycle will be repeated as many times as is required to reach the equilibrium state of the system.

The mutual thermal and mechanical interaction of contact elements underlines the importance of the role the joint plays in thermal deformation of machine tools. This role is expressed by the concept of the time-dependent closed-loop which was first recognized by Attia and Kops [3]. This loop consists of the following elements:

- contact pressure distribution

- thermal contact resistance distribution
- thermal deformation of contacting elements

This concept is presented in Fig. 1.1. The three basic elements of the closed loop are shown as nodes interacting in clockwise fashion. By changing the contact configuration of the interface, the contact pressure distribution affects the thermal contact resistance distribution. This configuration is defined by the micro-contacts, macro-contacts (contour area), thermal warping adjacent to the interface, and condition of the oxide film at the contact spots, as described by Attia and Kops in [4]. From Fig. 1.1, it is clearly shown that, if we want to determine the deformation of the contact elements, we must know the relationship between the contact pressure and the thermal contact resistance based on their distributions. This is the objective of the research work covered by this thesis.

1.2 Outline of the Thesis

In order to analyze the effect of contact pressure distribution on the thermal contact resistance distribution along the machine joint, it is necessary to examine the characteristics of the joint and the typical thermal and mechanical working conditions under which it functions. Chapter 2 covers these aspects. The nature of the phenomenon of thermal contact resistance and of the various variables affecting it will be discussed. The nonuniformity of the contact pressure distribution will also be described in this chapter. Chapter 2 includes a review of the available work on the problem of nonlinear thermal behaviour at a machine joint. The evaluation of the limitations imposed on both the theoretical and the experimental studies, indicates that a new accurate approach for determining the relationship between the contact pressure and the thermal contact resistance based on their distributions is required.

In Chapter 3, the experimental arrangements used to determine the temperature field under nonuniform contact pressure distribution will be discussed in detail. This

includes the nonuniform pressure distribution generation, thermocouple distribution and their calibration as well as installation, and the experimental set-up and procedure.

Chapter 4 presents the finite element analysis performed using ALGOR software. Finite element models permit:

1. To obtain the mechanical contact pressure distribution and final contact pressure distribution combined with the mechanical pressure and thermal stress distributions along the interface, for a given mechanical load and heat input.
2. To obtain through iteration, the thermal contact resistance distribution by using the temperature values obtained from the experiments.

In Chapter 5, the results from the experiments and finite element analysis will be given and discussed. The relationship between contact pressure and thermal contact resistance based on their distributions is determined by using the least squares method.

The conclusions of this thesis and recommendations for future work will be given in Chapter 6.

Chapter 2

Thermal and Mechanical Behaviour of a Machine Joint

2.1 Thermal Contact Resistance Distribution along the Machine Joint

The existence of an interface separating two elements in contact creates thermal resistance to the heat flow from one element to the other.

Because of the roughness of machined surfaces, a point-to-point contact is observed. These contact points, which are referred to as the “micro contacts”, are clustered in groups within a much smaller number of bounded zones known as the “contour areas” or the “macro contacts”, as described by Attia and Kops in [4].

Thus, the apparent contact area is composed of two groups of regions: the contact regions, where macro contact areas with a high density of micro contacts exist, and the non-contact regions.

Within the contact region, the metallic contact is influenced by the presence of

a surface film (mainly an oxide layer). The oxide layer, which is characterized by its low thermal conductivity, brittleness and high degree of roughness, constitutes an additional thermal barrier.

The interstitial medium (air or grease), which occupies the space enclosed by the profiles of the surfaces in the non-contact region, has a much lower thermal conductivity than that of the contacting solids.

Fig. 2.1 presents a case in which the heat is allowed to transfer from one structural element to another in such a way that the heat flow lines run parallel to each other and perpendicular to the nominal interface. As the heat flow lines approach the contact zone, they converge towards the least-resistance paths, i.e., the metallic contacts. This natural constriction of the flow lines gives rise to the known "constriction resistance".

The thermal constriction resistance represents the combined effect of both the local macroscopic and the microscopic constriction resistances, R_2 and R_1 respectively. The former is associated with the convergence of the flow lines towards the macro contacts (contour areas) which are distributed at discrete locations over the interface. The microscopic constriction resistance is subsequently created as the heat flow lines are squeezed again towards the micro contacts (surface asperities).

The local thermal resistances of the surface film R_f and the interstitial medium R_i form together with the thermal constriction resistance, the total local thermal contact resistance R_c .

The resultant effect of R_c on the temperature distribution in contacting elements is shown in Fig. 2.2. The temperature distribution in a plane normal to the nominal interface exhibits a "pseudo" temperature drop, $(\Delta T)_I$, which is defined as the difference between the extrapolated temperature values on either side of the interface. This drop causes the heat to flow across the thermal contact resistance R_c with a flux Q/A_a , where A_a denotes the apparent (nominal) contact area. Thus,

$$R_c = \frac{(\Delta T)_I}{Q/A_a} \quad (2.1)$$

CHAPTER 2. THERMAL AND MECHANICAL BEHAVIOUR OF A MACHINE JOINT

The thermal contact conductance h_c is defined as

$$h_c = \frac{Q/A_a}{(\Delta T)_I} \quad (2.2)$$

Therefore,

$$h_c = \frac{1}{R_c} \quad (2.3)$$

It should be mentioned that the depth of the disturbed zone (Fig. 2.2) depends on the texture of the contacting surfaces and the material properties of the contacting solids. Estimation of this depth is not available in published work on the thermal contact problem. However, as indicated in a personal communication between Attia and Yovanovich [5], for nominally flat ground surfaces, the expected depth of disturbance is in the range of 1.25 – 2.5 *mm*.

Experimental investigations carried out by Laming [6], Jakob [7] and Yovanovich [8] indicate that heat energy is transferred across the contact interface mainly by conduction through two parallel paths: the metallic contacts (the contact region) and the interstitial medium (the non-contact region). As mentioned before, the heat flow through the two paths is hindered by additional resistances connected in series: the thermal constriction resistance and the thermal resistance of the surface film layer.

The variables that affect the thermal contact resistance of the joint can, therefore, be classified into two groups:

(a) the variables which are inherent to the material of the joint, such as elasticity, the hardness of the metal, the thermal resistance of the contacting solids and the interstitial medium. Basically, these variables will not be changed with different working conditions.

(b) the variables which affect the thermal constriction resistance. These variables include the mean slope of surface asperities, the standard deviation of contacting surfaces and the pressure distribution along the joint. The first two factors are also affected by the pressure distribution. So the pressure distribution is the main effect in

this group and it is different with different working conditions. This is the reason that the pressure distribution plays a very important role in thermal resistance distribution and thermal deformation.

2.2 Nonuniformity of the Contact Pressure Distribution along the Machine Joint

Contact pressure in machine tool joints (the component of the contact stress vector normal to the nominal interface) is, generally, distributed nonuniformly along the interface. This causes the thermal contact resistance to be position-dependent. As indicated by Attia [9], the nonuniformity in the contact pressure distribution is due to the following factors:

1. The difference in the stiffness of contacting elements.

Because of this difference, the structure of a machine tool is treated as a beam on an elastic foundation as described by Kaminskaya et al [10]. The theory of bending of a beam on an elastic foundation assumes that the beam is resting on a continuously distributed set of springs, the stiffness of which is defined by a “modulus of foundation” k_f . The shape of the elastic line, i.e., profile of deflection $y(x)$, is influenced by the parameter $\lambda\ell$, where ℓ stands for the length of contact and λ is defined in terms of the modulus of foundation k_f , the modulus of elasticity E and the moment of inertia of the beam I , as defined by Den Hartog [11]:

$$\lambda = 4\sqrt{\frac{k_f}{4EI}} \quad (2.4)$$

According to Winkler’s hypothesis, the local contact pressure p_c depends on the deflection y in the given section, i.e.

$$p_c = k_f \cdot y \quad (2.5)$$

Thus, the contact pressure distribution $p_c(x)$ can be expressed as:

$$p_c = f(\lambda\ell) \quad (2.6)$$

2. The nature of mechanical loading.

Machine tool elements are usually subjected to a combined loading which is a result of forces, torsion and bending moments. Different loading gives different contact pressure distribution. As described by Heteyi [12], when the structure is under a concentrated loading F , the contact pressure distribution at the machine joint is

$$p_c(x) = \frac{F\lambda}{2} e^{-\lambda x} (\cos \lambda x + \sin \lambda x) \quad (2.7)$$

Under a uniformly distributed loading p , the contact pressure distribution is

$$p_c(x) = \frac{p}{2} (2 - e^{-\lambda x} (\cos \lambda x + \sin \lambda x) - e^{-\lambda(\ell-x)} (\cos(\ell-x) + \sin(\ell-x))) \quad (2.8)$$

When a bending moment M_0 is applied at the edge of the joint, the pressure distribution is

$$p_c(x) = 2M_0\lambda^2 (\cos \lambda x - \sin \lambda x) \quad (2.9)$$

Under multiple different loadings, the contact pressure distribution at the machine joint is the combination of the contact pressure distributions caused by each loading. This results in nonuniform contact pressure distribution of $p_c(x)$ over the interface.

3. Design and construction features.

Contact pressure distribution along a fixed joint is affected by its design and the number and distribution of clamping spots. In the case of a sliding joint which can be functioning as a fixed joint, there are some features which affect the stiffness of the joint and thus the contact pressure distribution:

- the clearance which causes the joint to be more compliant
- the gibs and backing strips which are generally of low stiffness

4. Surface irregularity.

The surface irregularities can be categorized by two parameters:

– Roughness (due to the characteristics of the machine tool, the geometry of the cutting tools, the speeds and feeds used during machining, etc.)

– Deviations in flatness (waviness) on to which the roughness is superimposed. This waviness is usually a function of the peculiarities of the process or the inaccuracies and deflections encountered in the machine tool.

Because of the surface irregularity, nonuniform contact pressure distribution is inevitable in a real joint.

5. Thermal loading.

The thermal field at the machine joint generates a nonuniform thermal stress distribution. Thus, contact pressure distribution at the machine joint is the sum of the mechanical contact pressure distribution and the thermal stress distribution. The thermal stress distribution is mainly affected by two factors:

– the deviation of the existing temperature field from the temperature field which is a linear function of the space coordinates

– the existence of external mechanical constraints which develop additional thermal contact stresses to make the beam deflection satisfy the given boundary conditions

For particular mechanical properties of contacting surfaces, the contact configuration is the result of the influence of the local contact pressure on the surface profile. As explained in Section 2.1, changes in the contact configuration accompanied by the change in the thickness of the interfacial gap, cause the change in the thermal contact resistance.

2.3 Review of Previous Work

The problem of thermal contact resistance at the interface of contacting solids is of fundamental importance; it has therefore received considerable attention, yielding

an extensive amount of literature. Generally speaking, these investigations were conducted in order to answer two questions: (i) for a given mechanical loading, what is the contact configuration? and (ii) for a given contact configuration and thermal loading, what is the thermal contact resistance?

In the studies of Thomas and Probert [13], Mikic and Carnasciali [14] and Yovanovich [15] the heat transfer through only one micro contact is considered. The total heat flow from one contacting body to another is divided into individual, separate heat flows corresponding to each micro contact and its corresponding gap (Fig. 2.3a). Each heat flow, Q , is then divided between the amount of heat which is transferred across the micro contact and the rest which is transferred through the interstitial medium. Thus the contacting bodies are treated as if they consist of a number of "unit cells" which are connected thermally in parallel. The surface between any two unit cells is taken as an adiabatic one. While the contact interface is usually treated as an isothermal surface, some investigators like Mikic and Mate [16] assumed a distribution for the heat flux over the contact spot in the form

$$Q/2\pi r_c \sqrt{r_c^2 - r^2}$$

r_c stands for the radius of the micro contact while r denotes the radial position of any point on the micro contact spot, $0 \leq r \leq r_c$. The micro contact spots are assumed to be identical and uniformly distributed over the contact area. Each micro contact is represented by a thin circular disc as shown in Fig. 2.3b. Because of the symmetry about the r -axis, only one-half of the unit cell is considered (Fig 2.3c). This model is known as the "disc-constriction" model. Other assumptions usually imposed on this model are:

1. Contact surface is perfectly clean, i.e., no surface films exist.
2. Heat conduction is the only mode of heat transfer.
3. Deformation of constriction disc under external loading is purely plastic.

Contact pressure over the micro contact area is equal to the plastic flow pressure, p_f , which is related directly to the hardness number, $p_f = H_B$.

As for the interstitial medium, some investigators such as Veziroglu, Yucu and Kakac [17] and Howard [18] have considered it, while the majority assumed that the contact is in vacuum. With the assumption of vacuum environment, the constriction resistance applies to both the mechanical and thermal contacts.

Based on the disc-constriction model, Cooper, Mikic and Yovanovich [19] extended their analysis to rough surfaces characterized by a Gaussian distribution of the asperity heights.

The correlation developed in the study by Cooper, Mikic and Yovanovich [19] does not require a knowledge of the change in the average micro contact radius as a function of the surface characteristics and the applied pressure. The expression derived for the thermal contact conductance h_c is

$$h_c = 1.45 \frac{k \tan \Theta}{\sigma_z} \left(\frac{p_a}{H_B} \right)^{0.98} \quad (2.10)$$

The limitations of this study which restrict its application to a certain extent, are:

1. The analysis is based on a single disc-constriction model, i.e., it does not account for the mutual interaction with neighbouring micro-contacts.
2. The change of pressure distribution due to the thermal deformation along the joint is ignored.
3. Surface asperities are assumed to be plastically deformed with no consideration of the elastic deformation of the surface sublayers.
4. With respect to the assumption that asperity heights are described by a Gaussian distribution, there is uncertainty about the actual distribution of the few peaks which are principally involved in the interaction between surfaces.
5. The plastic pressure is assumed to be equal to the hardness. The latter is given a constant value regardless of the loading level.
6. The surfaces in contact are perfectly clean, perfectly flat and placed in a vacuum.

The experimental technique, which has been applied in almost all available investigations by Cooper, Mikic and Yovanovich [19] and Fletcher and Gurog [20], is

performed by using two cylindrical specimens in contact. After applying a constant axial load F , heat is allowed to flow axially with a rate Q from one cylinder to another across the interface. Temperatures are then measured at discrete points located along the axis and far from the interface. By extrapolation, the temperature drop $(\Delta T)_I$ at the interface, and consequently the thermal contact resistance, can be determined.

The uncertainty about this experimental technique is that, in some cases, a negative value for the thermal contact resistance was obtained. The errors inherent to this technique can be attributed to the following reasons:

1. Extrapolation of temperatures on either side of the interface leads to serious errors as has been indicated by Thomas [21].
2. The relative stiffness of the contacting specimen has sometimes been chosen with no consideration of its effect on the contact pressure distribution along the joint. Under normal axial loading, a nonuniform contact pressure p_c is expected as described by Grocht [22]. Thus, by considering the contact pressure at the centre p_{cmax} to be equal to the applied pressure (i.e., the average contact pressure), serious errors are expected.
3. The thermal contact stresses developed at the interface are ignored and only the average mechanical contact pressure is considered. This causes the thermal contact resistance to be correlated to a contact pressure different from the real value.

Attia and Kops noticed these limitations in their works [23] and [24]. On prediction of thermal deformation of machine tools, they first recognized the nonlinear thermoelastic behaviour of a structural joint. From this point of view, the concept of closed-loop interaction was developed and a finite element method was used to calculate the thermal deformation by Attia and Kops [25]. A series of nonlinear thermal conductance values are applied to the contact elements of the finite element model. These values are calculated from the nonlinear pressure distribution by using Eq. 2.10.

In the experimental work carried out in [24], a centre force is applied to specimens

CHAPTER 2. THERMAL AND MECHANICAL BEHAVIOUR OF A MACHINE JOINT 14

of different shapes to obtain nonlinear contact pressure distributions. Long specimens are used to minimize errors in a plane strain analysis case. The temperatures are measured at the mid-plane using thermocouples. Deep drilling is required. To ensure contact at the tips of the thermocouples, the thermocouples are spring loaded.

Chapter 3

Experiment

3.1 Objective and Approach

The objective of the experiment is to determine the temperature fields under the effect of different mechanical loadings. These temperature fields are applied to the finite element model to obtain the thermal contact resistance and the combined contact pressure distributions along the interface. This objective brings about the need for a new experimental approach.

This work is a continuation of the research by Attia and Kops [24] with modification of their experimental methods.

In experiments carried out in the present study, the joint of a machine structure is represented by two rectangular specimens in contact. In order to avoid deep drilling and uncertainty of the thermocouple positioning, the block specimens used by Attia are now replaced by thin-plate specimens. Thus, the experiments represent a plane stress analysis case.

The contact pressure distribution along the machine joint is inherently nonuniform due to the nature of mechanical loading on the structure. In order to generate the nonlinear pressure distributions along the contact interface, axial loads are applied

to the upper specimens. The height-to-length ratio h/l of the upper specimen is the main factor creating a different profile of pressure distribution. In this study, two h/l ratios and three loads with each ratio are used.

In order to provide heat transfer across the contact interface, heaters are applied on the top of the upper specimen. Heat pumps attached on the lower part of the lower specimen act as heat sinks to ensure a balanced thermal field. The heat flows downward across the joint.

Because of the closed-loop interaction between the pressure distribution, thermal stress along the interface and the thermal contact resistance distribution, the temperature field caused by the heat transfer will constantly change until it reaches a steady state. Under the constant mechanical load and thermal input, the temperature field is affected directly by the thermal contact resistance along the contact interface.

Based on the temperature field obtained from the experiments, the finite element method is used to obtain the mechanical contact pressure combined with the thermal stress as the combined contact pressure distribution and through the iteration process, the final thermal contact resistance distribution is determined. The least squares method is then applied to the data for the whole range of contact pressure and thermal contact resistance and thus, the relationship between the thermal contact resistance and contact pressure based on their distributions is found.

The temperature field in the specimens is measured using thermocouples. Because the thickness of specimens is small and the walls are insulated, the temperature across the plate is considered to be uniform. The thermocouples are glued onto the side of the plates. As the interface area is the most interesting area in this experiment, more thermocouples are installed in this area to provide the most detailed information. Temperatures under the heater and above the heat pumps as well as along the edges of the specimens are also measured to obtain the boundary conditions.

3.2 Generation of Nonuniform Contact Pressure Distribution

The concept of generating different distributions of contact pressure $p_c(x)$ is based on the theory of unbonded contact of beam on elastic foundation. In this theory, the foundation is treated as isotropic half-space continuum and thus the interaction between the adjacent points is allowed to exist.

The problem of beams on elastic foundation both of continuum - or of Winkler-type has been intensively studied by Heteyi [12], Cheung and Zienkiewicz [26], Svec and Gladwell [27], and many others.

The distribution of the contact pressure is obtained from the profile of the deflection of the beam $y(x)$, along the contact interface which is defined as the x-axis, through the following differential relation:

$$p_c(x) = k_f \cdot y(x) \quad (3.1)$$

This deflection profile, known as the elastic line, is generally described in terms of k_f and the bending stiffness of the beam EI by the following differential equation:

$$EI \frac{d^4 y}{dx^4} = -k_f y + F_u, \quad (3.2)$$

where F_u stands for the distributed load acting on the beam. The solution of this equation takes the form

$$y(x) = e^{\lambda x}(C_1 \cos \lambda x + C_2 \sin \lambda x) + e^{-\lambda x}(C_3 \cos \lambda x + C_4 \sin \lambda x), \quad (3.3)$$

in which C_1 to C_4 are constants to be determined by virtue of boundary conditions, and λ is the characteristic of the system as expressed in Eq. 2.4.

Eqs. 3.2 and 3.3 suggest that the elastic line and consequently the distribution of the contact pressure $p_c(x)$ are significantly influenced by the distribution of applied load and the dimensionless parameter ' $\lambda \ell$ ', where ℓ denotes the contact length along

the joint. This parameter represents the relative stiffness of contacting bodies. Due to the uncertainty associated with the control and measurement of the distribution of applied pressure, our effort is confined in the present study to the case of a concentrated load. An increase in the height-to-length ratio of the beam, h/ℓ , results in an increase in the beam moment of inertia I and thus in a decrease in the parameter ' $\lambda\ell$ '. By decreasing the h/ℓ ratio, the beam becomes more flexible, causing a change in the distribution of the contact pressure $p_c(x)$.

As shown in Fig. 3.1, under a concentrated load, the profile of the pressure distribution changes from convex to concave as the h/ℓ ratio increases from 0.5 to 2.0. To cover a wider pressure range, more than one concentrated load is applied on the upper specimen. The values of different pressure distributions are obtained from the finite element analysis models developed in Chapter 4.

In previous experimental studies performed by Attia and Kops [24], loads of 2200 N to 17640 N (500 lbs to 4000 lbs) were applied to a set of blocks of a 127 mm (5 in) length with the same cross-section as the dimensions of the plates used in the current experiment. These loads were used to create the range of the contact pressure occurring along the interface.

As in this experiment, using plane stress conditions rather than plane strain, plates are used instead of blocks and their thickness is 6 mm , which is about 20 times thinner than the 127 mm (5 in) blocks used previously; hence, to recreate the same range of contact pressures, lesser loads are necessary:

$$\frac{2200 N}{20} = 110 N$$

$$\frac{17640 N}{20} = 882 N$$

To cover this range, loads of 98 N , 294 N and 882 N (10 kg , 30 kg and 90 kg) are chosen, thereby providing a 3-fold load increment factor. The contact region of the interface with a thickness of 6 mm and a width of 25.4 mm (1 in) results in an area of:

$$25.4 \text{ mm} \times 6 \text{ mm} = 152.4 \text{ mm}^2 = 1.524 \text{ cm}^2$$

Hence the loads of 98 *N* to 882 *N* (10 *kg* to 90 *kg*) cover a range of contact pressures from $p_{\min} = 294 \text{ kPa}$ (3 *kg/cm*²) to $p_{\max} = 7840 \text{ kPa}$ (80 *kg/cm*²). The typical value observed in machine tool structural joints is 3920 *kPa* (40 *kg/cm*²) [24]. Thus the average pressure values used in the experiments, notably 603 *kPa*, 1808 *kPa* and 5816 *kPa* (6.15 *kg/cm*², 18.45 *kg/cm*² and 55.35 *kg/cm*²), extend below and above the 3920*kPa* value.

In order to obtain information for different profiles of pressure distributions, upper specimens with two different h/ℓ ratios, 0.5 and 2.0, are used. For the ratio of 0.5, the height h of the specimen is 12.7 *mm* and the length ℓ is 25.4 *mm*. For ratio 2.0, h is 50.8 *mm* and ℓ is 25.4 *mm*. The upper specimen rests on the lower specimen, which is a square of 76.2 *mm* \times 76.2 *mm* and the same thickness of 6 *mm*.

The test specimens are made of AISI 1045 cold drawn steel with hardness of 160 H_B . The contact areas are ground. The measured value of the roughness of the surface is $R_a = 1 \mu\text{m}$.

3.3 The Distribution, Calibration and Installation of the Thermocouples

In response to the need to define the thermal contact resistance along the joint as a position-dependent function, a two-dimensional heat flow condition was ensured. The temperatures were measured by thermocouples. In order to obtain accurate temperatures, an advance knowledge of the characteristics of the disturbed temperature field was needed.

The difference between the measured temperature and that which would exist had no thermocouple been introduced is attributed to the following effects:

- the insertion of a single thermocouple

- the heat conduction along the thermocouple wire
- the disturbance resulting from the mutual interaction between two adjacent thermocouple holes

These effects were analyzed by Attia and Kops [28, 29]. In their study [28], the distance between the thermocouple hole and the heat input boundary was $2.4 \times D$, where D is the diameter of the thermocouple hole. In the present experiments, the diameter was 0.75 mm , so the minimum distance was 1.8 mm .

In the same study of Attia and Kops, it was pointed out that when the diameter of the thermocouple wire was 0.25 mm which was the case in this study, the error in thermocouple reading due to the heat conduction into thermocouple leads was of 0 to 0.10 of the quantity ' $g \cdot D$ ', where g is the temperature gradient of the undisturbed temperature field. The value of g in this study was $1 \text{ }^\circ\text{C}/\text{mm}$. So the error was $0.025 \text{ }^\circ\text{C}$ in the present experiments.

As explained in the work of Attia and Kops [29], to avoid the disturbance of one thermocouple affecting the temperature reading of another thermocouple downstream of it, the minimum distance was $4.75 \times D$, therefore, the minimum distance between the two thermocouples along the heat flow direction was 3.6 mm .

The disturbed area around the interface assumed to be a maximum of 2.5 mm on each side, was the most critical area concerned. Two rows in which each row has 9 thermocouples 2.5 mm above and below the interface were installed. Another two rows each having 9 thermocouples, were installed 4 mm above and 4 mm below each of the first two rows. This distance was slightly larger than the minimum distance. In order to obtain the temperature boundary conditions, a row of 9 thermocouples was installed 2.5 mm below the heating surface of upper specimen and another row of 9 thermocouples was installed 2.5 mm above the coolers attached to the lower specimen. For the rest of the boundary of the thermal field, thermocouples were distributed uniformly at a distance of 2.5 mm from the edges of the specimens. Figs. 3.2 and 3.3 demonstrate the thermocouple distributions for the two cases of h/ℓ

ratios: 0.5 and 2.0. With the h/ℓ ratio 0.5, the number of thermocouples on the upper specimen was 27. For the ratio 2.0, the number was 33. The lower specimen had 39 thermocouples on it. A total of 99 were installed on the specimens. Same thermocouple numbers were used in the thermocouple calibration.

Because the thermal contact resistance calculation depends on the temperature field, it imposed a stringent constraint on the allowed temperature measurement error. In order to meet this requirement, the selection of thermocouple and the methods of thermocouple calibration and installation were thoroughly studied.

The models of thermocouple wire used in the experiments were Omegalux GG-30 and TT-30 type-E. Both of the models were made of same alloy combination; the "+" lead was Chromega Nickel-Chromium and the "-" lead was Constantan Copper-Nickel. However, they had different insulation materials. The GG-30 thermocouple wire was insulated by glass braid and TT-30 was insulated by teflon. These thermocouple wires of 0.25 mm diameter gave a very stable thermal characteristic. The ends of two metal wires of the thermocouple were twisted tightly to ensure the best contact of the wires and they were carefully welded by the thermocouple welding machine. The welded junction was of an approximate 0.6 mm – 0.7 mm diameter.

A total of 99 thermocouples were calibrated. To give a series of standard temperatures, the Neslab Proportional Temperature Control RTE 200 heat bath which had a range of -30°C to 100°C was used. The reference temperatures were measured by an HP 2804A quartz thermometer with the accuracy of 0.01°C . To cover the working temperature range, four temperature points which were approximately 10°C , 40°C , 60°C and 90°C were chosen. Detailed calibration results are given in Tables 3.1, 3.2 and 3.3.

The calibrating procedure was as follows. First the Neslab RTE200 heat bath was turned on and the reference temperature was set. After about four hours when the desired reference temperature became steady, thermocouples were inserted into the bath and the temperatures were read through an Omegalux digital thermometer with

accuracy of 0.1°C . The same procedure was repeated 4 times at different reference temperature points. The adjustment of the thermocouples would be the average of the differences between the temperatures read from the Omegalux digital thermometer and the reference temperatures. As shown in Tables 3.1 to 3.3, the difference values were all within $\pm 0.1^{\circ}\text{C}$, which was the accuracy with which the temperature field was measured. This meant the measured temperatures could be treated as the temperatures of the thermal field.

The positions for installation of the thermocouples were marked with drills of 0.75 mm diameter and a depth of only 0.64 mm by using a precision mini-drilling machine. When the thermocouples were inserted into these shallow holes, caution was exercised to allow the junctions to contact the surfaces of the specimens.

The thermocouples were installed using the thermal conducting glue OMEGABOND 101. Thermocouples with glue were calibrated and the temperature readings were identical to the temperature measured by the same thermocouples without glue. This shows that OMEGABOND 101 presents a very good thermal conductivity. Its working temperature range was 0°C to 100°C , which covered the temperature range that the experiments required (20°C to 90°C).

3.4 Experimental Apparatus

The experimental apparatus consisted of two systems: a mechanical system and a thermal system (Figs. 3.4 and 3.5). The function of the mechanical system was to apply a concentrated line load to the upper specimen. The thermal system had the function of directing a stationary heat flow from the upper specimen through the interface to the lower specimen.

The mechanical system contained two sub-systems: a hydraulic system and a pneumatic system.

The hydraulic system included:

- an oil reservoir (A1)
- a hand-operated hydraulic pump (A2)
- a four-way valve (A3)
- a pressure gage with 4 *kPa* (0.5 *psi*) subdiv. (A4)
- a double-acting cylinder (A5)
- a rigid flat steel loading plate of 500 *N* (51 *kg*) weight (A6)

This system had two functions. One was to position the height of the knife edge for the different height ratios of the upper specimens. The other was to alter the load on the upper specimen by applying an upward pulling force to the loading plate through the double-acting cylinder. Changing the hydraulic pressure, the upward force applied by the cylinder on the loading plate was changed and thus the load on the upper specimen was adjusted. In order to find out the corresponding pressure reading of the hydraulic manometer from the desired load, a calibration of the manometer was done. The load of the loading plate as measured by the scale was 500 *N* (51 *kg*), and this corresponded to a zero pressure reading on the manometer. As the pressure in the hydraulic system was increased, the load on the scale was decreased. For loads 98 *N* (10 *kg*) and 294 *N* (30 *kg*), the corresponding readings of the pressure gage were 48 *psi* and 67 *psi*, respectively. A load of 882 *N* (90 *kg*) was achieved by adding weight of 382 *N* (39 *kg*) to the 500 *N* (51 *kg*) loading plate. At this point, the hydraulic system was not applied.

The pneumatic system consisted of a self-aligning aerostatic bearing table (A7) on which the lower specimen rested. The bearing top plate had a convex bottom and sat on a concave-shaped base. Compressed air was forced through the air nozzles, creating an air cushion between the top and the base, thus allowing the table and the test specimens on it to self-align themselves to the knife edge.

The thermal system consisted of:

- two 10-watt Omegalux printed circuit heaters (B1)
- six Peltier heat pumps Model CP-1.4-71-0.6L (B2)

- two independent DC power supplies for heaters and heat pumps (B3)
- two springs pressing the heaters (B4)
- Omegalux GG-E-30 and TT-E-30 thermocouples (B5)
- one Omegalux digital thermometer (B6)
- two fins for cooling heat pumps (B7)

The area of the commercially available heater was greater than the area of the upper specimen to be heated. The dimensions of the heaters were $25.4 \text{ mm} \times 12.7 \text{ mm}$; the surfaces to be heated were $12.7 \text{ mm} \times 6 \text{ mm}$. To prevent the heaters from developing hot spots, they were placed between two layers of brass sheeting. Two springs were inserted between the heaters and the knife shoulder to press the heater to the specimen for good thermal contact.

The specimens were insulated from the ambient air using fibreglass wool. First, small fibreglass particles were inserted into spaces between the thermocouples, then the plates were wrapped in layers of fibreglass wool. For the purpose of streamlining the heat flow, out of the six heat pumps installed, only the two central heat pumps on each side of the lower specimen were powered. Two fins were installed on either side of the assembly in order to enhance convection cooling of the hot side of the heat pumps. Thermal conductive paste was spread on the contacting surface of the heat pumps, the heater, and the brass plates to ensure uniform thermal conductivity.

3.5 Experimental Procedure

Before the test was started, all of the contact area of the specimens was thoroughly cleaned in order to obtain the best thermal conductivity.

The upper specimen which had h/ℓ ratio 0.5 was placed on top of the bottom specimen. The compressed air valve was turned on and air was released into the air bearing. The hydraulic pump was used to lower the knife edge down to the top of the upper specimen; when the distance was about 2 mm , the downward movement of the

knife was stopped. After a very careful adjustment of the position of the specimens which assured that the knife edge and the two centre lines of the upper specimen and the lower specimen were colinear, the hydraulic pump was used again now allowing the knife to be lowered down onto the top of the upper specimen. The 382 *N* (39 *kg*) weight item was added to the loading plate so as to obtain the desired 882 *N* (90 *kg*) load. The mechanical load was thus achieved.

To obtain the thermal field, the power supplies of the heaters and the heat pumps were then turned on. The temperature of the middle point above the interface was monitored and the power supplies of the heaters and the heat pumps were adjusted accordingly. The steady state thermal field was achieved after four hours. To increase cooling, two fans were set blowing towards the fins under the angle of 45°.

The temperature of every thermocouple was read on the digital thermometer.

After the three-round temperature measurement, the 382 *N* (39 *kg*) weight was removed. The next mechanical load applied to the upper specimen was 294 *N* (30 *kg*) and was achieved after pumping the hydraulic pressure to the point which corresponded to the 294 *N* (30 *kg*) load. At the same time, the temperature field was monitored constantly. The power supply of the heat pumps was adjusted to make sure the temperature remained steady. The three-round temperature measurement was carried out and then repeated for the 98 *N* (10 *kg*) load.

After finishing tests with one upper specimen ($h/\ell = 0.5$), the hydraulic cylinder was pumped up to give enough space between the knife edge and the upper specimen to change it (to the one with h/ℓ ratio 2.0), and the same experimental procedure was applied again.

Chapter 4

Finite Element Analysis

4.1 Objective and Approach

The objective of this chapter is to determine the final contact pressure distribution and the thermal contact resistance along the interface.

From the theory of the nonlinear behaviour of the machine joint, it is known that a closed-loop interaction between the pressure distribution, thermal stress distribution and the thermal contact resistance exists. The pressure distribution along the contact surface controls the thermal contact resistance distribution. Different local values of the thermal contact resistance cause different heat transfer across the interface imposing the thermal field which changes the profile of the contact surfaces through the thermal stresses it develops along the joint. As the thermal field reaches a steady state, the values of the three elements in the closed-loop interaction converge to the equilibrium values which are unknown in advance. Thus, the final contact pressure distribution is defined as the result of the mechanical contact pressure distribution and thermal stress distribution.

To find out the effect of the contact pressure distribution on the thermal contact resistance, the values of the final contact pressure and the thermal contact resistance

are required.

Geometric models of the specimens used in the experiments are designed. They are built in a finite element analysis system named ALGOR. In ALGOR stress analysis module, material properties, stress boundary conditions and concentrated forces are applied to the models. After the models have been processed, the mechanical contact pressure distribution along the interface is obtained.

In order to obtain the thermal contact resistance distributions, material properties and thermal boundary conditions are applied to the the model. First, the assumed values of thermal conductivity distribution are applied to the elements along the interface in the model, since ALGOR requires thermal conductivity instead of thermal resistance. By running this model in the ALGOR heat transfer module, a temperature field is obtained. Comparing this field with the experimental temperature field, the distribution of thermal conductivity of the elements along the interface is adjusted and the model is run again with the new values. After several iterations, a temperature field, which is close enough to the experimental temperature field, is determined. This temperature field is used to obtain the combined final contact pressure distribution. At the same time, the final thermal conductivity of the elements along the interface is obtained. The thermal conductivity is then converted to the thermal contact resistance along the interface.

Applying the final temperature field to the stress model node-by-node, the final contact pressure distribution along the interface is determined. The whole computing procedure is demonstrated in Fig. 4.1.

4.2 Introduction to ALGOR

This section is based on the ALGOR software user's guide [30].

ALGOR is a comprehensive mechanical FEA software system. It consists of five integrated families described here.

1. SUPERDRAW II is a geometric modelling program like Autocad where the model is constructed and where the boundary conditions are specified.

To create a large complicated model in a FEA software is very time consuming and requires a substantial amount of processing time. In ALGOR, the way to reduce this time is to divide the model into several simple parts, create each of them separately and save them under different names, and then merge them together.

For engineering models, one has access to different colours, different groups and different layers. They are summarized as follows:

- Colours are used to assign certain element aspects (e.g. element thickness, applied pressure) to specific elements
- Groups are used to assign different material properties to specific elements
- Layers are used to combine sections of a model together

2. DECODER is a program that reads a file in one format and creates output files in other formats. ALGOR provides many different decoders, each tailored to translate certain types of models for different purposes. In this work the stress decoder and the thermal decoder were used. The decoders translate files created in Superdraw II into files suitable for display and analysis in Superview. The decoders also create the files required for analysis by ALGOR's Finite Element Analysis processors. The drawing mistakes which are made in Superdraw II are checked out here.

The material properties are entered through decoders. One can define the element type, material and element properties used in the particular model. There are five types of elements available with isotropic material properties: Truss membrane, 2-D elasticity, Brick, Plate, and Shell.

3. COMBSST and COMBSTT create a single model file composed of multiple, decoded model files. One can use this to create one file with multiple element types, or to create a model that has many identical components in multiple locations.

4. STRESS AND THERMAL PROCESSORS are finite element analysis processors which solve for the stress and thermal fields from the processed geometry and

boundary conditions provided by the decoders.

5. SUPERVIEW is a read-only program which enables one to visualize the model. It enables one to examine the model as if it were an actual physical object. Also, it will give one the output data from the FEA processor, such as the stress and temperature at every node and the heat flux going through an individual element in a certain direction, etc.

Here is a general procedure for creating and processing a finite element analysis model with ALGOR (Fig. 4.2):

1. Create the model in Superdraw II. When one finishes the model, the "Transfer" command is used to send the model to the decoder, which processes the model so that it can be displayed in Superview.

2. Use the Decoder to prepare the model for viewing. When the decoder finishes, one can display the model in Superview. If the Decoder reports errors in the model, it can be examined in Superview to determine where the errors occurred. The Decoder generates the files used by Superview from the files produced by Superdraw II. The original Superdraw II file is not changed during decoding - the file is translated to a new format (and saved with a new file extension), and additional information is included in the Superview files.

3. Send the decoded file to the Finite Element Analysis Processor to solve for the required field.

4. Return to Superview to obtain the final data.

4.3 Creating the Finite Element Model

In this study, the experiments dealt with nonlinear thermoelastic behaviour at the interface of two contact surfaces subjected to a nonuniform pressure distribution and heat flow across the interface. Because the disturbed zone, which extended 2.5 *mm* above and below the interface, had different thermal conductivity than the material of

the specimens, it was treated differently in the finite element analysis program. The upper specimen, the lower specimen and the contact interface which included the contact zone were modelled separately. Thermal conductivity values of the elements along the interface varied to represent the nonuniform distribution. Both the stress field and thermal field were symmetrical with respect to the centre line. To model this, the interface was divided into five sections, each section containing two elements which were symmetrically located on each side of the centre line. These two elements had the same thermal conductivity. All these sections were saved in different layers. The upper specimen and lower specimen had the same material properties; therefore, they were saved in one layer. A total of six layers was used to save the six parts of the model. These layers were saved and decoded in separate files. To group the six layers together, the two programs COMBSST and COMBSTT were used. The combination of all the layers constituted the entire model. The models of the specimens of different h/l ratios are presented in Figs. 4.3 and 4.4.

The model was drawn in the YZ plane as it is required by ALGOR that all plane stress and plane strain models (i.e. 2-D models) must be constructed in the YZ plane (otherwise, an error would occur when decoding the model).

The following are characteristic features of the finite element model in ALGOR:

- Model was two-dimensional
- Rectangular elements were used to construct the model
- Six layers were formed: layer 1 was for the upper and lower specimens and layers 2 to 6 were used to model the elements at the interface
- For the stress analysis model, a point force was applied at the mid-point of the top line of the upper specimen to simulate the knife edge loading conditions
- Boundary conditions for the stress analysis model required that the nodes on the bottom line of the lower specimen be restricted from movement corresponding to the situation of the test specimen resting on a rigid base
- For the thermal analysis model, the temperature boundary which was obtained

from the experiment was applied to the model. There was no heat exchange between the boundary of the model and the environment, reflecting the insulation of the specimens in the experiment

· An initial room temperature of 25°C was assigned to all remaining nodes

The following material properties were assigned to the model:

Material: AISI 1045 CD

Poisson Ratio: $\nu = 0.292$

Thermal Expansion Coefficient: $\alpha_e = 1.08 \times 10^{-5} \text{ }^{\circ}\text{C}^{-1}$

Diffusivity: $\alpha_d = 1.474 \times 10^{-5} \text{ m}^2/\text{s}$

Density: $\rho = 7.833 \times 10^3 \text{ kg/m}^3$

Thermal Conductivity: $k = 54 \text{ W/m }^{\circ}\text{C}$

Young's Modulus of Elasticity: $E = 2.01 \times 10^8 \text{ kPa}$

Each different layer was then decoded in the stress and thermal decoder separately. The decoders were accessible from the Superdraw II program from the ALGOR menu of the stress analysis or heat transfer modules. The decoder in the stress analysis module was used to decode the stress problem while the one in the heat transfer module was used for the thermal problem. The stress analysis module of ALGOR allows application of the temperature field which is obtained from the heat transfer module to the model in the stress module; the temperature field must be known prior to solving for the stresses. Due to unknown thermal contact resistance, the node temperatures were unknown and were to be determined. This had to be done through iteration which will be described in the next section.

4.4 FEA Determination of the Thermal Conductivity and Pressure Distributions

An iterative computing method was used to determine the thermal conductivity distribution along the interface and the temperature field which was used in the stress analysis module for the combined pressure distribution.

It was assumed that the thermal conductivity was proportional to the local contact pressure distribution, and therefore it could be calculated from the pressure distribution obtained from the stress analysis module in ALGOR. The originally assumed values of the thermal conductivity distribution were based on the original mechanical contact pressure distribution. From the thermal conductivity values assigned to the elements along the interface, the thermal analysis module generated a temperature field. This field was compared with the temperature field obtained from the experiment and new thermal conductivity values were determined and assigned to the elements along the contact interface of the model. After several iterations, the thermal conductivity distribution converged to the final distribution. The last temperature field was then applied to the stress model to obtain the corresponding contact pressure distribution along the interface.

To follow this procedure, the stress analysis model was first used to find the mechanical pressure distribution; the ambient temperature of 25°C was assigned to every node. The desired type of simulation was specified (i.e. 2-D plane stress) in the "Type" option of the "Element" submenu of the stress decoder. In the same submenu, the material used in the "Group" option was specified. Since no group numbers were provided for the simulation, only group I could contain the specific material properties for each layer. For all layers, the same material properties were entered. In the "Analysis" submenu, "static" was specified for static analysis. In the "Load Case" option of the "Globe" submenu, a "Load Case Multiplier" of 3 was specified for 98 N , 294 N and 882 N (10 kg , 30 kg and 90 kg) for A(Press).

B(Accel), C(Disp) and D(Therm). Details about this option are available in the ALGOR manual section on the decoder. Then, the "Decode" submenu was entered to perform the decoding of the file once the three options - (1) intersect lines, (2) invalid lines, (3) invalid regions - are released from performing (a star must appear in front of each of these options in order to release them). To accelerate the process, these settings were saved as default settings for the other layers to be decoded.

Once the decoded files of the six layers of the model were obtained, the "Combine" option of the COMBSST menu was performed. As explained earlier, this option required each piece of the model to be assembled into the entire model. Then, the model was ready to be processed by the "Static Analysis Processor" (SSAP0H). This processor created an output file where the results were read by a word processor like WordPerfect and were seen graphically by the "Superviews" program available through the ALGOR menu. The outputs were the mechanical contact pressure distributions along the interface. These mechanical contact pressure values were used to calculate the assumed thermal conductivity values k which were later entered into the thermal decoder.

When the thermal decoder was used to decode the interface blocks, thermal conductivity values k of the elements along the interface were required. Since the exact values of k were unknown, they were initially assumed as follows.

Considering the thermal field was symmetrical with respect to the centre line, the heat flux along this line was not distorted and run perpendicularly across the interface. Thus, the thermal conductivity of the centre element could be calculated as a one-dimensional problem (Fig. 4.5).

$$\Delta T' = \frac{(T_1 - T_2) + (T_3 - T_4)}{2}, \quad (4.1)$$

where T_1 to T_4 are measured temperatures along the centre; $\Delta T'$ stands for the average value of the temperature drop between the two measured temperatures along the centre line on each side above and below the disturbed zone. The heat flux along

the centre line was then determined as

$$q_{centre} = \frac{\Delta T'}{c} \times k, \quad (4.2)$$

where c stands for the distance between T_1 and T_2 , and k is here the thermal conductivity of the AISI 1045 CD. Because the thermal field was one-dimensional along the centre line, the same heat flux run through the centre element of the interface. The assumed thermal conductivity of the centre element of the interface was obtained:

$$k_{centre} = \frac{q_{centre} \times d}{T_2 - T_3}, \quad (4.3)$$

where d is the depth of the disturbed zone across the interface.

The thermal conductivity was assumed to be proportional to the local mechanical contact pressure with the coefficient of proportionality C which can be calculated from

$$C = \frac{k_{centre}}{p_{mech\ centre}} \quad (4.4)$$

The first assumed thermal conductivity distribution along the interface was then calculated for the local values of mechanical contact pressure distribution along the interface:

$$k(x) = C \times p_{mech}(x) \quad (4.5)$$

The first assumed values of thermal conductivity were assigned to the elements along the interface through the thermal decoder. Then the model was processed by the thermal processor (SSAP10H). The temperature field obtained from FEA was compared with the experimentally determined temperature field. It was found that the biggest temperature difference occurred within two rows of nodes above and below the interface zone. Thus the temperatures of these two rows from the experiment became the reference temperatures for the comparison.

The heat passing through each element along the interface in both experimental temperature field and numerically calculated temperature field should be the same. Therefore:

$$q = \frac{T_{2exp} - T_{3exp}}{d} \times k_2 = \frac{T_{2cal} - T_{3cal}}{d} \times k_1, \quad (4.6)$$

where T_{2exp} and T_{3exp} are the local temperatures of the upper row and lower row from experiment and T_{2cal} and T_{3cal} were the corresponding calculated temperatures, k_1 is the thermal conductivity used in the FEA model and k_2 is the thermal conductivity used in the next iteration:

$$k_2 = \frac{T_{2cal} - T_{3cal}}{T_{2exp} - T_{3exp}} k_1 \quad (4.7)$$

Subsequently, a new series of k was obtained. This iteration continued until the two temperature fields became identical within an acceptable error.

There was a number of possible sources of error. One of the two main sources was the thermocouple positioning error: the spot where the thermocouple was installed was not exactly where it was planned to be, and thus not exactly in the same position as the corresponding node in the finite element model. The maximum distance error was ± 0.1 mm. Since the experimental temperature field indicated the maximum temperature gradient of $1^\circ\text{C}/\text{mm}$, the positioning contributed $\pm 0.1^\circ\text{C}$ to the error. The other source of the error was the accuracy of the temperature digital thermometer which was $\pm 0.1^\circ\text{C}$. Adding these two factors together, the total temperature error was $\pm 0.2^\circ\text{C}$. Temperatures within this range were treated as identical.

The iteration gave the final results of the thermal conductivity distributions, which will be converted to thermal contact resistance distributions, along the interface under different mechanical loads, in Chapter 5.

However, the thermal fields induced thermal stresses contributing to the final contact pressure distribution at the interface. Thus, to find the final contact pressure distributions, temperature fields were used. In order to transfer the temperature fields to the stress model, a program in the thermal analysis sub-system called "Advance" was used. Combined with the temperature field, the stress model was run with the

same procedure used for the mechanical contact pressure distribution. The program gave the final combined contact pressure distribution along the interface.

Chapter 5

Results and Discussion

As described in Chapter 3, two upper-specimens, $h/\ell = 0.5$ and $h/\ell = 2.0$, are used in the experiments. These two different ratios divide the experiment data into two groups of distinctively different contact pressure distribution: one with maximum at the centre and the other with the minimum at the centre, i.e. convex and concave respectively. In each group, three different axial loads: 98 *N*, 294 *N* and 882 *N* (10 *kg*, 30 *kg* and 90 *kg*), are applied on the upper-specimen, introducing three levels of these two types of pressure distribution. Thus, six cases in which temperature fields are measured are investigated. The two-dimensional temperature fields are shown in Figs. 5.1 and 5.2, while experimental temperature data is given in Tables 5.1 to 5.12. Examining the temperature data, it is found that the temperature just below the heated surface was nearly identical in each of the six cases: the maximum difference is 0.2°C (Tables 5.13 and 5.14). This means that regardless of the mechanical load, the heat input is kept constant. However, due to the different thermal contact resistance along the interface, temperatures above the heat pumps are different.

The contact zone which contains the area 2.5 *mm* wide above and below the interface is considered the most important area. To assess the temperature data of this area, the contact surface is divided into nine channels: each channel contains one

thermocouple of each row. As shown in Fig. 4.5, every channel is treated as isolated from each other, which means that the heat flow in the channel is not affected by the heat flow in the neighbouring channels. Thus, there is an one-dimensional thermal field in each channel.

The two rows of thermocouples from each side above and below the interface are used to calculate the temperature drop ΔT caused by the interface.

$$\frac{T_1 - T_2}{c} = \frac{T_2 - T_a}{d/2} \quad (5.1)$$

$$T_a = T_2 - \frac{d/2}{c}(T_1 - T_2) \quad (5.2)$$

$$\frac{T_3 - T_4}{c} = \frac{T_b - T_3}{d/2} \quad (5.3)$$

$$T_b = T_3 + \frac{d/2}{c}(T_3 - T_4) \quad (5.4)$$

$$\Delta T = T_a - T_b, \quad (5.5)$$

where d is the depth of disturbed zone which here is 5 mm, and c is the distance between thermocouples which is 4 mm.

The results are given in Tables 5.15 and 5.16. It can be seen that, for different h/ℓ ratios 0.5 and 2.0, under 882 N load, the maximum values of ΔT along the interface are 0.6°C and 0.4°C respectively. When the load is decreased to 98 N, the maximum values of ΔT increase to 3.6°C and 2.0°C respectively. These results are considered reasonable [31], and therefore, further finite element analysis based on these temperature fields can be carried on.

The concept of the closed-loop interaction at a machine joint states that the thermal field in structural elements causes their thermal deformation, which generates thermal stresses along the joint, altering the existing mechanical pressure distribution.

New contact pressure distribution gives a new thermal contact resistance distribution which leads to a new thermal field. This new thermal field results in a new thermal stress distribution along the interface. The iteration will continue until a state of equilibrium is reached. Thus, the final contact pressure distribution $p_c(x)$ at the equilibrium state is the result of the mechanical contact pressure distribution $p_{mech}(x)$ and the thermal stress distribution along the interface $s_{th}(x)$ at the equilibrium state.

$$p_c(x) = p_{mech}(x) + s_{th}(x) \quad (5.6)$$

A finite element method described in Chapter 4 was used to find the mechanical pressure distribution, the final contact pressure distribution and the thermal contact resistance distribution along the interface between the specimens.

Because the stress field and thermal field were both symmetrical with respect to the centre line, only half of the model was examined and half of the data used. The first results obtained from this method were the original mechanical pressure distributions of the six cases. Because there was no heat transfer and the temperature fields were uniform, neither thermal stress nor thermal deformation occurred along the interface. In the finite element model, half of the interface was divided into five elements and each element was connected with its two neighbouring elements by two nodes. There were six nodes along the interface of the model (Fig. 5.3). The pressure distributions obtained from the finite element method were the normal stress at the nodes (Tables 5.17 and 5.18). Since the thermal conductivity was the property of the element recognized by ALGOR, the contact pressure values on the corresponding elements were required. The contact pressure at the interface of each element is calculated by taking the average of the pressures of its two neighbouring nodes. For example:

$$p_{element1} = \frac{p_{node1} + p_{node2}}{2}$$

Tables 5.19 and 5.20 present the values of mechanical contact pressure for each element along the interface for the six cases. Figs. 5.4 and 5.5 show the mechanical contact

pressure distributions along the interface. The x-axis in the Figures represents the relative position from the centre line to the edge of the contact interface.

Under the axial loads of 98 N, 294 N and 882 N (10 kg, 30 kg and 90 kg), the corresponding averages of pressure values are 603 kPa, 1808 kPa and 5816 kPa (6.15 kg/cm², 18.45 kg/cm² and 55.35 kg/cm²). The average pressures in Tables 5.19 and 5.20 are slightly different from the above values. The maximum difference of five percent occurs at $h/l = 0.5$ and $F = 98$ N and is considered acceptable. These differences are caused by the finite element identification (Fig. 5.3). Only five elements below the interface should carry the pressure from the upper specimen. The pressure on the rest of the lower specimen elements on the interface level outside the upper specimen is supposed to be zero. However the finite element calculation provides values of the normal stress on these "outside" elements which are not equal to zero. If these values are added to the values of the elements along the interface, the sums are equal to the average values as originally expected. The finite element model is also limited by the fact that, the nodes along the interface are common to both the upper and lower elements and no sliding between them is permitted. The maximum effect caused by the no-sliding restriction takes place at the two ends of the interface in the model and, therefore, the values obtained at the ends of the interface are considered to have the maximum deviation from the real situation.

With temperature fields applied to the finite element models, the combined mechanical and thermal stress fields of the specimens were determined. Figs. 5.6 and 5.7 show the close view of the stress field of the interface area. The normal combined stress distributions at nodes along the interface were obtained (Tables 5.21 and 5.22). Using the same method described above, the combined contact pressure distribution of the elements were calculated (Tables 5.23 and 5.24, Figs. 5.8 and 5.9).

Comparing the average values of final combined contact pressure distributions and mechanical contact pressure distributions along the interface in each case, it can be seen that they are very close to each other. This is illustrated in Figs. 5.10 and 5.11.

This indicates that the thermal stress along the interface does not add any significant value to the value of the mechanical pressure distribution. It just redistributes the pressure at the interface.

Using Eq. 5.6, data of the pressure change along the interface caused by the thermal stress in the different cases are obtained (Tables 5.25 and 5.26). Figs. 5.12 and 5.13 demonstrate their distribution along the joint. Examining the data, one can find that the arithmetic mean of $s_{th}(x)$ of each case is very small compared to the average magnitude of mechanical pressure, which confirms the earlier conclusion.

The effect of the thermal stress distribution on the mechanical pressure distribution $\Phi(x)$ can be defined as

$$\Phi(x) = \frac{|s_{th}(x)|}{p_{mech}(x)} \quad (5.7)$$

Tables 5.27 and 5.28 contain Φ values expressed as percentage which demonstrate that the thermal stress has more effect on the pressure distribution of lower values as, percentagewise, Φ decreases when the load increases.

It should be mentioned here, that the effect of thermal stresses does not only depend on the value of pressure but also depends on other factors, such as the coefficient of thermal expansion of the material; however, in this thesis the effect of other properties is not considered.

The thermal analysis module in ALGOR was used to find out the thermal conductivity distribution along the interface. As described in Sect. 4.4, since the thermal conductivity distribution along the joint was unknown in advance, initially the assumed thermal conductivity values proportional to mechanical contact pressure were assigned to the elements along the interface of the model. These assumed values are given in Tables 5.29 and 5.30. Running this model in the thermal analysis module provided the temperature field. This temperature field was compared with the experimental temperature field and the thermal conductivity values were adjusted. The model was run again with the new values. After several iterations, the final thermal conductivity distribution of the elements along the interface was obtained

(Tables 5.31 and 5.32). Figs. 5.14 and 5.15 present the first assumed and the final thermal conductivity distributions. One can find substantial difference of the thermal conductivity values between the first assumption and the final results obtained through iterations. This indicates that the assumed proportionality of the thermal conductivity to the local mechanical contact pressure does not represent the actual situation.

Based on the thermal conductivity distribution, the thermal resistance distribution of the disturbed zone is calculated from the known relationships:

$$R(x) = \frac{1}{h(x)} \quad (5.8)$$

$$h(x) = \frac{k(x)}{d} \quad (5.9)$$

Thus,

$$R(x) = \frac{d}{k(x)}, \quad (5.10)$$

where $R(x)$ is the thermal resistance distribution of the disturbed zone of depth d , $h(x)$ is the thermal conductance distribution, and $k(x)$ is the thermal conductivity distribution.

The thermal resistance of the disturbed zone $R(x)$ is a combination of the thermal resistance of the material of the disturbed zone and the thermal contact resistance caused by the interface $R_c(x)$. The value of the thermal resistance of the material of the disturbed zone is $0.0926 \text{ m}^2\text{C}/\text{kW}$. Thus,

$$R_c(x) = R(x) - 0.0926 \quad (5.11)$$

Tables 5.31 and 5.32 give the values of thermal contact resistance of the elements along the interface, and Figs. 5.16 and 5.17 demonstrate their distributions along the interface. Figs. 5.18 to 5.23 show the relationship between thermal contact resistance distributions, $R_c(x)$, and contact pressure distributions, $p_c(x)$, plotted against the interface, x/L . As expected, when the contact pressure increases, the thermal

contact resistance decreases, and it is evident that their distributions are inversely proportional to each other. One can now use these distributions to determine the relationship between thermal contact resistance, R_c , and contact pressure, p_c , from their local values.

To find this relationship, the least squares method is used. Figs. 5.24 to 5.25 show the resulting thermal contact resistance plotted against the contact pressure under all loading conditions, for $h/\ell = 0.5$ and $h/\ell = 2.0$, respectively. The curve for the case $h/\ell = 2.0$ and $F = 98 \text{ N}$ can be approximated by

$$y = a + bx$$

The remaining five cases can be represented by

$$y = a + \frac{b}{x}$$

Based on the relationship between thermal contact resistance and contact pressure in these five cases (the first case will be treated separately), it is estimated that

$$R_{cest} = a + \frac{b}{p_c} \quad (5.12)$$

The least squares method defines the curve for which the sum of magnitudes of Δ_i under the curve will be equal to the sum of magnitudes of Δ_i above the curve, i.e. the average of Δ_i is equal to zero. Δ_i is defined by the difference between the thermal contact resistance data and the value of the fitting curve. In order to find the values of a and b which will give the best fitting curve, the function has to be minimized:

$$S = \sum_{i=1}^n (\Delta_i)^2 = \sum_{i=1}^n (R_{cdata} - R_{cest})^2 = \sum_{i=1}^n (R_{cdata} - a - \frac{b}{p_c})^2 \quad (5.13)$$

by taking partial derivatives of S with respect to a and b and setting them equal to zero:

$$\frac{\partial S}{\partial a} = 2 \sum_{i=1}^n (a + \frac{b}{p_c} - R_{cdata}) = 0 \quad (5.14)$$

$$\frac{\partial S}{\partial b} = 2 \sum_{i=1}^n \left(a + \frac{b}{p_c} - R_{cdata} \right) \frac{1}{p_c} = 0 \quad (5.15)$$

For brevity, the sums are expressed as

$$\overline{1/P} = \sum_{i=1}^n \frac{1}{p_c} \quad (5.16)$$

$$\overline{R} = \sum_{i=1}^n R_{cdata} \quad (5.17)$$

$$\overline{(1/P)^2} = \sum_{i=1}^n \left(\frac{1}{p_c} \right)^2 \quad (5.18)$$

$$\overline{R/P} = \sum_{i=1}^n \frac{R_{cdata}}{p_c} \quad (5.19)$$

With this notation, the Eqs. 5.14 and 5.15 are expressed as

$$a + b \overline{1/P} = \overline{R} \quad (5.20)$$

$$a \overline{1/P} + b \overline{(1/P)^2} = \overline{R/P} \quad (5.21)$$

so that a and b can be solved simultaneously

$$a = \frac{\overline{1/P} \overline{R/P} - \overline{R} \overline{(1/P)^2}}{\overline{(1/P)^2} - (\overline{1/P})^2} \quad (5.22)$$

$$b = \frac{\overline{R} \overline{1/P} - \overline{R/P}}{\overline{(1/P)^2} - (\overline{1/P})^2} \quad (5.23)$$

For the case $h/\ell = 2.0$ and $F = 98 \text{ N}$, we estimate

$$R_{ccest} = a + b \cdot p_c \quad (5.24)$$

Using the same method, a and b of this function are obtained.

The relationship function of every case is shown below:

$$\text{for } h/\ell = 0.5 \text{ and } F = 98 \text{ N} \quad R_c = 0.0145 + \frac{29.8}{p_c} \quad (5.25)$$

$$\text{for } h/\ell = 0.5 \text{ and } F = 294 \text{ N} \quad R_c = -0.0175 + \frac{64.0}{p_c} \quad (5.26)$$

$$\text{for } h/\ell = 0.5 \text{ and } F = 882 \text{ N} \quad R_c = -0.0078 + \frac{59.5}{p_c} \quad (5.27)$$

$$\text{for } h/\ell = 2.0 \text{ and } F = 98 \text{ N} \quad R_c = 0.1331 - 0.0001p_c \quad (5.28)$$

$$\text{for } h/\ell = 2.0 \text{ and } F = 294 \text{ N} \quad R_c = -0.0096 + \frac{52.0}{p_c} \quad (5.29)$$

$$\text{for } h/\ell = 2.0 \text{ and } F = 882 \text{ N} \quad R_c = -0.0142 + \frac{53.1}{p_c} \quad (5.30)$$

These functions are combined for three levels of loading and plotted separately for $h/\ell = 0.5$ and $h/\ell = 2.0$, each case covering its own range on a R_c vs. p_c graph, Figs. 5.24 and 5.25. One can see that they follow a common trend, which could be represented by

$$R_{ccst} = \frac{b}{p_c} \quad (5.31)$$

Using the least squares method, two new functions of the relation between the thermal contact resistance and the contact pressure are obtained for two groups of the latter, convex and concave:

$$\text{for } h/\ell = 0.5 \quad R_c = \frac{32.9}{p_c} \quad (5.32)$$

$$\text{for } h/\ell = 2.0 \quad R_c = \frac{39.2}{p_c} \quad (5.33)$$

Figs. 5.24 and 5.25 show that these two functions fit the data very well.

Comparing these two curves with separate curves at each pressure range case (Figs. 5.24 and 5.25), it can be seen that while at the lower pressure range the agreement is very good, it deteriorates at high pressure range. This might be influenced by the fact that, the relationship R_c vs. p_c at high pressure range was obtained for a steeper slope of the contact pressure distribution along the interface.

Comparing the results of the convex and concave contact pressure distributions (three of each), one finds that they are very close to each other. Therefore, using the least squares method, a general function combining the results of all distributions is obtained:

$$R_c = \frac{37.9}{p_c} \quad (5.34)$$

Fig. 5.26 presents the general function and Fig. 5.27 demonstrates the same function in log-log coordinates. It can be seen that the data for both contact pressure distributions (convex and concave) are quite close to each other. Again, the deviations could probably be attributed to variation in slopes and perhaps also differences in convex/concave shapes. The seemingly large departure from the straight line of the general function in the high contact pressure range is exaggerated due to the log-log coordinates, and it is in fact quite small.

In the theoretical research work of Mikic [32], the relationship between the thermal contact resistance and contact pressure expressed as a function combining the micro-constriction resistance and macro-constriction resistance, R_1 and R_2 respectively, is

$$R_c = R_1 + R_2 = 0.689 \frac{\sigma_c}{k \tan \Theta} \left(\frac{H_B}{p_c} \right)^{0.985} + \frac{4b}{k} \sum_{n=1}^{\infty} \frac{1}{n} \left[\int_0^1 \left(\frac{p_c}{p_{av}} \right)^{0.985} \cos(n\pi\bar{y}) d\bar{y} \right]^2 \quad (5.35)$$

The macro-constriction resistance R_2 , for the contact pressure distributions in this study, can be expressed as

$$R_2 = \frac{4b}{k} \sum_{n=1}^{\infty} \frac{1}{n} \left[\int_0^1 \frac{p_c}{p_{av}} \cos(n\pi\bar{y}) d\bar{y} \right]^2 p_c \sum_{i=1}^5 \frac{1}{p_{ci}} \quad (5.36)$$

Thus,

$$R_2 = \frac{4b}{k} \sum_{n=1}^{\infty} \frac{1}{n} \left[\sum_{m=1}^5 \frac{p_{cm}}{p_{av}} \cos\left(\frac{mn\pi}{5}\right) \right]^2 p_c \sum_{i=1}^5 \frac{1}{p_{ci}} \quad (5.37)$$

Using the values of the combined contact pressure obtained from the finite element analysis for various distributions, the relationship functions for each case are obtained.

$$\text{for } h/\ell = 0.5 \text{ and } F = 98N \quad R_{c2} = 2.04 \times 10^{-7} p_c \quad (5.38)$$

$$\text{for } h/\ell = 0.5 \text{ and } F = 294N \quad R_{c2} = 6.63 \times 10^{-8} p_c \quad (5.39)$$

$$\text{for } h/\ell = 0.5 \text{ and } F = 882N \quad R_{c2} = 1.84 \times 10^{-8} p_c \quad (5.40)$$

$$\text{for } h/\ell = 2.0 \text{ and } F = 98N \quad R_{c2} = 1.57 \times 10^{-7} p_c \quad (5.41)$$

$$\text{for } h/\ell = 2.0 \text{ and } F = 294N \quad R_{c2} = 6.89 \times 10^{-8} p_c \quad (5.42)$$

$$\text{for } h/\ell = 2.0 \text{ and } F = 882N \quad R_{c2} = 1.98 \times 10^{-8} p_c \quad (5.43)$$

Thus, the macro-constriction resistance is proportional to the contact pressure distribution:

$$R_2 = C \cdot p_c, \quad (5.44)$$

where C is a coefficient of proportionality.

The maximum value of R_2 is of the order of $10^{-4} m^2 C/kW$. This means that the macro-constriction resistance is negligible in comparison with the thermal contact resistance, R_c , which is of the order of $10^{-2} m^2 C/kW$, a hundred times higher than R_2 .

As indicated in Eq. 5.35, the micro-constriction resistance depends on the material properties and contact surface finish. For the material used in this study, the thermal conductivity was $54 W/m^{\circ}C$, the hardness of material was $160 H_B$, and the slope of the surface irregularity measured from the profilograph Taylor Hobson Talysurf 4 was 0.14 (Fig. 5.28). The roughness of the contact surface was measured by Mitutoyo Surftest 401 as $R_a = 1 \mu m$. Thus, the corresponding standard deviation of the surface is $\sigma_c = 1.2 \mu m$. However, the roughness of the surface calculated from the parts of the profilograph, with omission of extreme values, was determined as $R_a = 0.55 \mu m$, for which the standard deviation value is $\sigma_c = 0.66 \mu m$. Substituting these values for the micro-constriction resistance term of the Mikic formula, Eq. 5.35, one obtains for the general function found in this study

$$\text{for } \sigma_c = 0.66 \mu m \quad R_c = 0.79 \frac{\sigma_c}{k \tan \Theta} \frac{H_B}{p_c} \quad (5.45)$$

$$\text{for } \sigma_c = 1.20 \mu m \quad R_c = 0.45 \frac{\sigma_c}{k \tan \Theta} \frac{H_B}{p_c} \quad (5.46)$$

In order to compare these results with those obtained by Cooper, Mikic and Yovanovich [19], one has to convert them to thermal contact conductance values.

As

$$h_c = \frac{1}{R_c}, \quad (5.47)$$

we have

$$\text{for } \sigma_c = 0.66 \mu m \quad h_c = 1.27 \frac{k \tan \Theta}{\sigma_c} \frac{p_c}{H_B} \quad (5.48)$$

$$\text{for } \sigma_c = 1.20 \mu m \quad h_c = 2.20 \frac{k \tan \Theta}{\sigma_c} \frac{p_c}{H_B} \quad (5.49)$$

Fig. 5.29 is the graph given in [19] with the results obtained by Cooper, Mikic and Yovanovich [19], Mikic and Rohsenow [33], Henry [34], and Yovanovich and Fenech [35], onto which results obtained in this study, converted into the thermal contact conductance, have been plotted. It can be seen that the two plots for $\sigma_c = 0.66 \mu m$ and for $\sigma_c = 1.20 \mu m$ are nearly parallel to the Mikic theoretical function [32], which is in-between them. In particular, the plot of the general function for $\sigma_c = 0.66 \mu m$ shows a very good agreement with the experimental data obtained in [33], [34], and [35].

Chapter 6

Conclusions and Recommendations

6.1 Conclusions

The conclusions which can be derived from this study on the effect of contact pressure distribution on the thermal contact resistance distribution along a machine joint, are as follows:

1. An iterative experimental and finite element modelling approach has been applied to find out the effect of the contact pressure distribution on the thermal contact resistance distribution. In this approach, the thermal field in the finite element model of two contacting specimens subjected to various contact pressure distributions was correlated with the experimental temperature field measurements through consecutive iterations, using initially assumed local values of thermal conductivity converted later into the thermal contact resistance distribution.
2. Experiments were conducted on two thin-plate specimens of steel under plane

stress loading by a concentrated force acting on the upper, smaller specimen. Its height-to-length ratio defined its stiffness and thus, the profile of the contact pressure distribution. Two upper specimens of $h/l = 0.5$ and 2.0 used in the experiments provided convex and concave contact pressure distributions respectively, while the variation of loading force provided various levels of contact pressure distribution. Six profiles of contact pressure distributions were generated. In condition of heat transfer across the interface, corresponding thermal contact resistance distributions caused the temperature drop across the interface which was found to be between $0.1\text{ }^{\circ}\text{C}$ and $3.6\text{ }^{\circ}\text{C}$ for contact pressure 6303 kPa and 835 kPa respectively.

3. Thermal contact resistance distribution was determined for the combined mechanical contact pressure and thermal contact stress distributions. For the experimental conditions used, the effect of thermal contact stresses was the redistribution of the total contact pressure at the interface. This effect was found to be significant for the low loading condition, for which it amounted on average for thirty five percent.

4. The function representing the relationship between thermal contact resistance and contact pressure for various distributions was defined using the least squares method. It was revealed that although this relationship can be expressed by the single function for the whole experimental range, the deviations experienced for different slopes and forms of distributions (convex and concave), noticeable particularly for steep slopes at high contact pressure levels, could indicate the effect of macro-constriction resistance, however small its values according to the theoretical calculations might be.

5. The results are validated by comparison with published data on thermal contact conductance, both theoretical and experimental. The linearity of the general function for thermal contact conductance (in log-log coordinates) obtained from the R_c vs. p_c distributions, and its near parallelity to the Mikic theoretical function for

micro-constriction conductance, indicate the negligible effect of macro-constriction resistance. However, the deviation from the straight line of the general function (log-log coordinates) of the individual R_c vs. p_c curves obtained from the distributions of the thermal contact resistance and contact pressure along the interface, which indicates the possibility of the effect of macro-constriction resistance, requires further study to better understand this phenomenon.

6.2 Recommendations for Future Studies

On the basis of the work presented, it is proposed that the following aspects be considered for future research.

1. It is recommended to undertake experimental studies which would permit to determine the significance of macro-constriction resistance and its contribution to the effect which contact pressure distribution has on thermal contact resistance distribution.
2. Since only two different h/ℓ ratios are used in the experiments, it is recommended that specimens with different h/ℓ ratios be used to generate different pressure distributions. The results would lead to formulation of the relationship between the thermal contact resistance and contact pressure distributions.
3. The function was defined for a specific material and surface roughness. It is suggested to conduct experiments with different materials and surface roughness which would permit to determine the effect of these parameters on the relationship function.

Bibliography

- [1] Zawistowski, F., "Temperature Controlled Machine Tools", *Microtechnic* 19, Nr. 6, 1965, pp. 336-340.
- [2] Spur, G., "Konstruktive Gestaltung und Automatisierung der Werkzeugmaschine", *Industrie - Anzeiger*, 90 Jg, Nr. 67 v. 20, 1968.
- [3] Attia, M. H. and Kops, L., "Nonlinear Thermoelastic Behaviour of Structural Joints - Solution to a Missing Link for Prediction of Thermal Deformation of Machine Tools", *ASME, J. of Eng. for Ind.*, Vol. 101, 1979.
- [4] Attia, M. H. and Kops, L., "Importance of Contact Pressure Distribution on Heat Transfer in Structural Joints of Machine Tools", *Trans. of ASME, J. of Eng. for Ind.*, Vol. 102, 1980, pp. 159-167.
- [5] Personal Communication between Attia, M. H. and Yovanovich, M. M., April, 1976.
- [6] Laming, L. C., "Thermal Conductance of Machined Metal Surfaces", *ASME Int. Heat Transfer Symposium*, Boulder, Sept. 1961 pp. 65-71.
- [7] Jakob, M., *Heat Transfer*. Chapman and Hall, 1949.
- [8] Yovanovich, M. M., "Thermal Contact Resistance, Theory and Application", Lecture Notes, Waterloo University, Ont., Canada, 1967.

- [9] Attia, M. H., "Effect of Structural Joints on Thermal Deformation of Machine Tools", *Ph.D Thesis, McGill University*, 1978.
- [10] Kaminskaya, V., Levina, Z.M. and Reshetov, D.N., "Bodies and Body Components of Metal Cutting Machine Tools, Calculation and Design". Vol. 2, National Lending Library for Science and Technology, Boston Spa., Yorkshire, 1964.
- [11] Den Hartog, J.P., *Advanced Strength of Materials*. McGraw-Hill Book Co., Inc., 1952
- [12] Heteyi, M., *Beams on Elastic Foundation*. John Wiley & Sons Canada, Ltd., 1974
- [13] Thomas, T. R. and Probert, S., "Thermal Contact Resistance: the Directional Effect and Other Problems", *Int. J. Heat Mass Transfer*, Vol. 13, 1970.
- [14] Mikic, B. and Carnasciali, G., "The Effect of Thermal Conductivity of Plating Material on Thermal Contact Resistance". *Trans. ASME, J. Heat Transfer*, Vol. 92, 1970.
- [15] Yovanovich, M. M., "On the Temperature Distribution and Constriction Resistance in Layered Media", *J. Composite Materials*, Vol. 4, 1970.
- [16] Mikic, B. B. and Mate, C. F., "Thermal Contact Resistance", MIT, M.E. Tech. Report 4542-41, 1966.
- [17] Veziroglu, T. N., Yucu, H. and Kakac, S., "Analysis of Thermal Conductance of Contacts with Interstitial Plates", *Int. J. Heat Mass Transfer*, Vol. 19, 1976.
- [18] Howard, J. R., "An Experimental Study of Heat Transfer Through Periodically Contacting Surfaces", *Int. J. Heat Mass Transfer*, Vol. 19, 1976.

- [19] Cooper, M. G., Mikic, B. B. and Yovanovich, M. M., "Thermal Contact Conductance", *Int. J. Heat Mass Transfer*, Vol. 12, 1969, pp. 279-300.
- [20] Fletcher, L. S. and Gurog, D. A., "Prediction of Thermal Contact Conductance Between Similar Metal Surfaces", Paper 70-852, AIAA 5th Thermal Dynamics Conference, Los Angeles, Calif., June 1970.
- [21] Thomas, T.R., "Extrapolation Errors in Thermal Contact Resistance Measurements", *Trans ASME, J. Heat Transfer*, Vol. 87, May 1965, pp. 243-251.
- [22] Grocht, M. M., *Photoelasticity*, Vol. 2, John Wiley and Sons, New York, 1961.
- [23] Attia, M. H. and Kops, L., "System Approach to the Thermal Behaviour and Deformation of Machine Tool Structures in Response to the Effect of Fixed Joints", *J. Eng. for Industry ASME*, Vol. 30, 1983.
- [24] Attia, M. H. and Kops, L., "A New Method for Determining the Thermal Contact Resistance at Machine Tool Joints", *annals of the CIRP*, Vol. 30, 1981.
- [25] Attia, M. H. and Kops, L., "Computer Simulation of Nonlinear Thermoelastic Behaviour of a Joint in Machine Tool Structure and its Effect on Thermal Deformation", *J. Eng. for Industry ASME*, Vol. 101, 1979.
- [26] Cheung, Y.K. and Zienkiewicz, O.C., "Plates and Tanks on Elastic Foundation - An Application of Finite Element Method", *Int. J. Solids Structures*, Vol. 1, 1965
- [27] Svec, O.J. and Gladwell, G.M., "A Triangular Plate Bending Element for Contact Problems", *Int. J. Solids Structures*, Vol. 9, 1973
- [28] Attia, M.H. and Kops, L., "Distortion in Thermal Field Around Inserted Thermocouples in Experimental Interfacial Studies - Part II: Effect of the Heat Flow Through the Thermocouple", *ASME J. of Eng. for Industry*, Vol. 58, 1987.

- [29] Attia, M.H. and Kops, L., "Distortion in Thermal Field Around Inserted Thermocouples in Experimental Interfacial Studies", *ASME J. of Eng. for Industry*. Vol. 108, 1986.
- [30] User's Manual of ALGOR.
- [31] Personal Communication between Li, W. and Attia, M.H., January, 1993.
- [32] Mikic, B.B., "Thermal Constriction Resistance due to Non-Uniform Surface Conditions", *Int. J. Heat Mass Transfer*, Vol. 13, 1970.
- [33] Mikic, B.B. and Rohsenow, W.M., "Thermal Contact Resistance", *M.I.T Rep.*, No. 4542-41, 1966.
- [34] Henry, J.J., "Thermal Contact Resistance", *A.E.C. Rep.*, No. 2079-2, M.I.T., 1964.
- [35] Yovanovich, M.M. and Fenech, H., "Thermal contact conductance of nominally flat rough surfaces in a vacuum environment", *Prog. Astronaut & Aeronaut.* 18. 733, 1966.

Appendix A

Figures

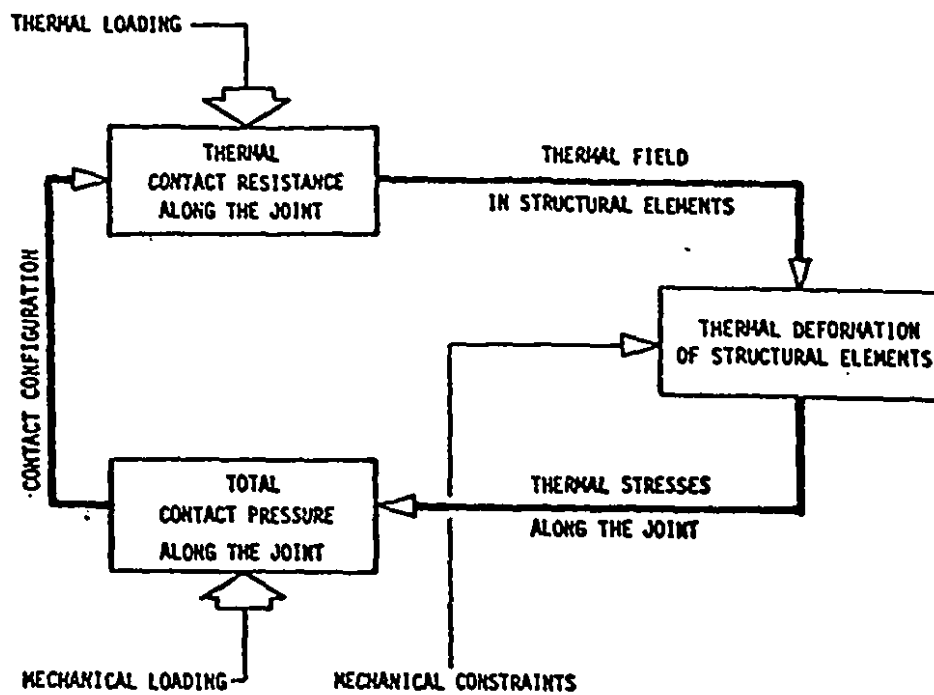


Fig. 1.1 Schematic representation of the time-dependent closed-loop interaction at machine joint [3].

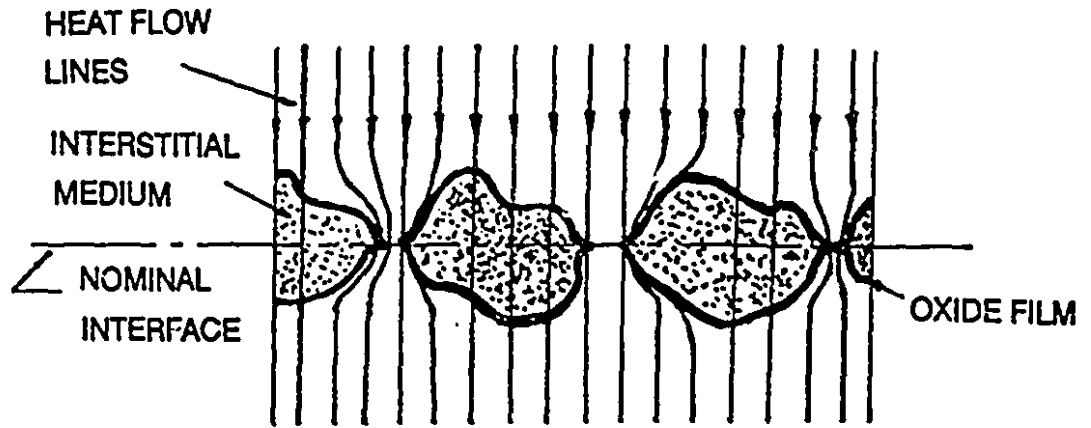


Fig. 2.1 Contact configuration and heat flow constriction across the joint.

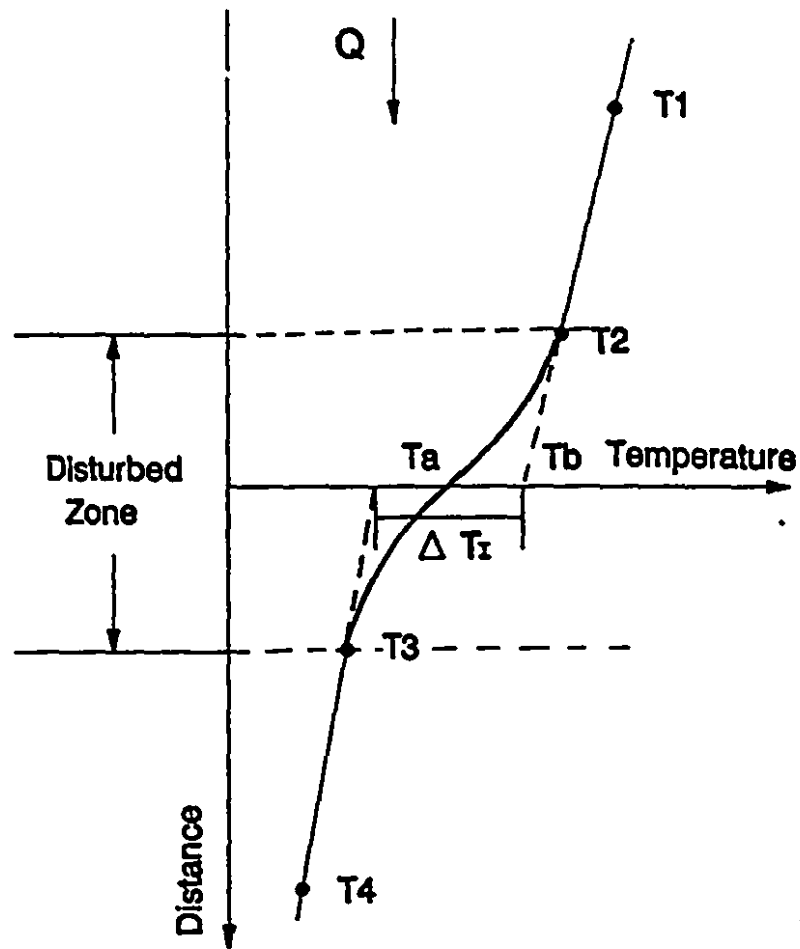


Fig. 2.2 Temperature distribution across the interface.

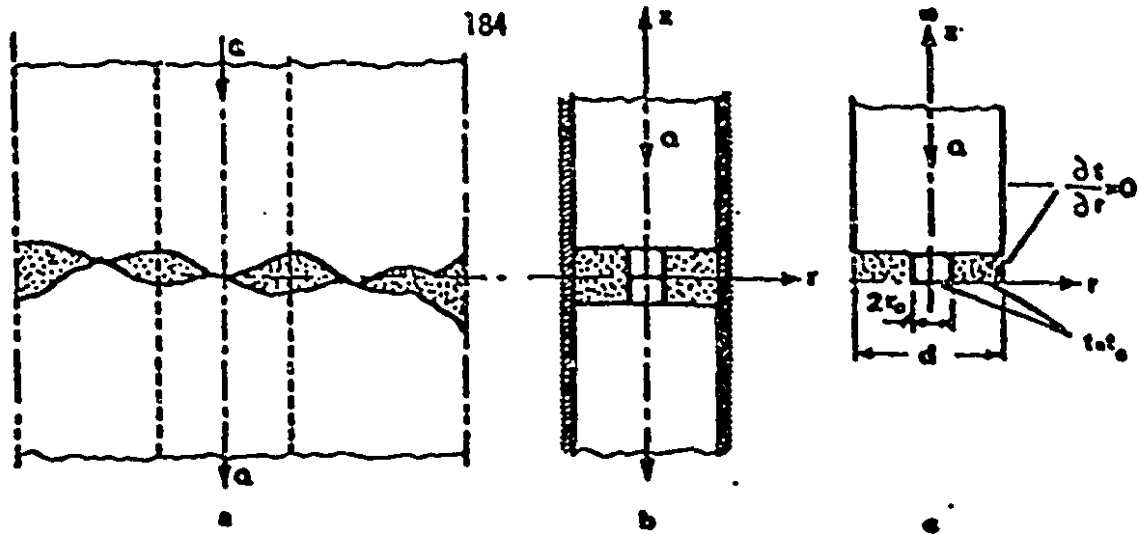


Fig. 2.3 Representation of the disc-constriction model: a - Bodies in real contact; b - Idealized unit cell; c - Thermal boundary conditions [14].

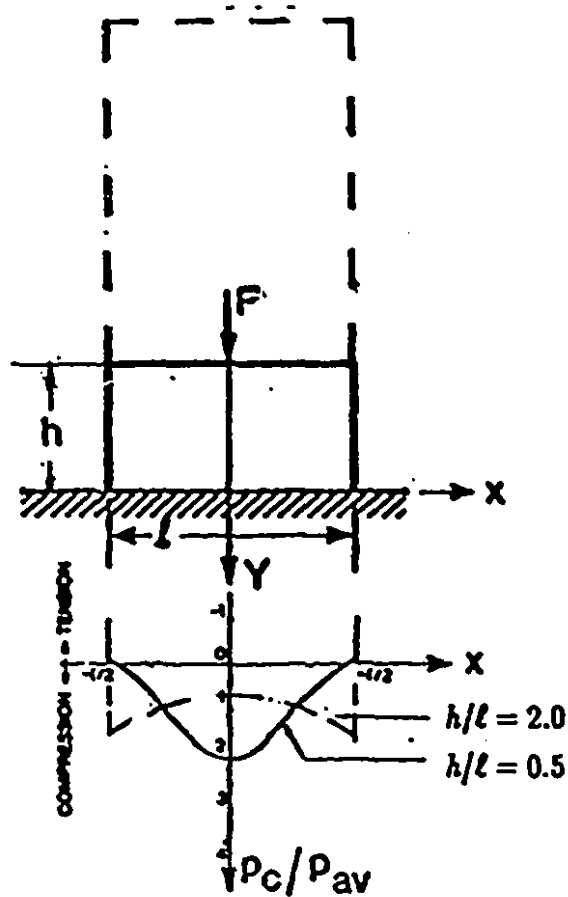


Fig. 3.1 Contact pressure distributions along the interface with different h/l ratios.

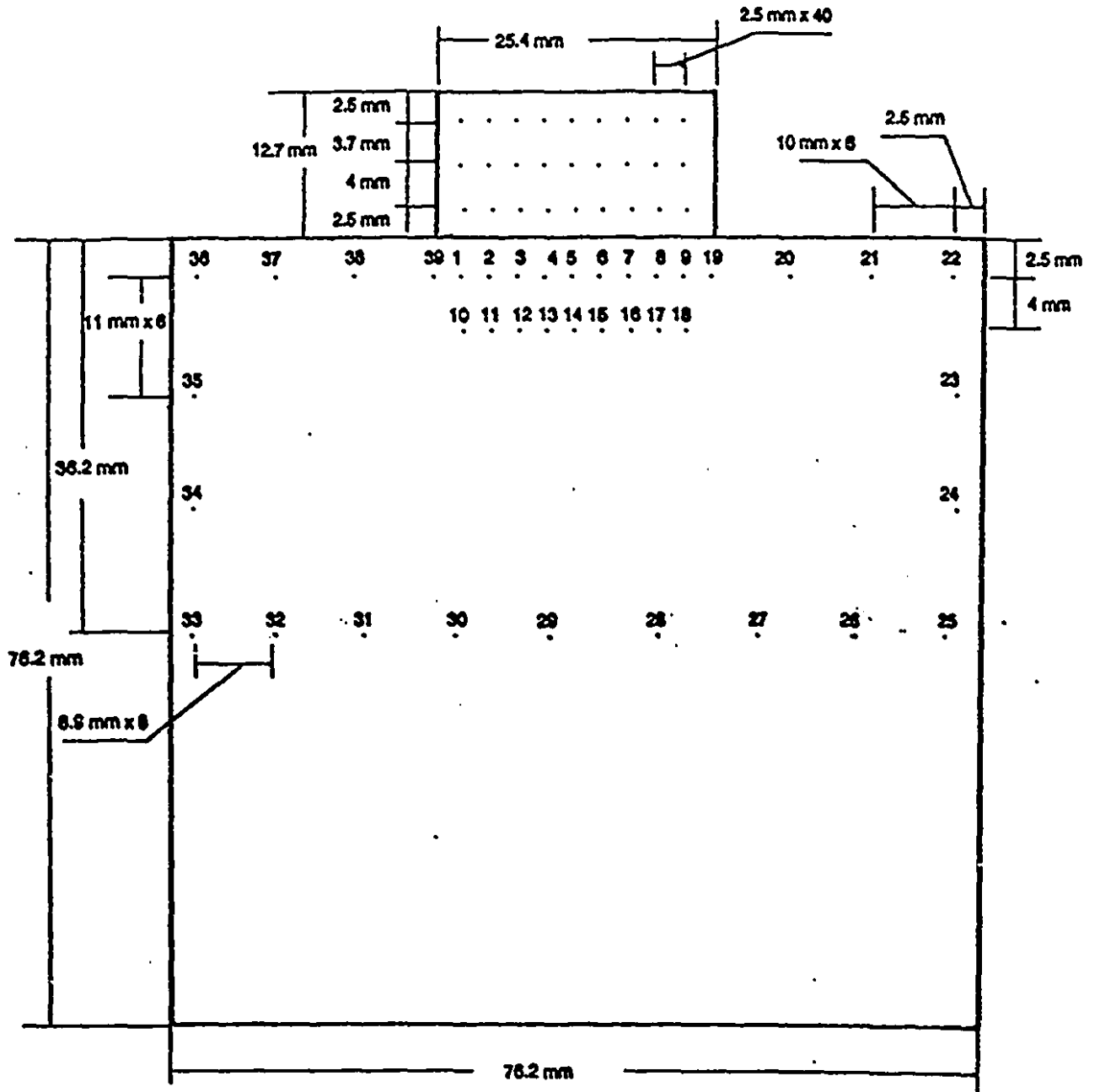


Fig. 3.2 Experimental thermocouple distribution $h/l=0.5$.

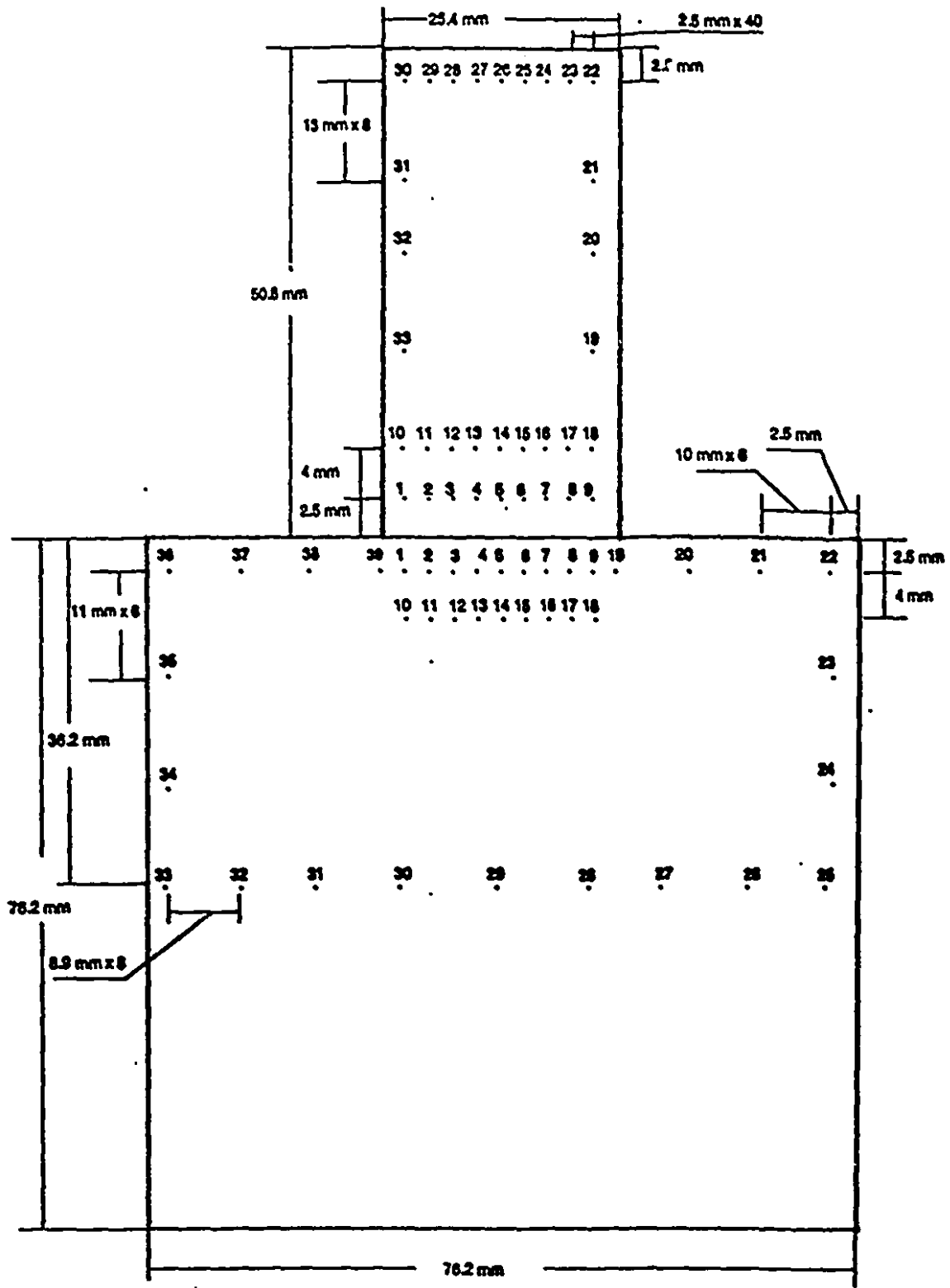


Fig. 3.3 Experimental thermocouple distribution $h/l=2.0$.

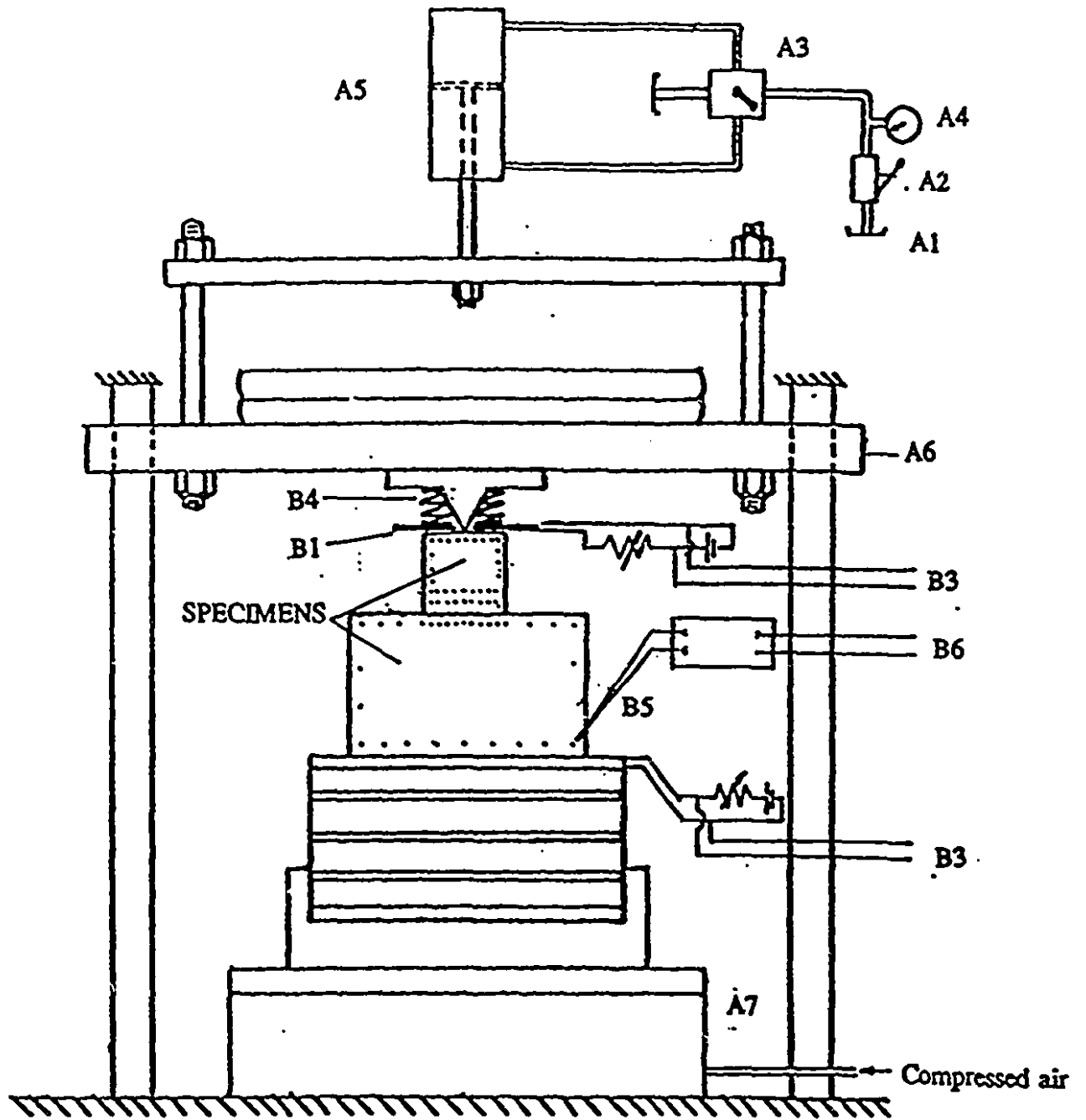


Fig. 3.4 Schematic representation of the test rig.

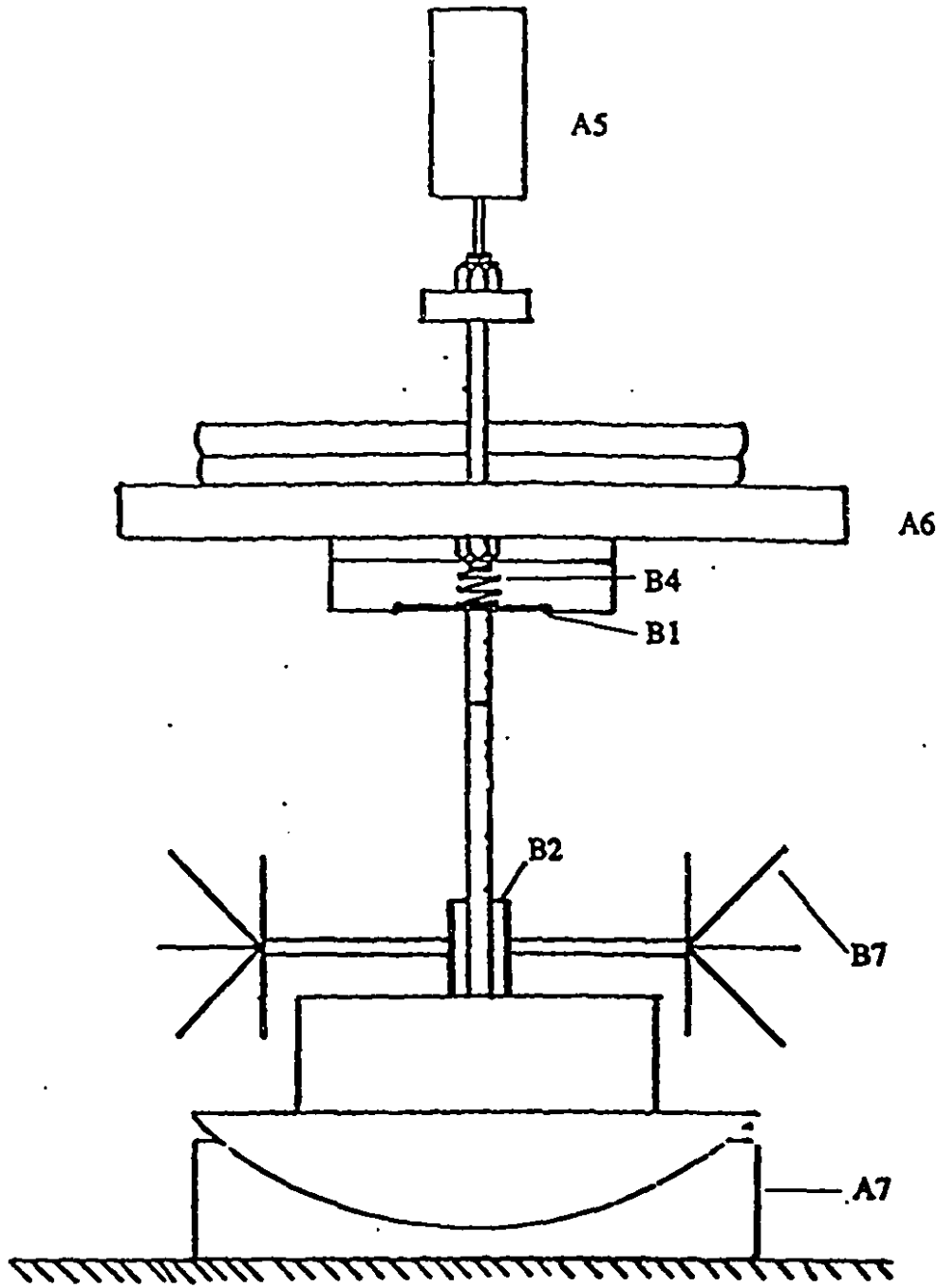


Fig. 3.5 Side view of the test rig.

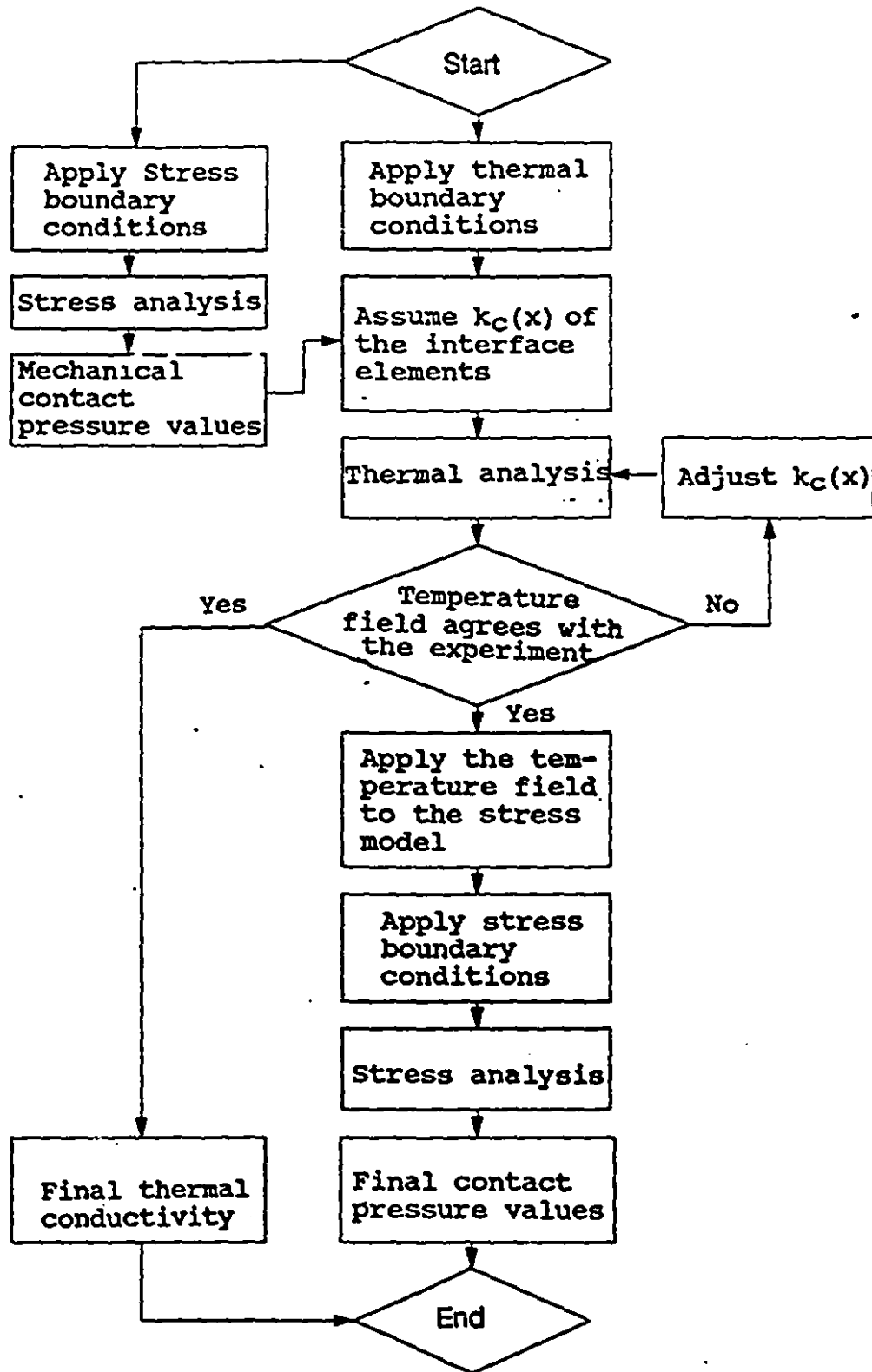


Fig. 4.1 Schematic representation of the closed-loop computer iteration.

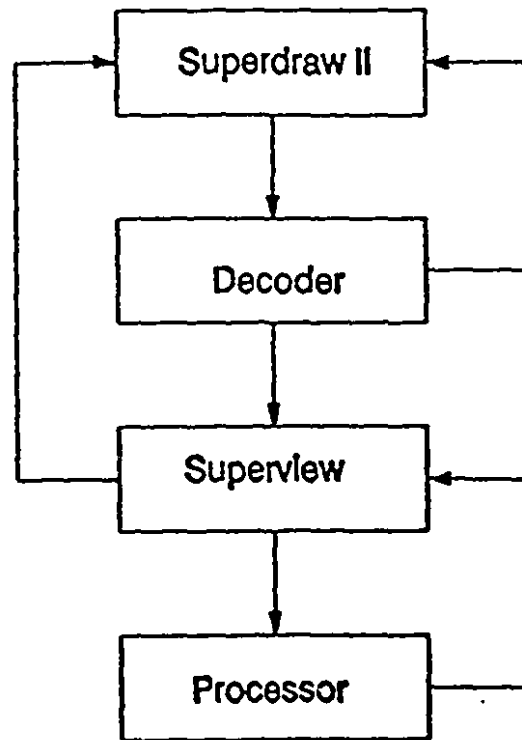


Fig. 4.2 Finite element analysis procedure in ALGOR.

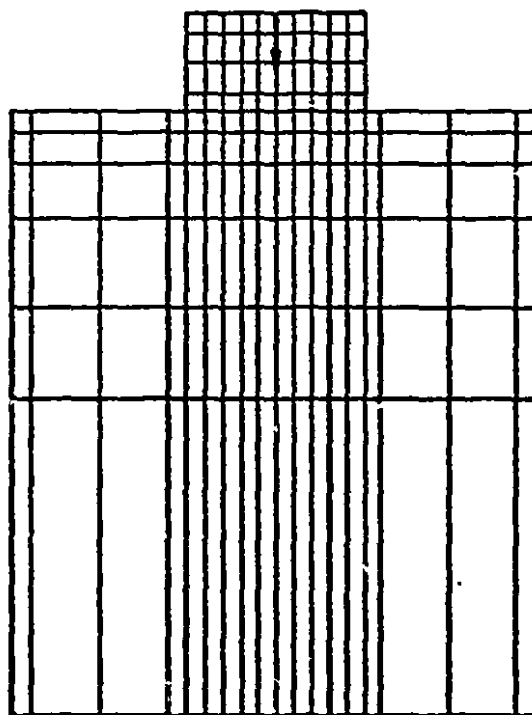


Fig. 4.3 Finite element model for $h/l=0.5$.

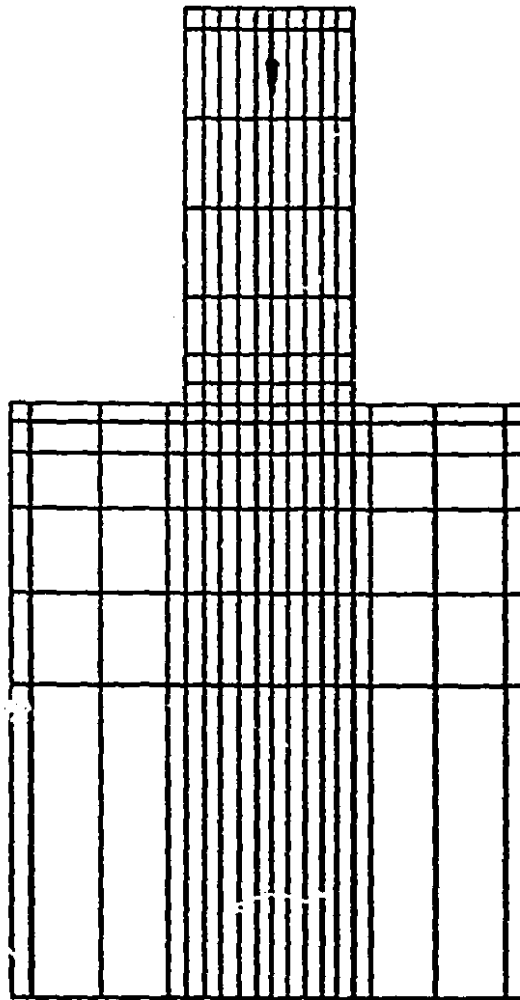


Fig. 4.4 Finite element model for $h/l=2.0$.

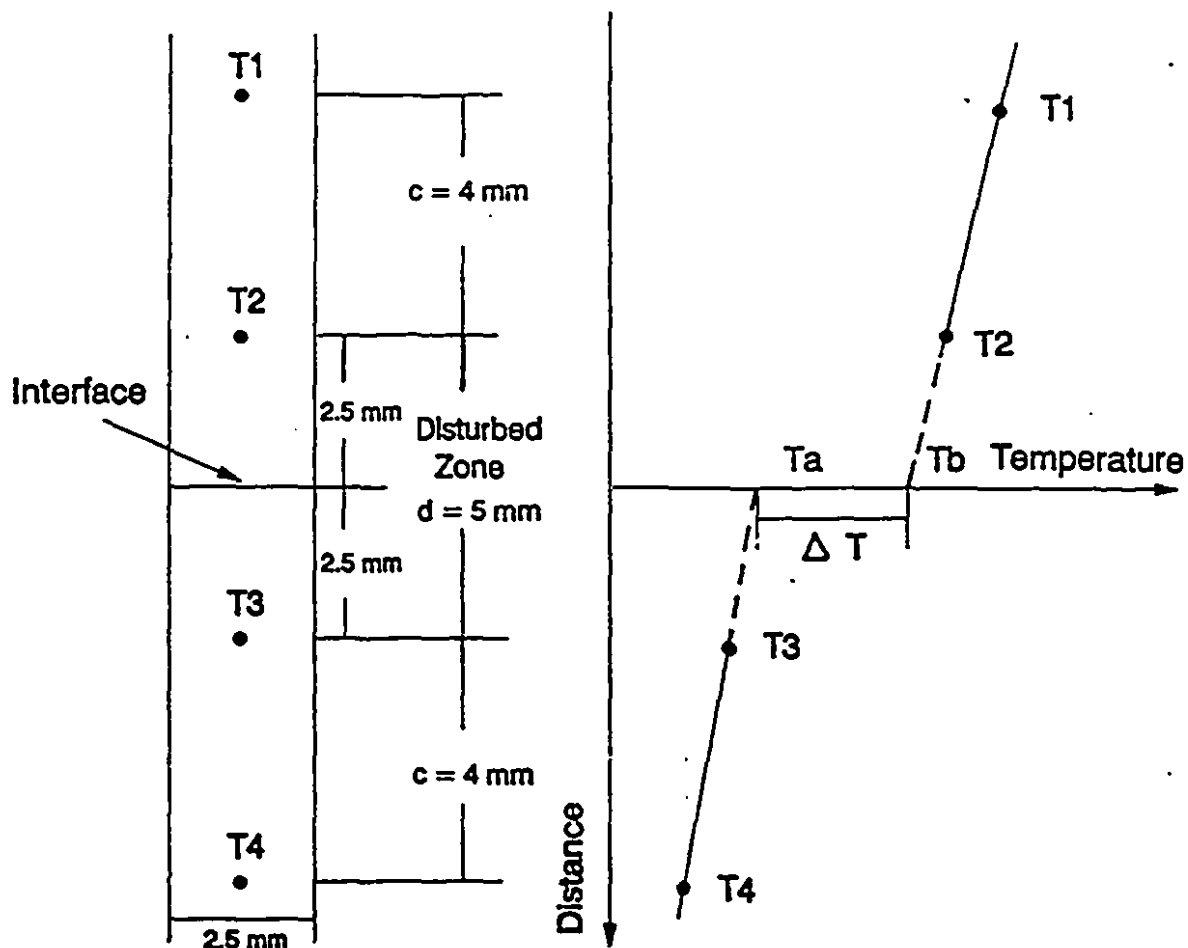


Fig. 4.5 Model of one-dimensional channel temperature distribution across the interface.

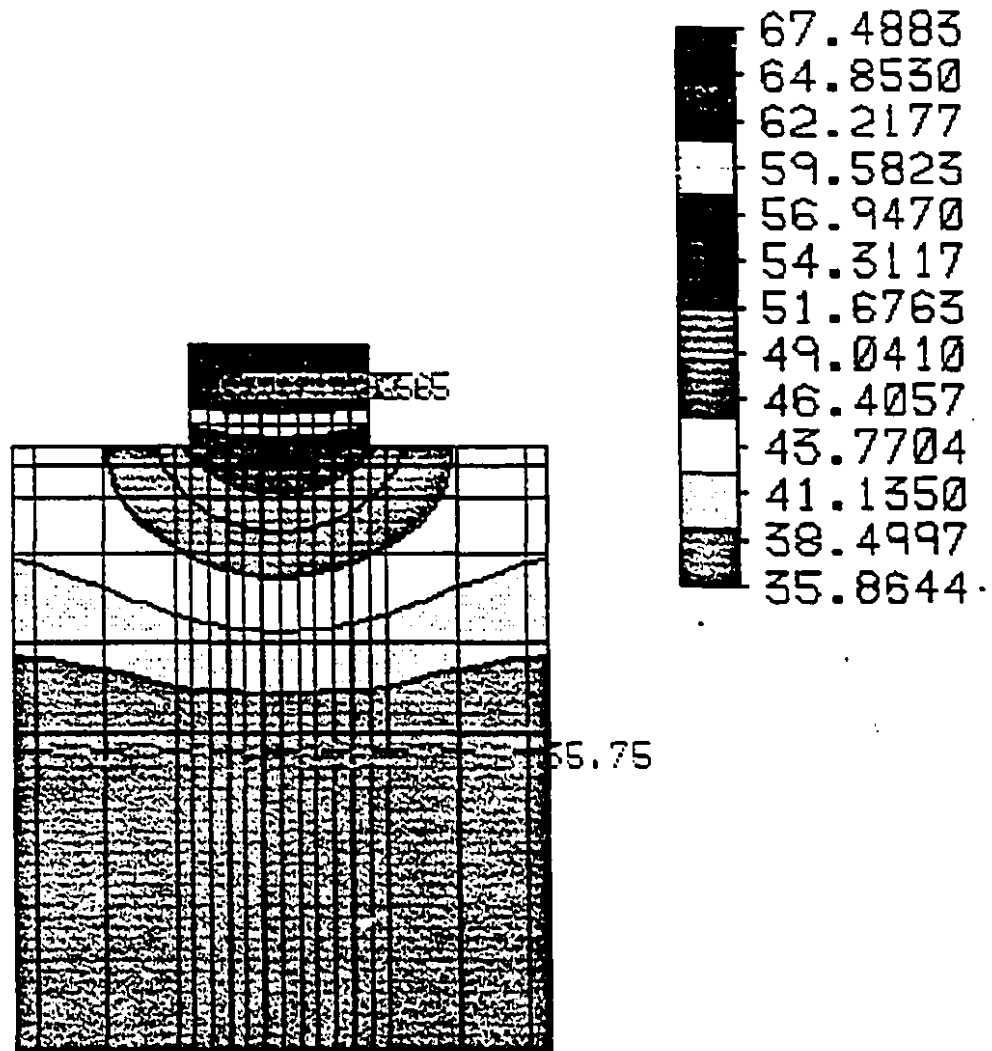


Fig. 5.1 Temperature field on the finite element model for $h/l=0.5$ $F=294N$.

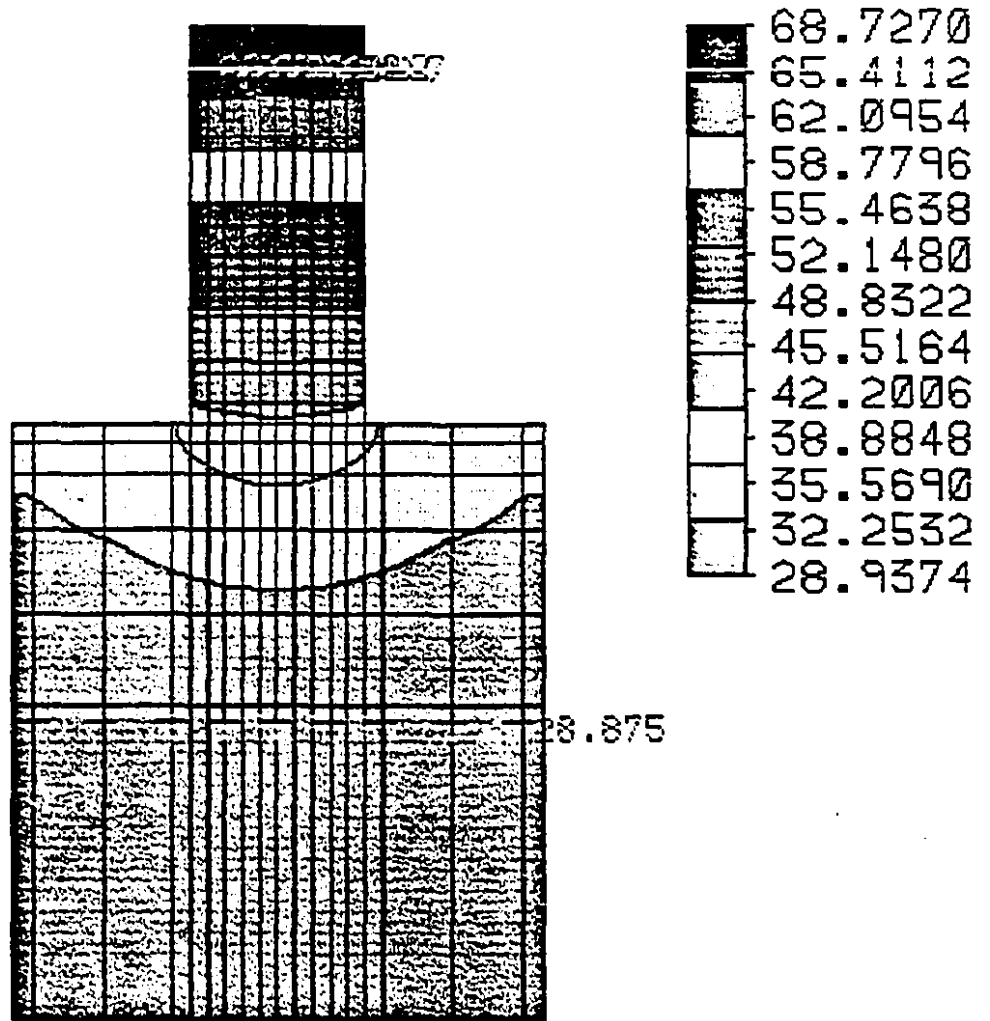


Fig. 5.2 Temperature field on the finite element model for $h/l=2.0$ $F=294N$.

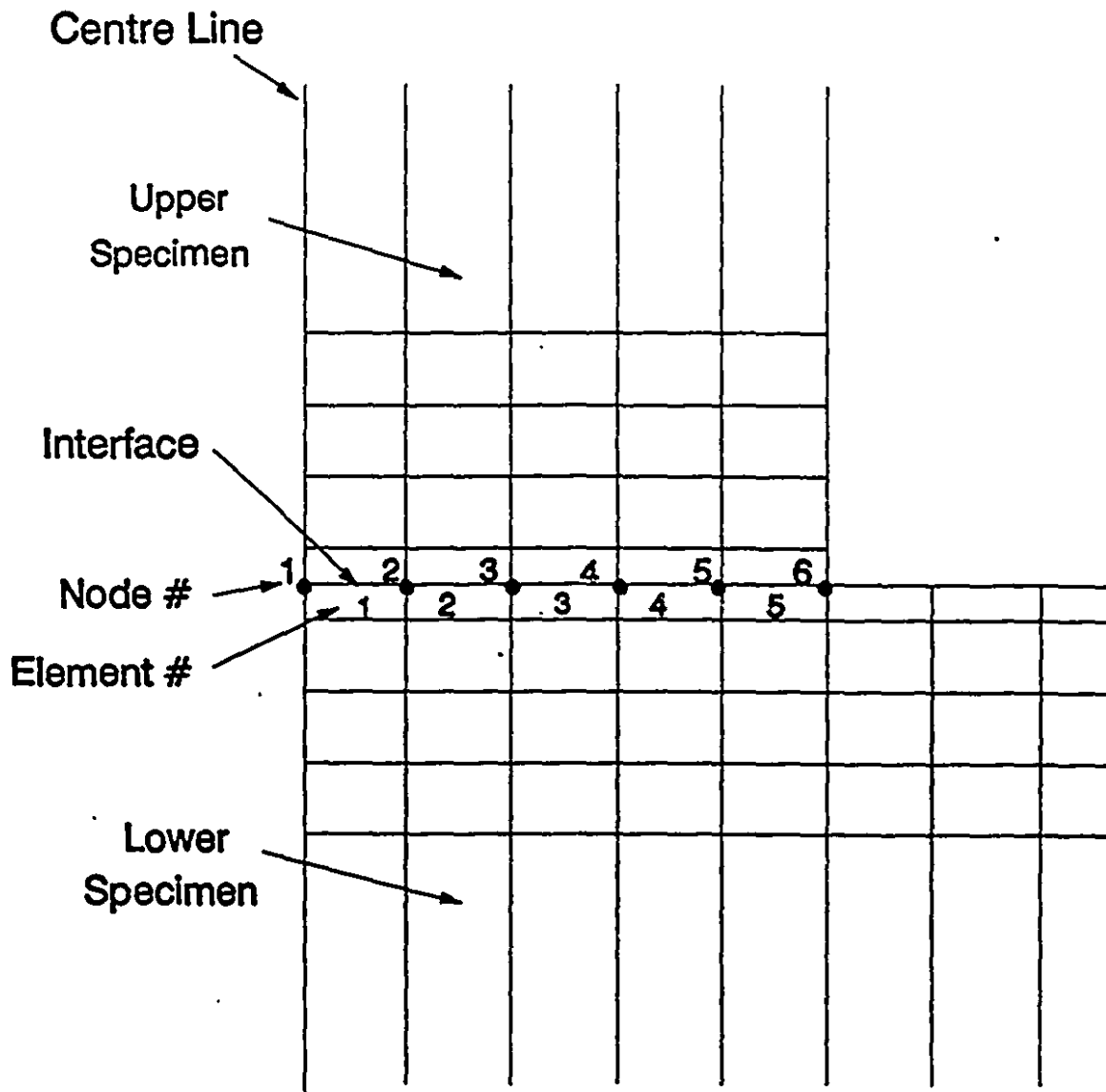


Fig. 5.3 Interface area of the finite element model.

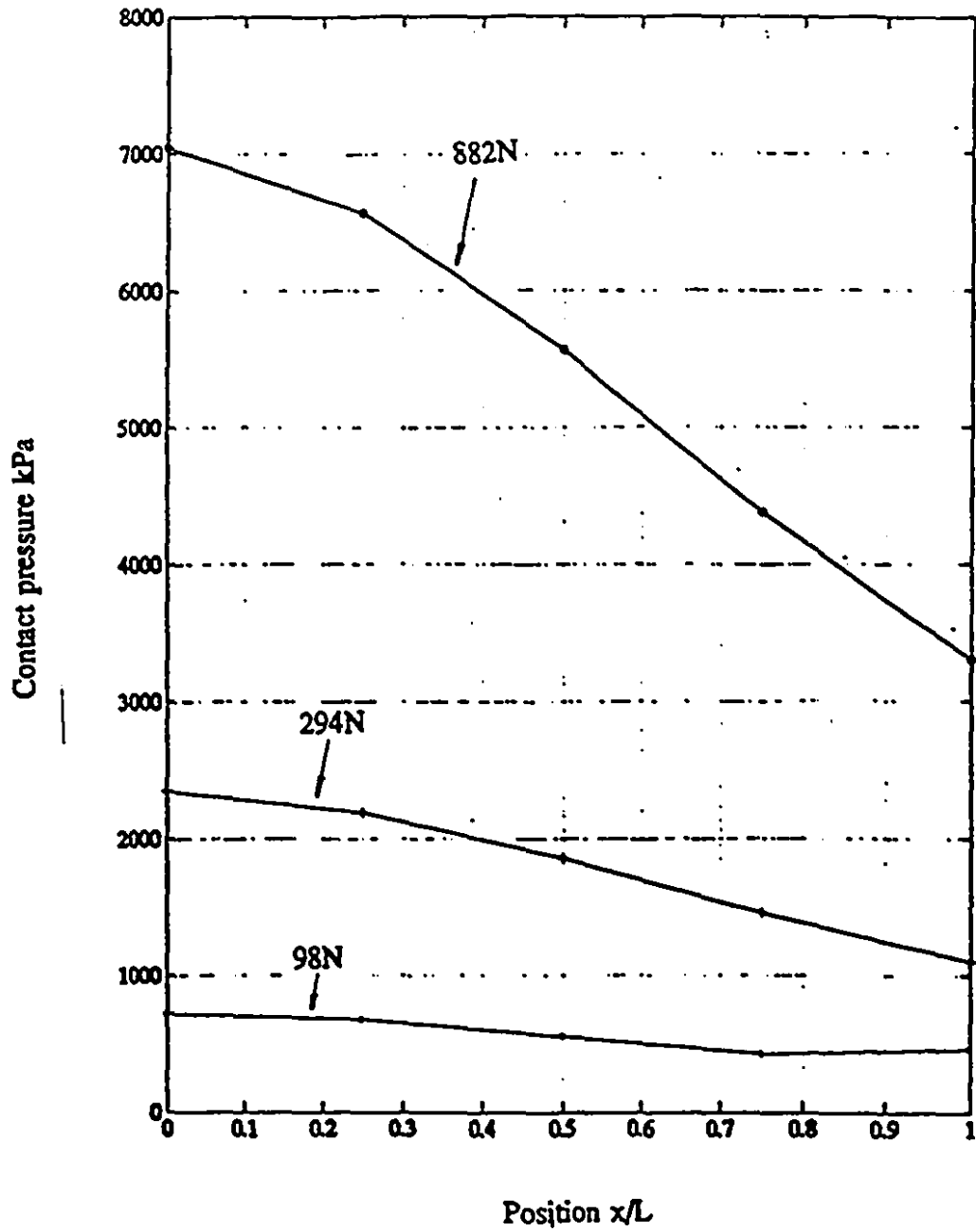


Fig. 5.4 Mechanical contact pressure distribution along the half-length interface from the axis of symmetry for $h/l=0.5$.

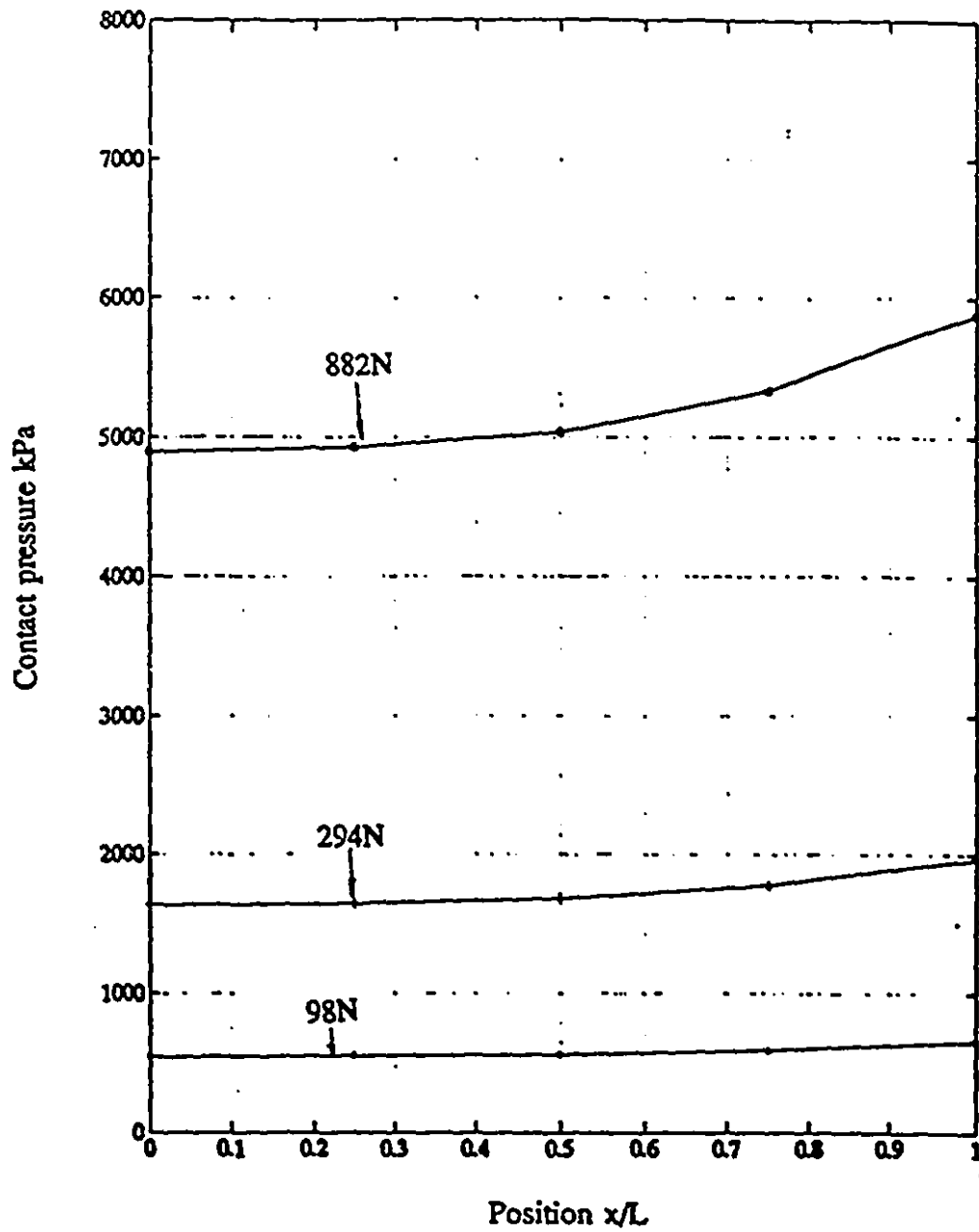


Fig. 5.5 Mechanical contact pressure distribution along the half-length interface from the axis of symmetry for $h/l=2.0$.

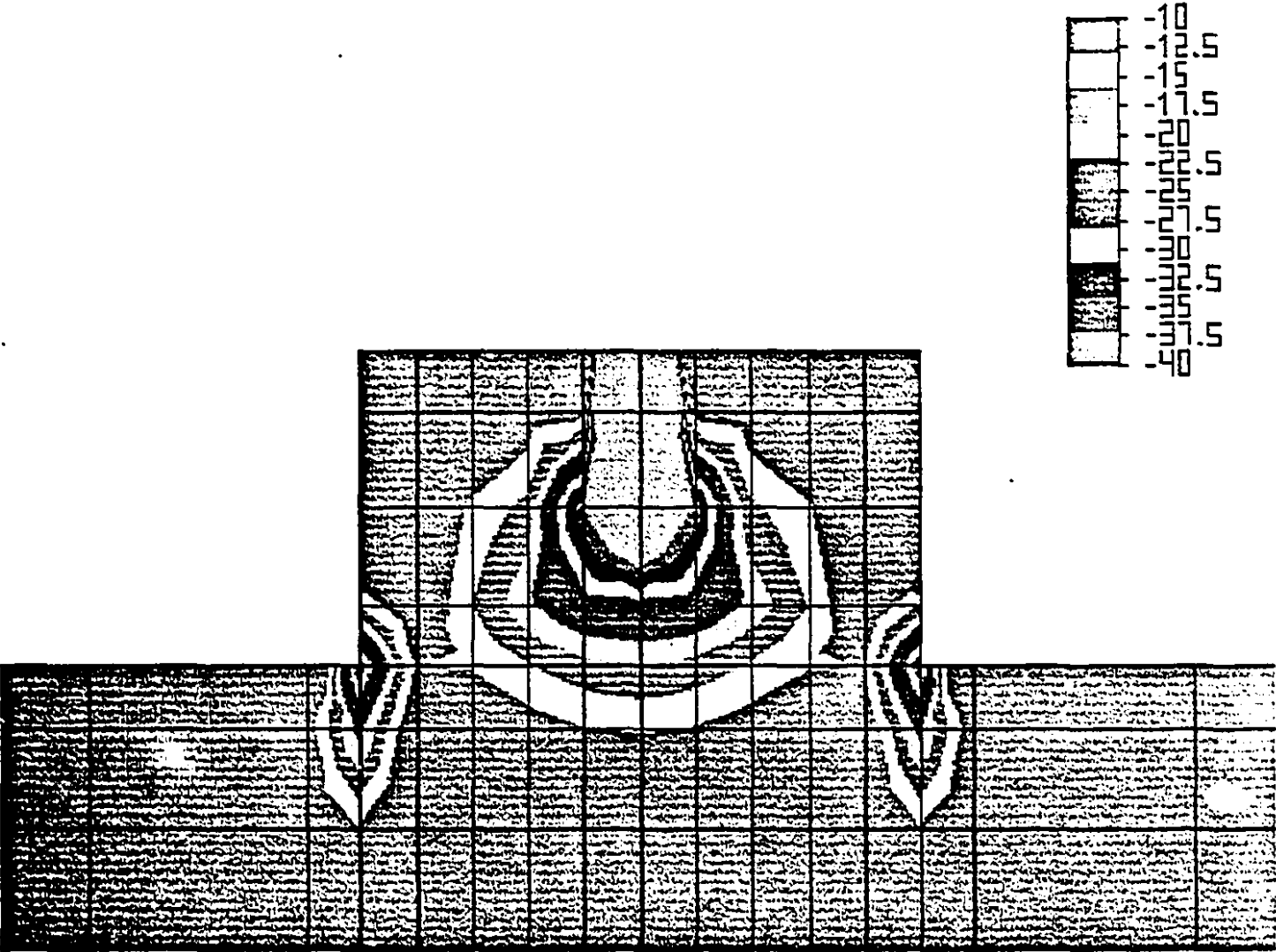


Fig. 5.6 Close view of the stress field of the interface area for $h/l=0.5$.

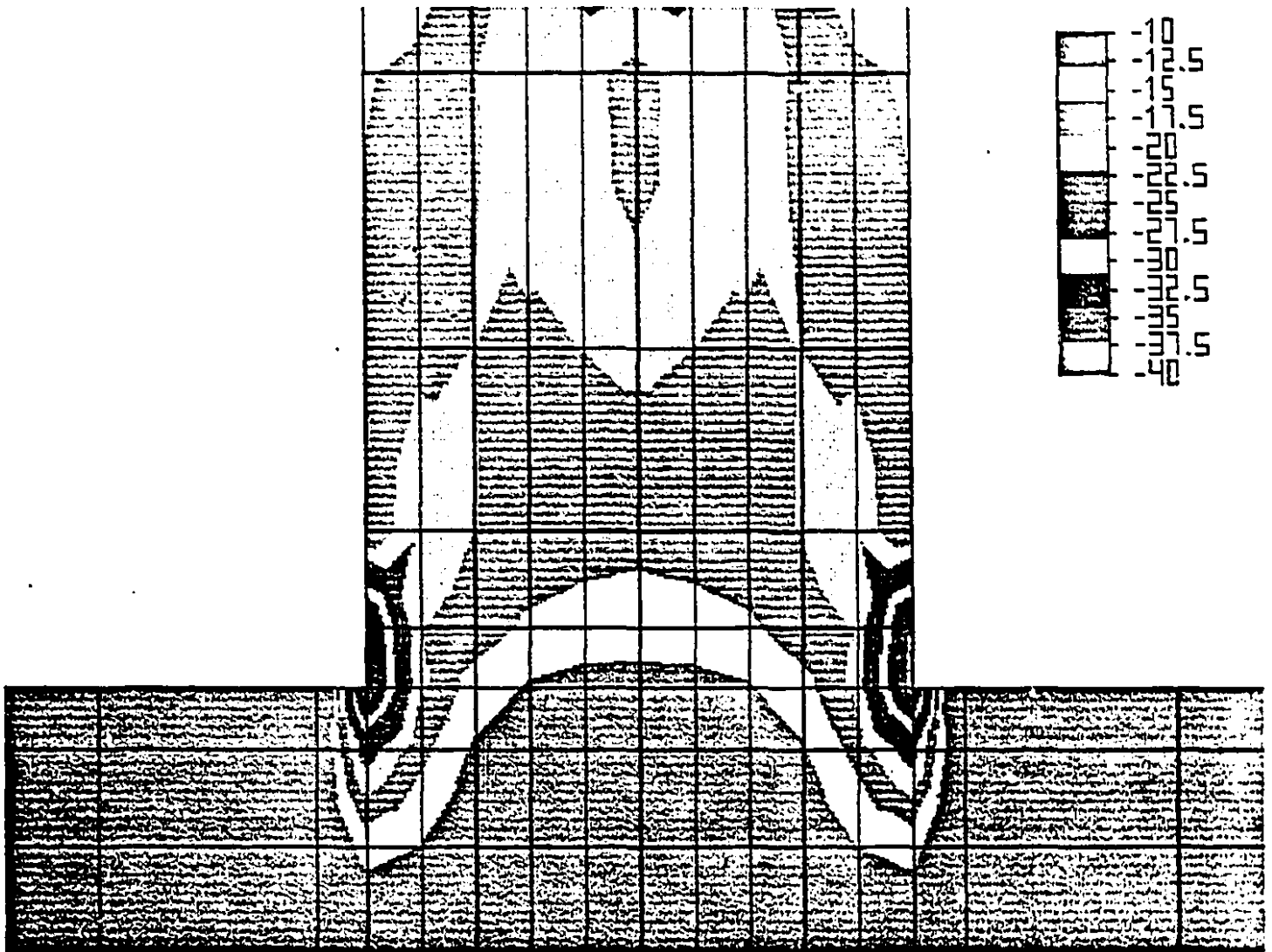


Fig. 5.7 Close view of the stress field of the interface area for $h/l=2.0$.

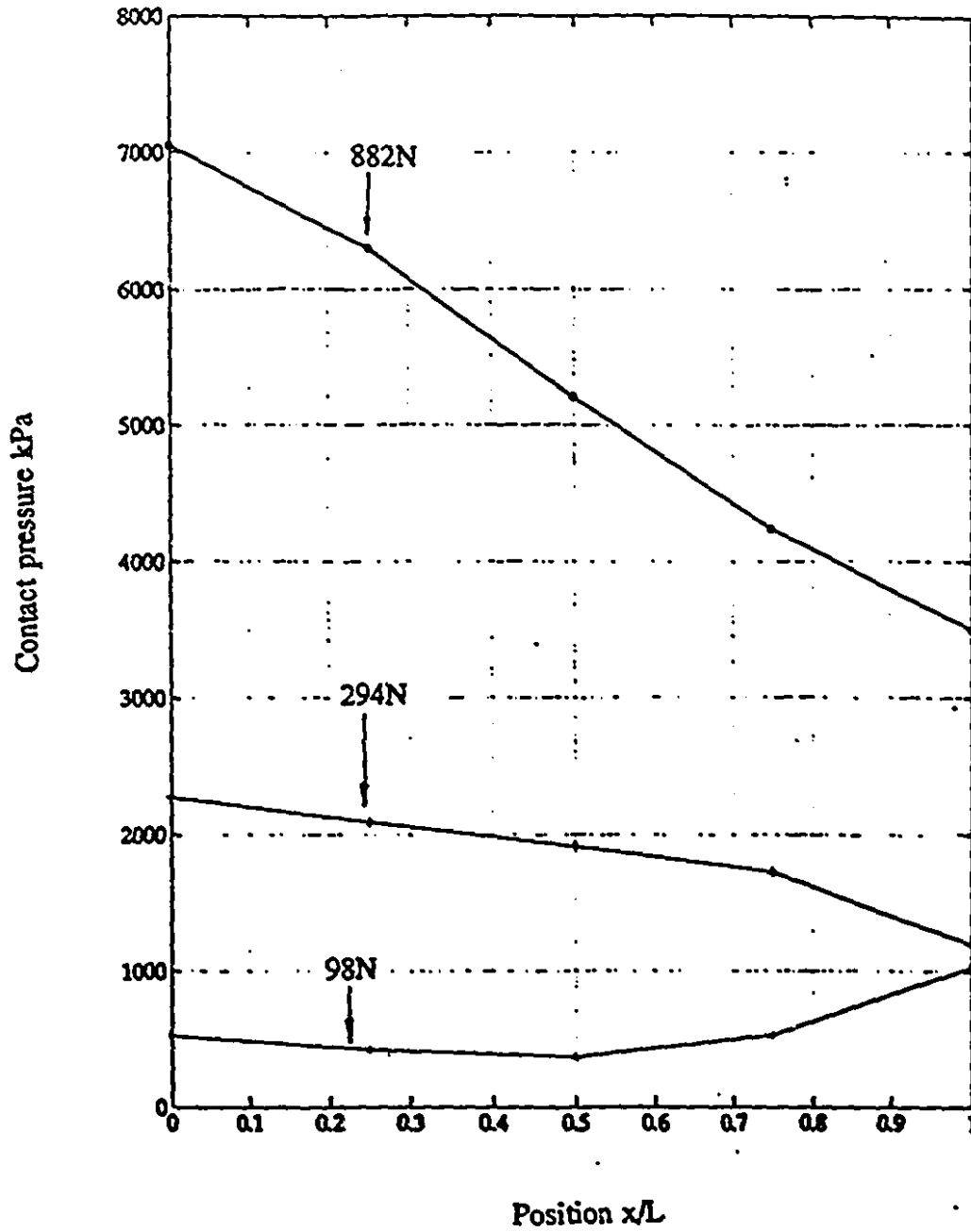


Fig. 5.8 Combined (mechanical and thermal) contact pressure distribution along the half-length interface from the axis of symmetry for $h/l=0.5$.

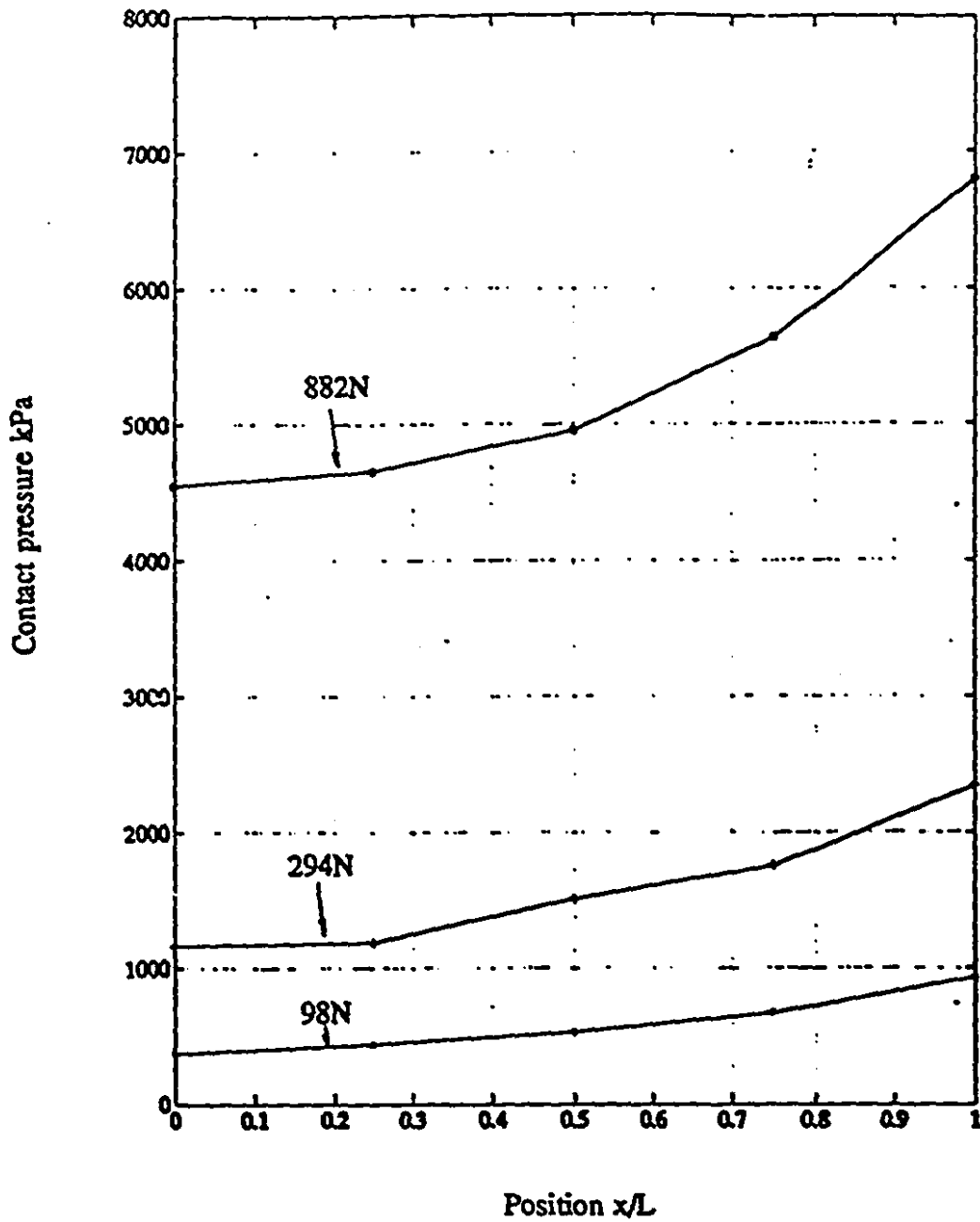


Fig. 5.9 Combined (mechanical and thermal) contact pressure distribution along the half-length interface from the axis of symmetry for $h/l=2.0$.

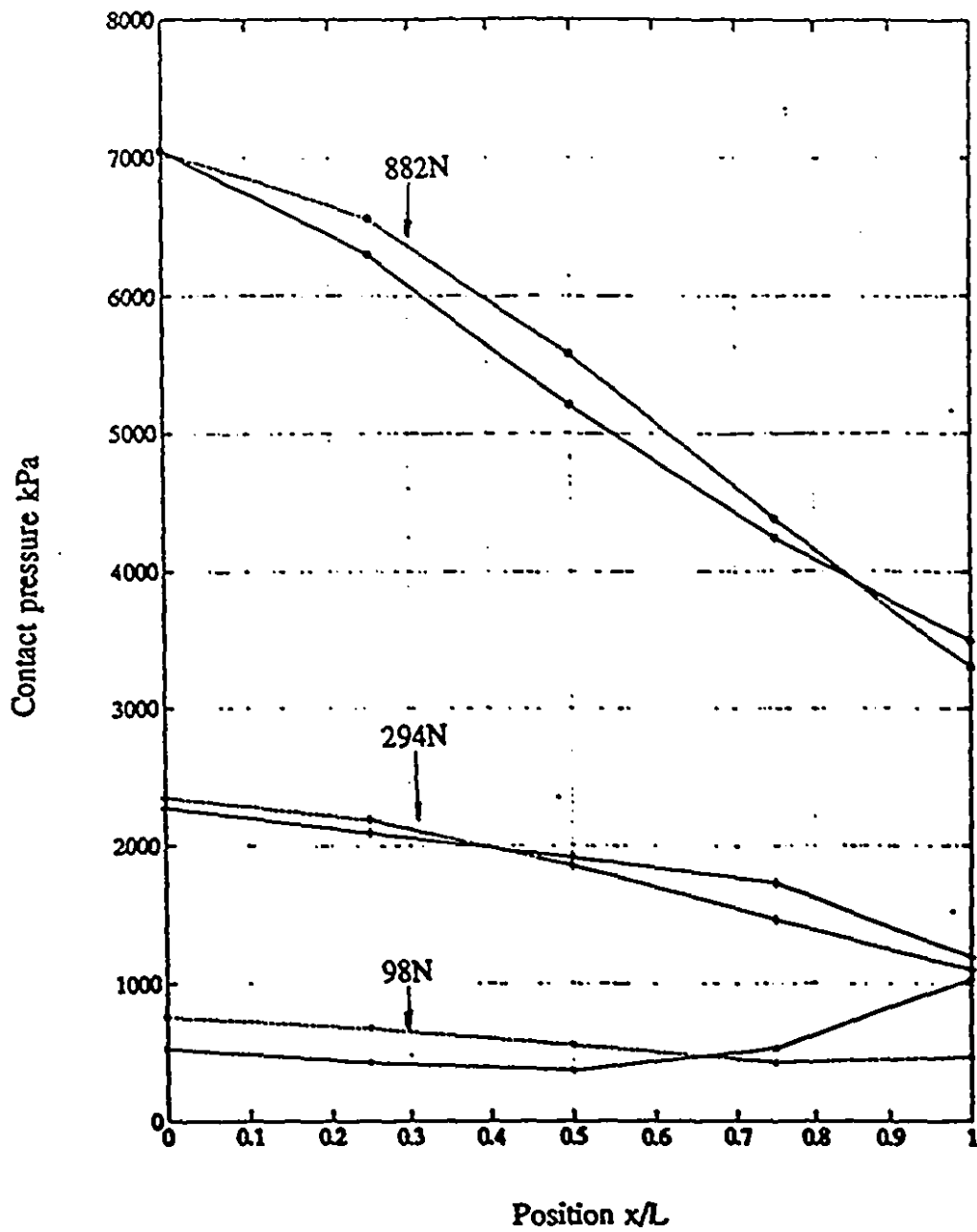


Fig. 5.10 Comparison of combined contact pressure distribution and mechanical-only contact pressure distribution for $h/l=0.5$:

- combined contact pressure
- - - mechanical contact pressure

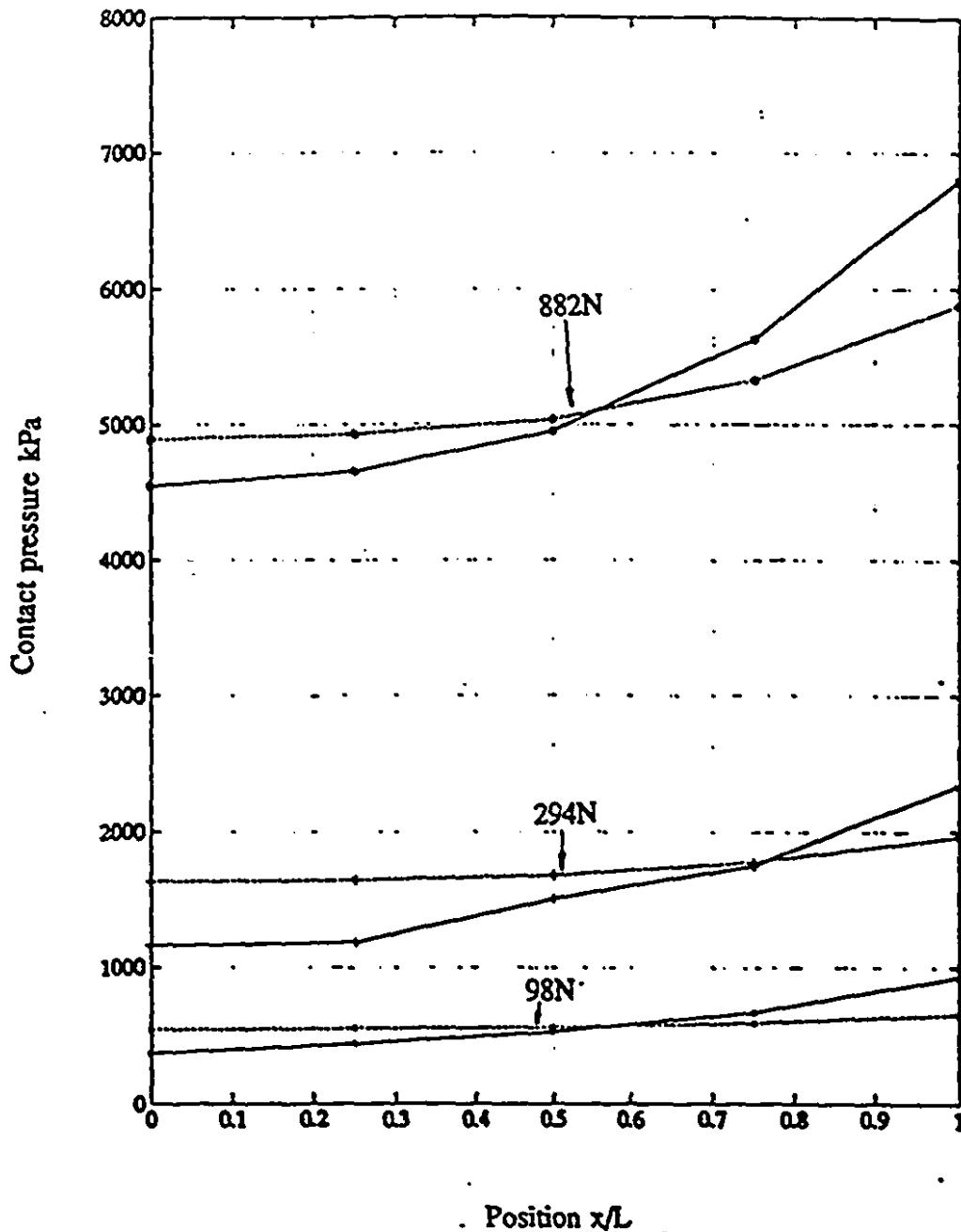


Fig. 5.11 Comparison of combined contact pressure distribution and mechanical-only contact pressure distribution for $h/l=2.0$:
 — combined contact pressure
 - - - mechanical contact pressure

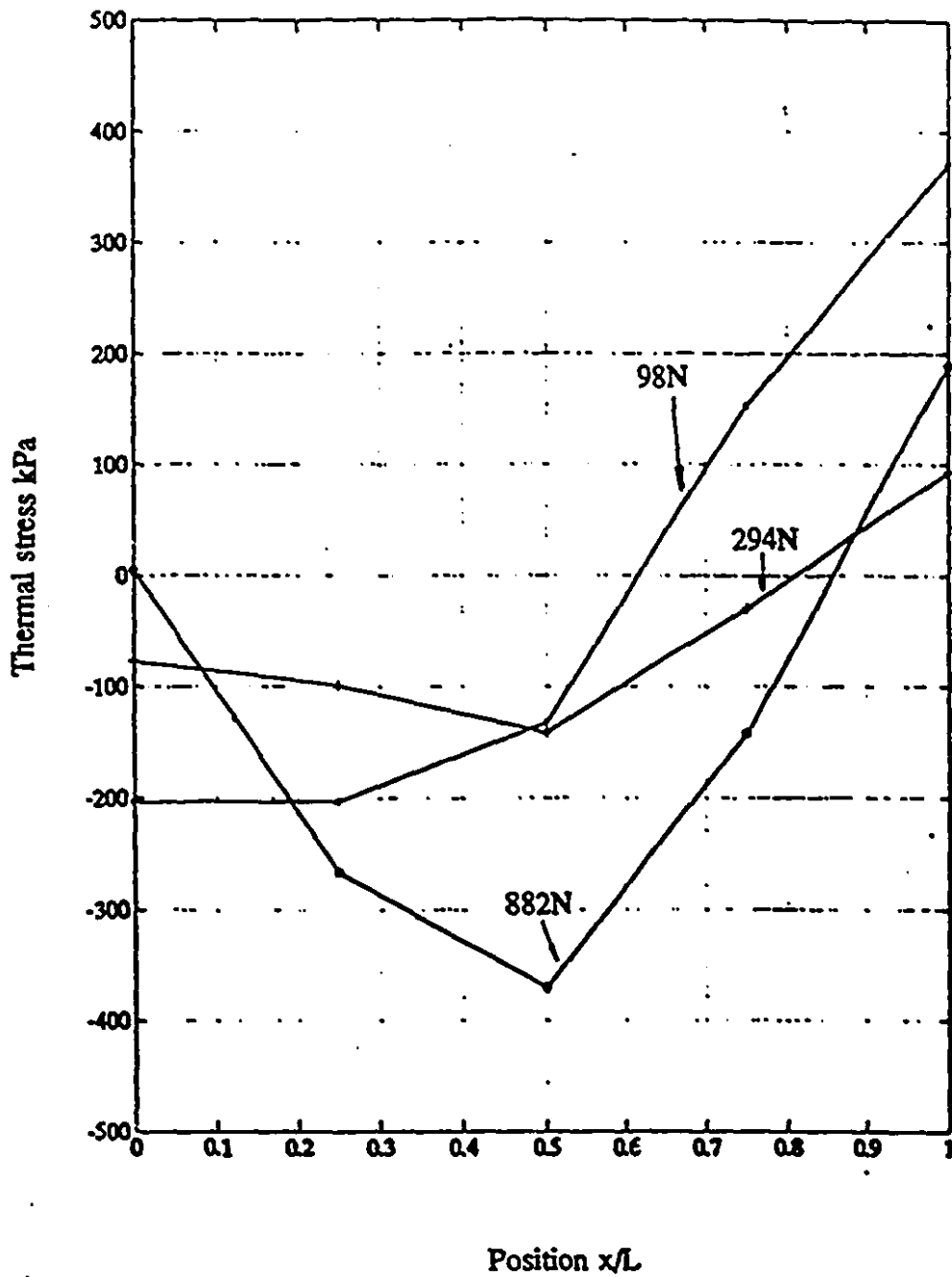


Fig. 5.12 Thermal stress distribution along the half-length interface from the axis of symmetry for $h/l=0.5$.

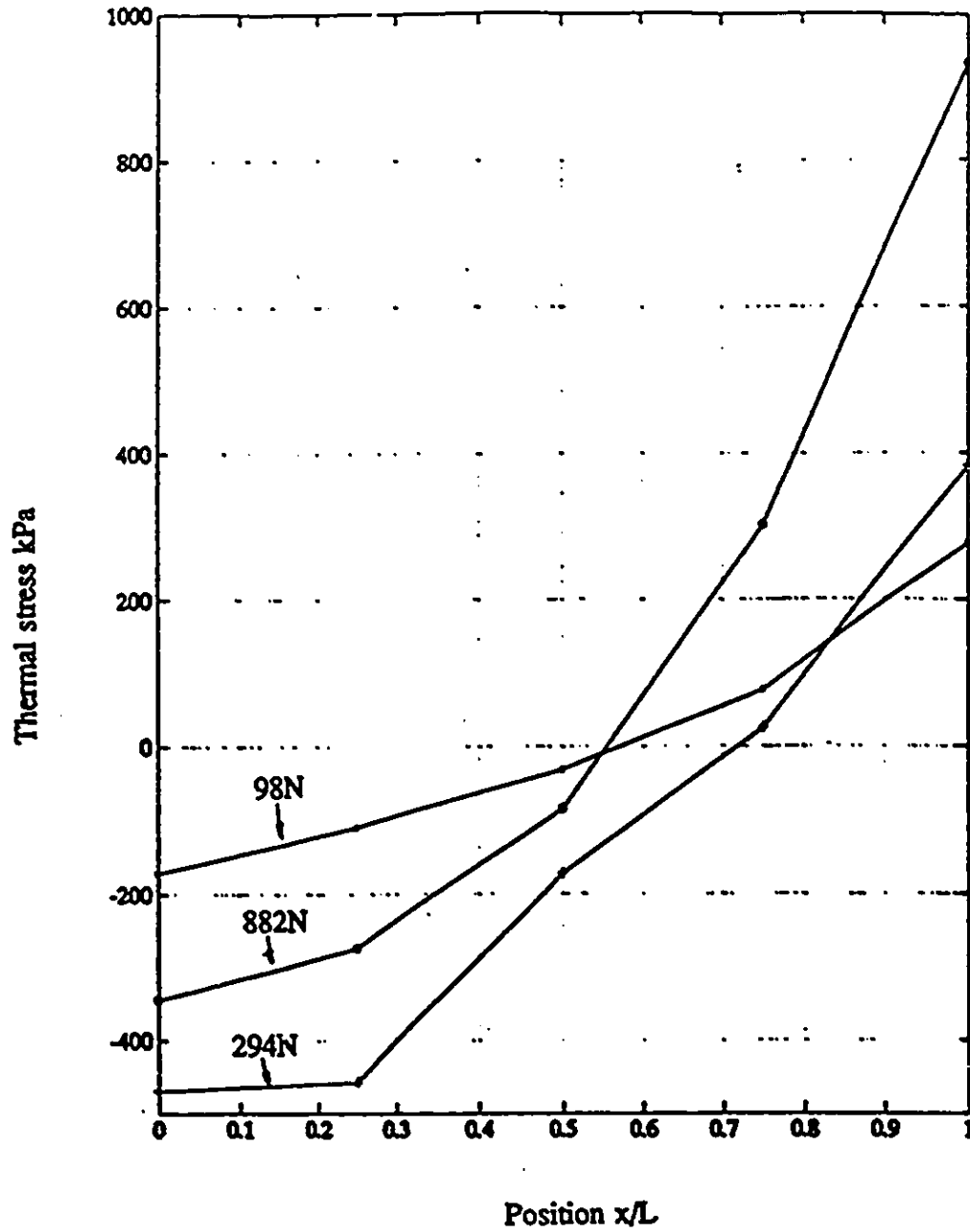


Fig. 5.13 Thermal stress distribution along the half-length interface from the axis of symmetry for $h/l=2.0$.

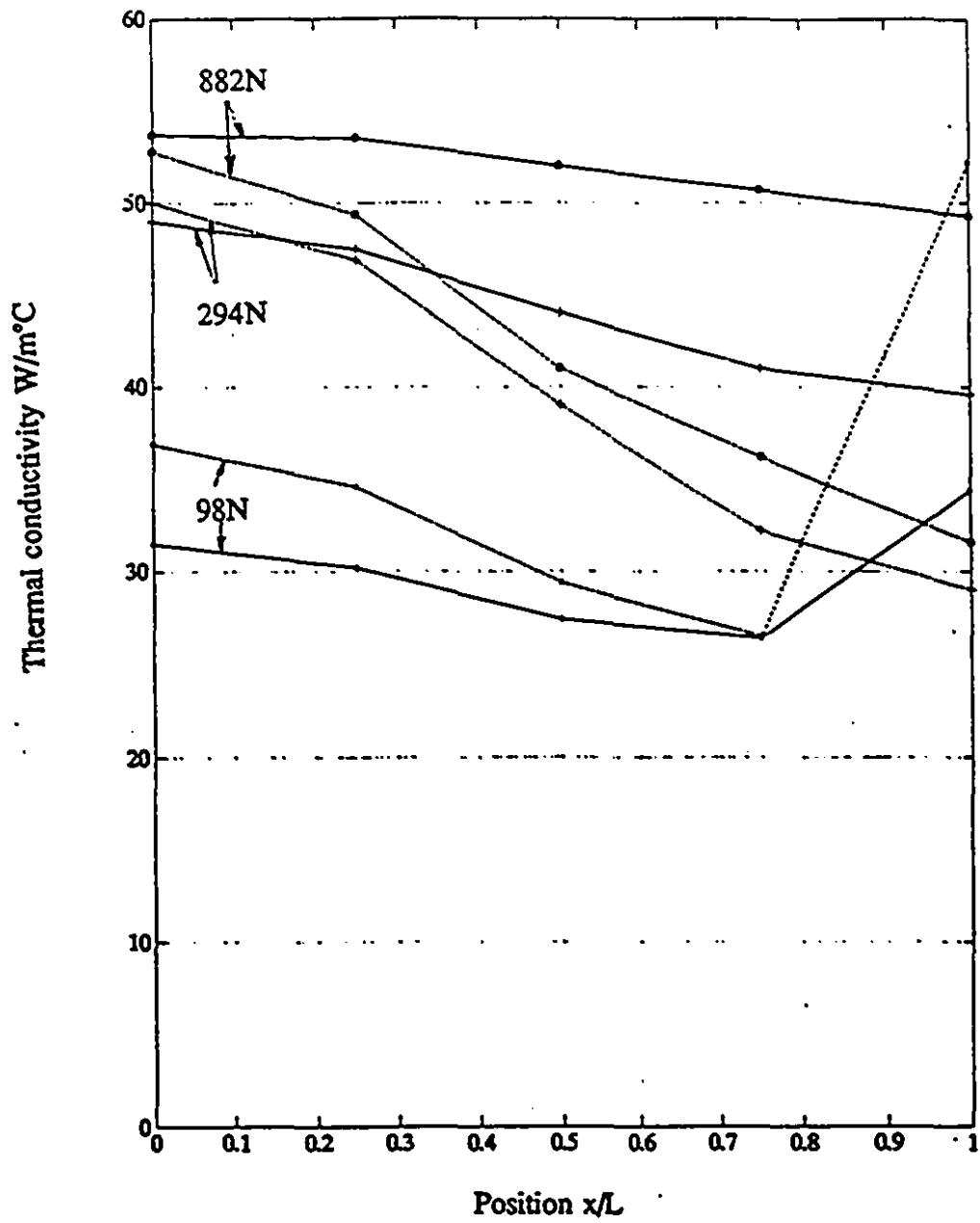


Fig. 5.14 Thermal conductivity distribution in the disturbed zone for $h/l=0.5$:
 — final thermal conductivity
 - - - first assumed thermal conductivity

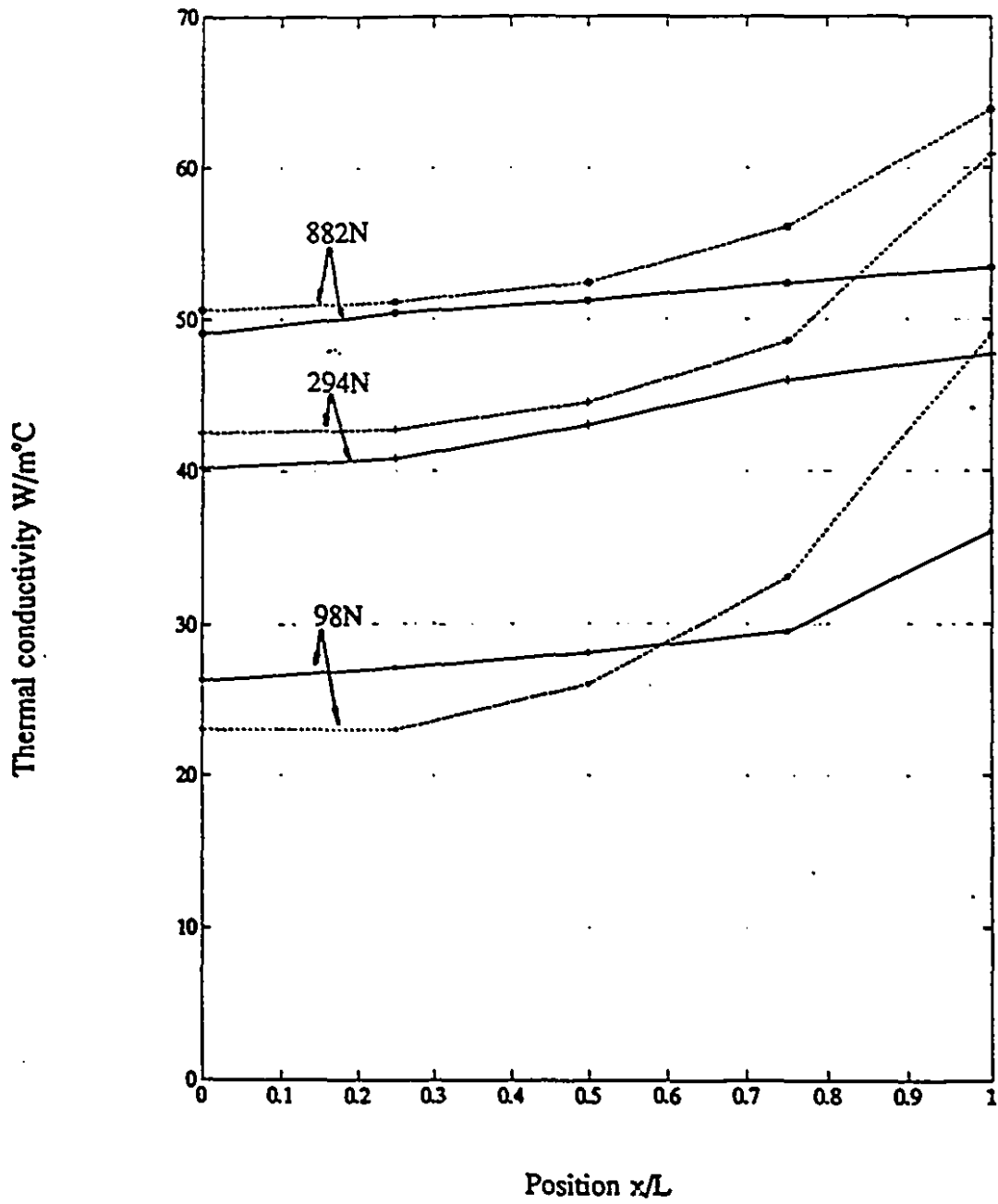


Fig. 5.15 Thermal conductivity distribution in the disturbed zone for $h/l=2.0$:
 — final thermal conductivity
 first assumed thermal conductivity

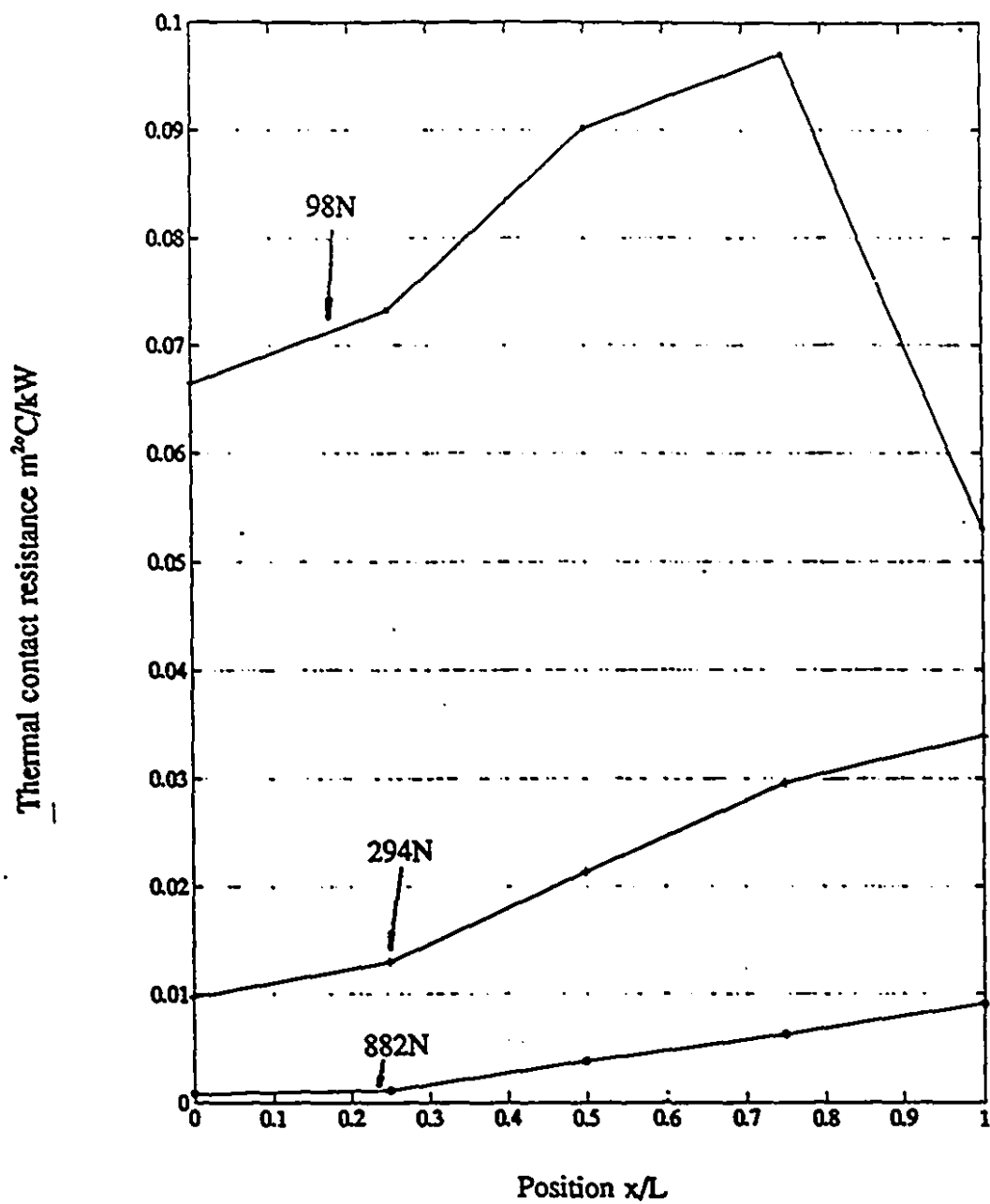


Fig. 5.16 Thermal contact resistance distribution along the half-length interface from the axis of symmetry for $h/l=0.5$.

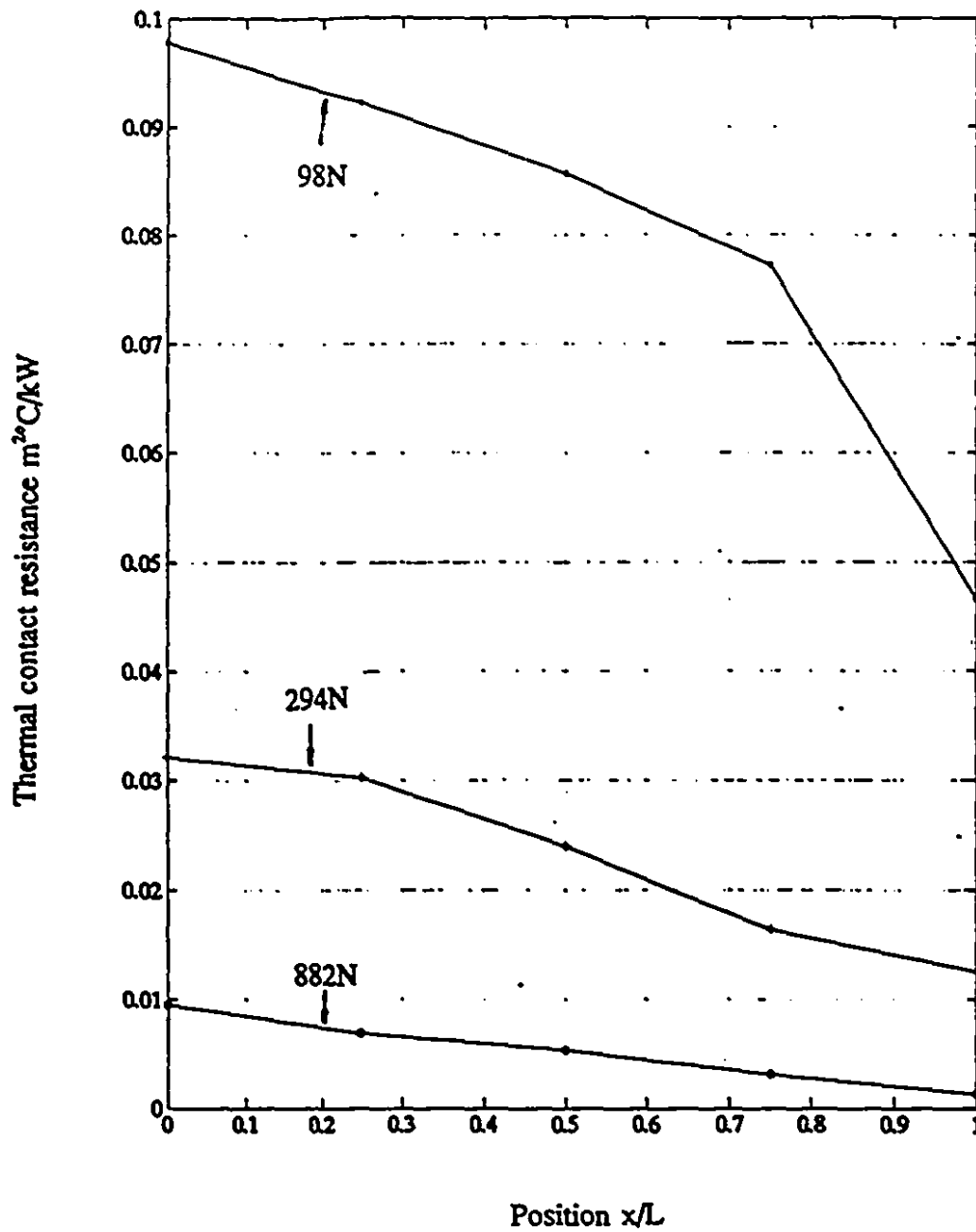


Fig. 5.17 Thermal contact resistance distribution along the half-length interface from the axis of symmetry for $h/l=2.0$.

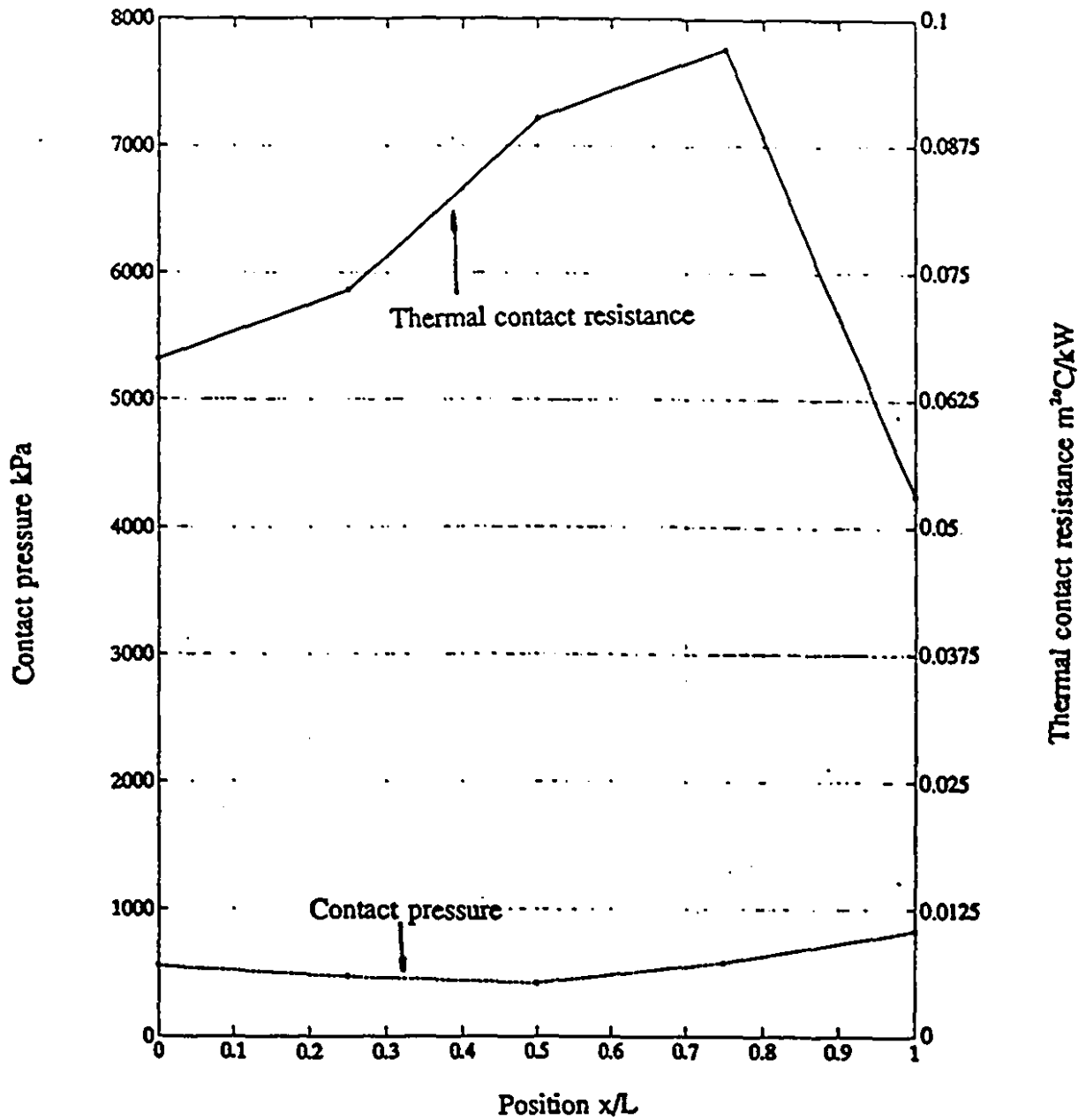


Fig. 5.18 Thermal contact resistance and contact pressure distribution for $h/l=0.5$ $F=98N$.

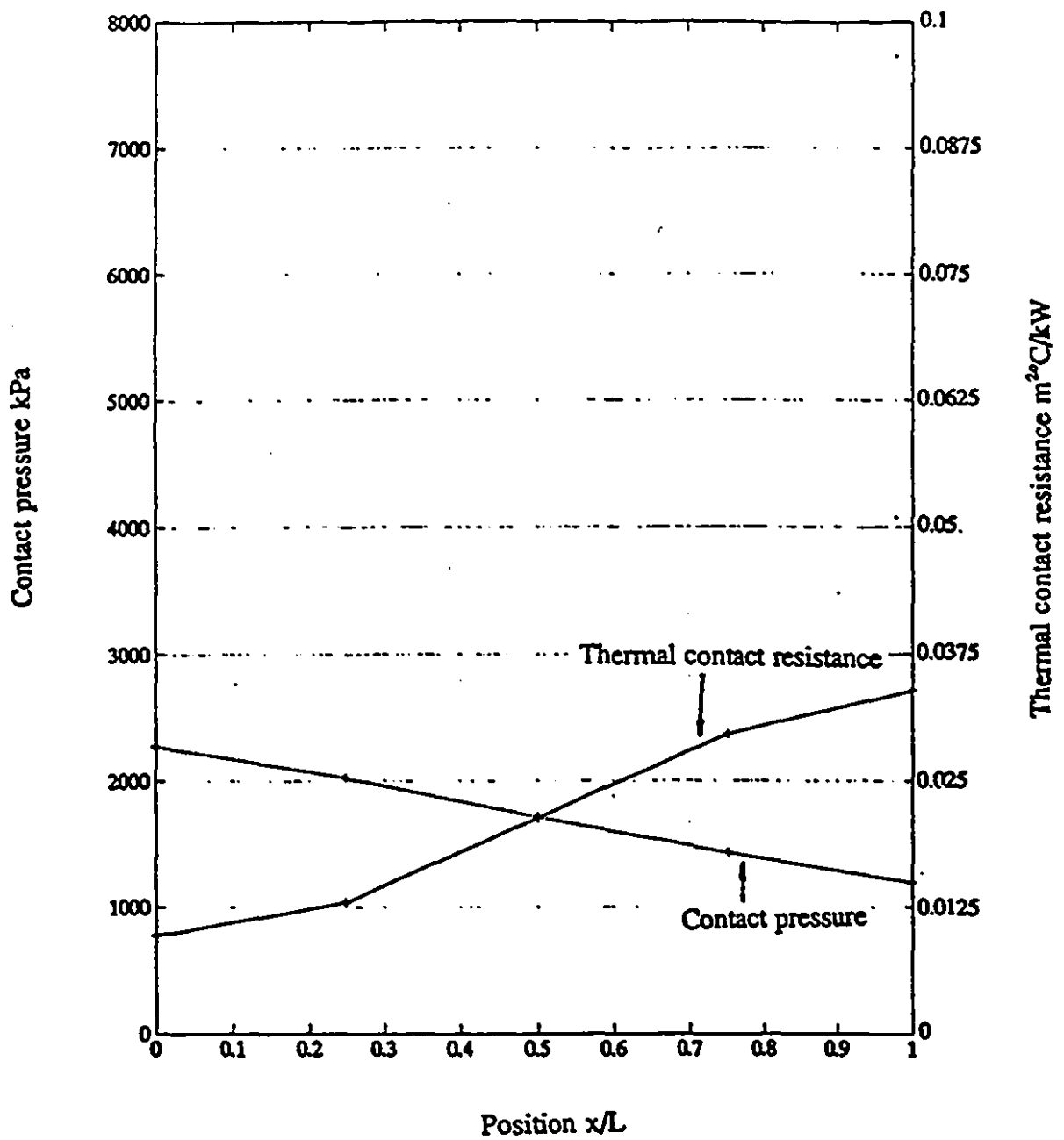


Fig. 5.19 Thermal contact resistance and contact pressure distribution for $h/l=0.5$ $F=294N$.

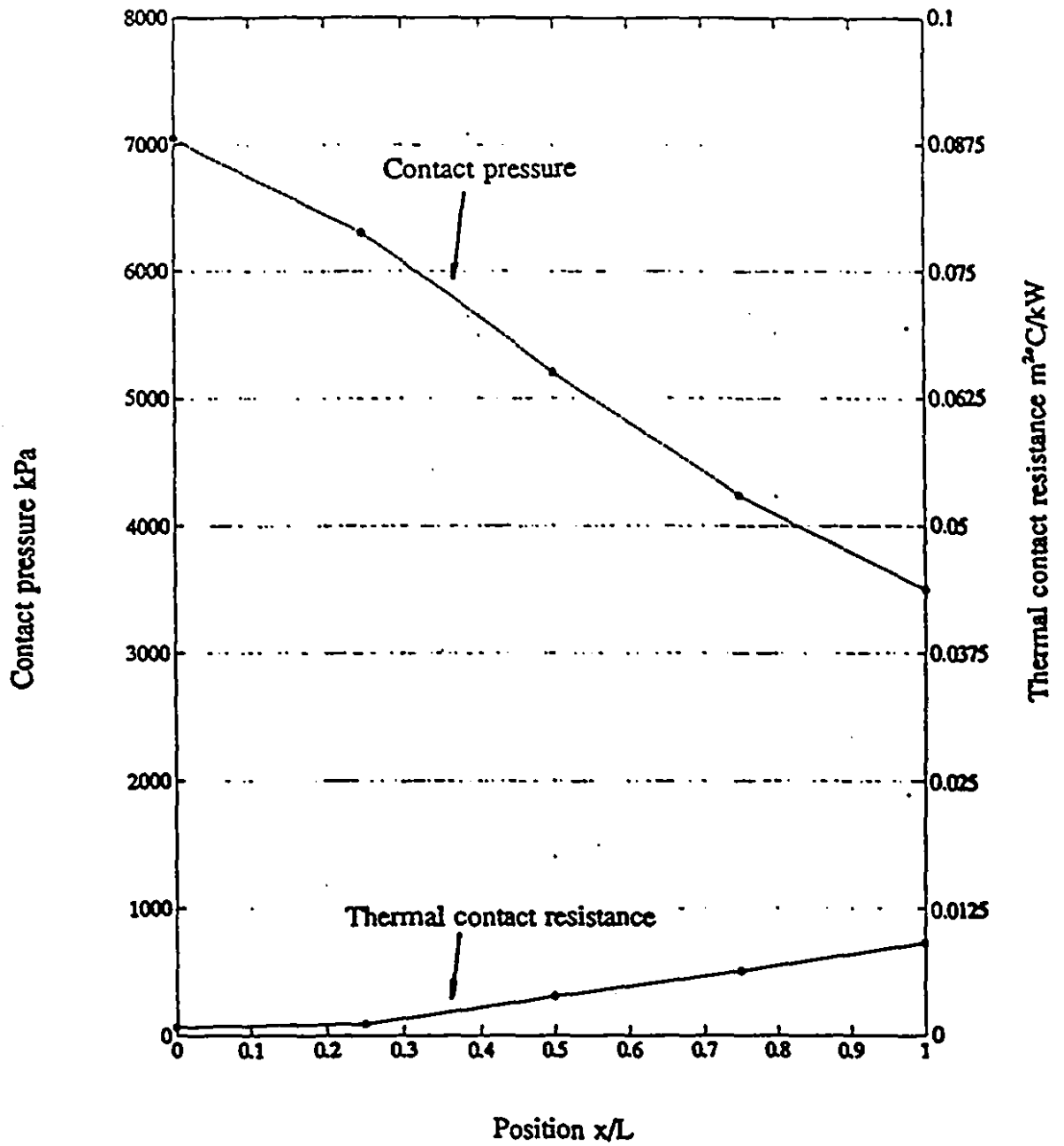


Fig. 5.20 Thermal contact resistance and contact pressure distribution for $h/l=0.5$ $F=882N$.

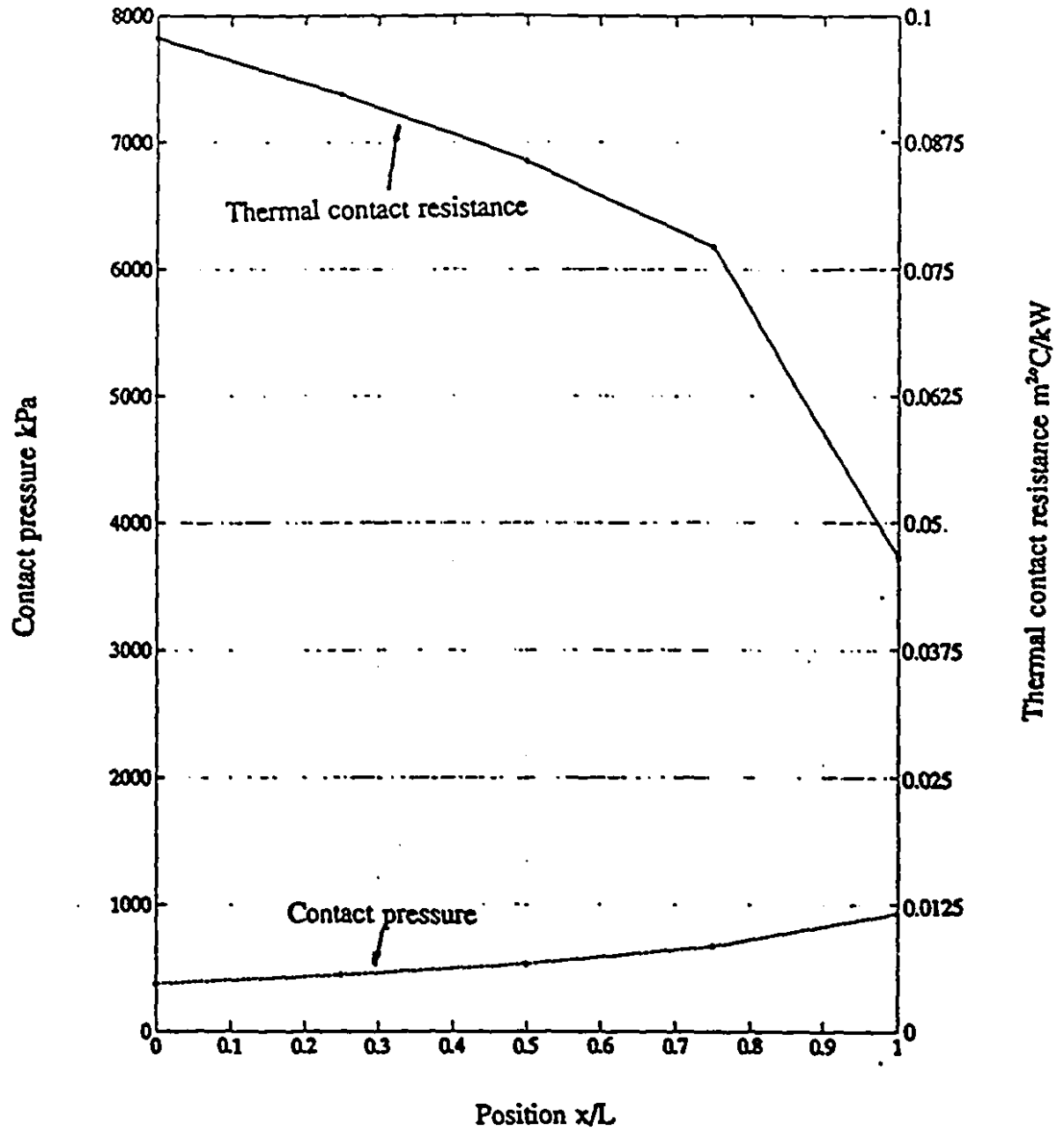


Fig. 5.21 Thermal contact resistance and contact pressure distribution for $h/l=2.0$ $F=98N$.

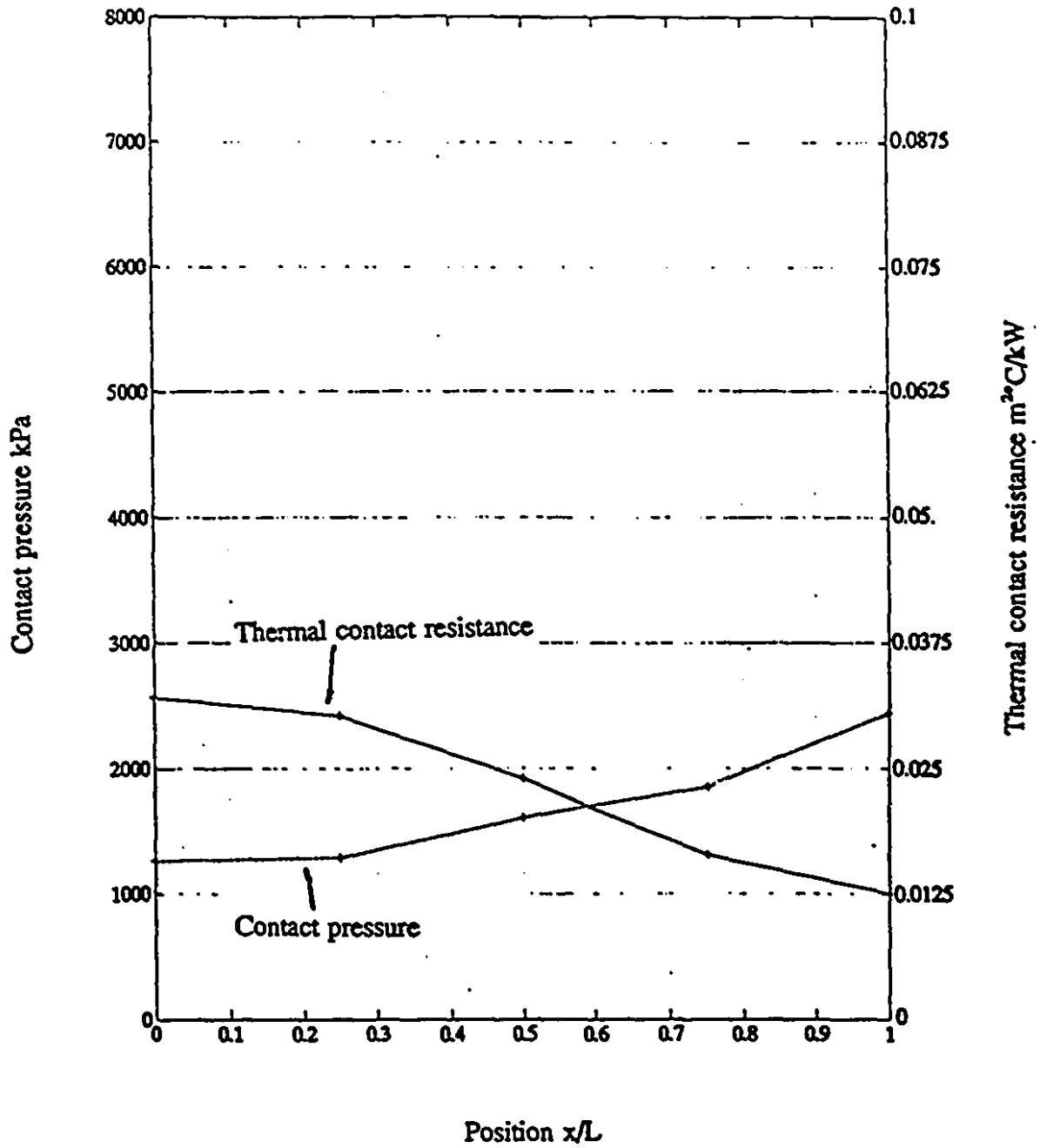


Fig. 5.22 Thermal contact resistance and contact pressure distribution for $h/l=2.0$ $F=294N$.

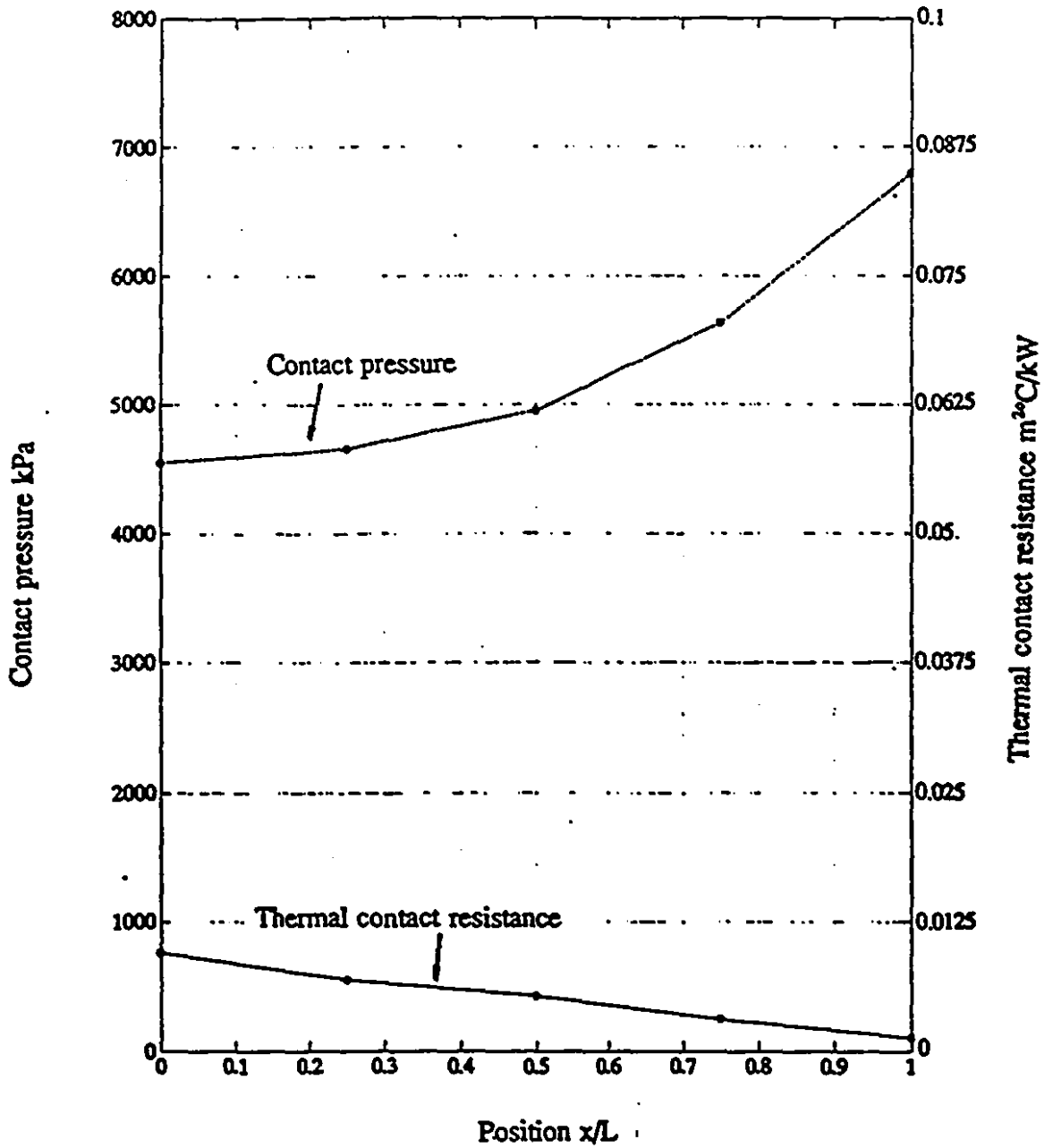


Fig. 5.23 Thermal contact resistance and contact pressure distribution for $h/l=2.0$ $F=882N$.

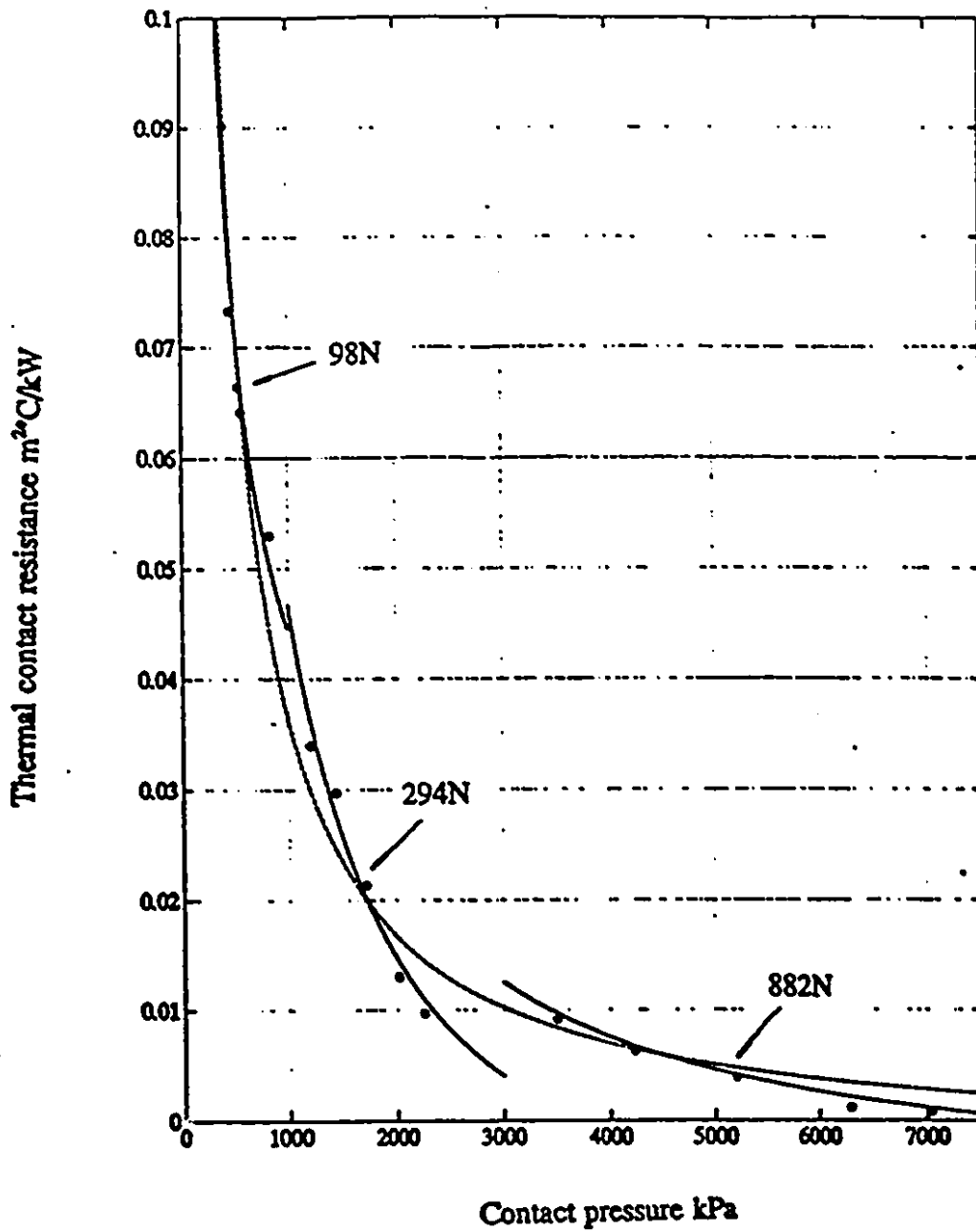


Fig. 5.24 Relationship between the thermal contact resistance and the contact pressure for the convex contact pressure distributions, $h/l=0.5$:
 — relationship for each load
 - - - general function for convex $p_c(x)$

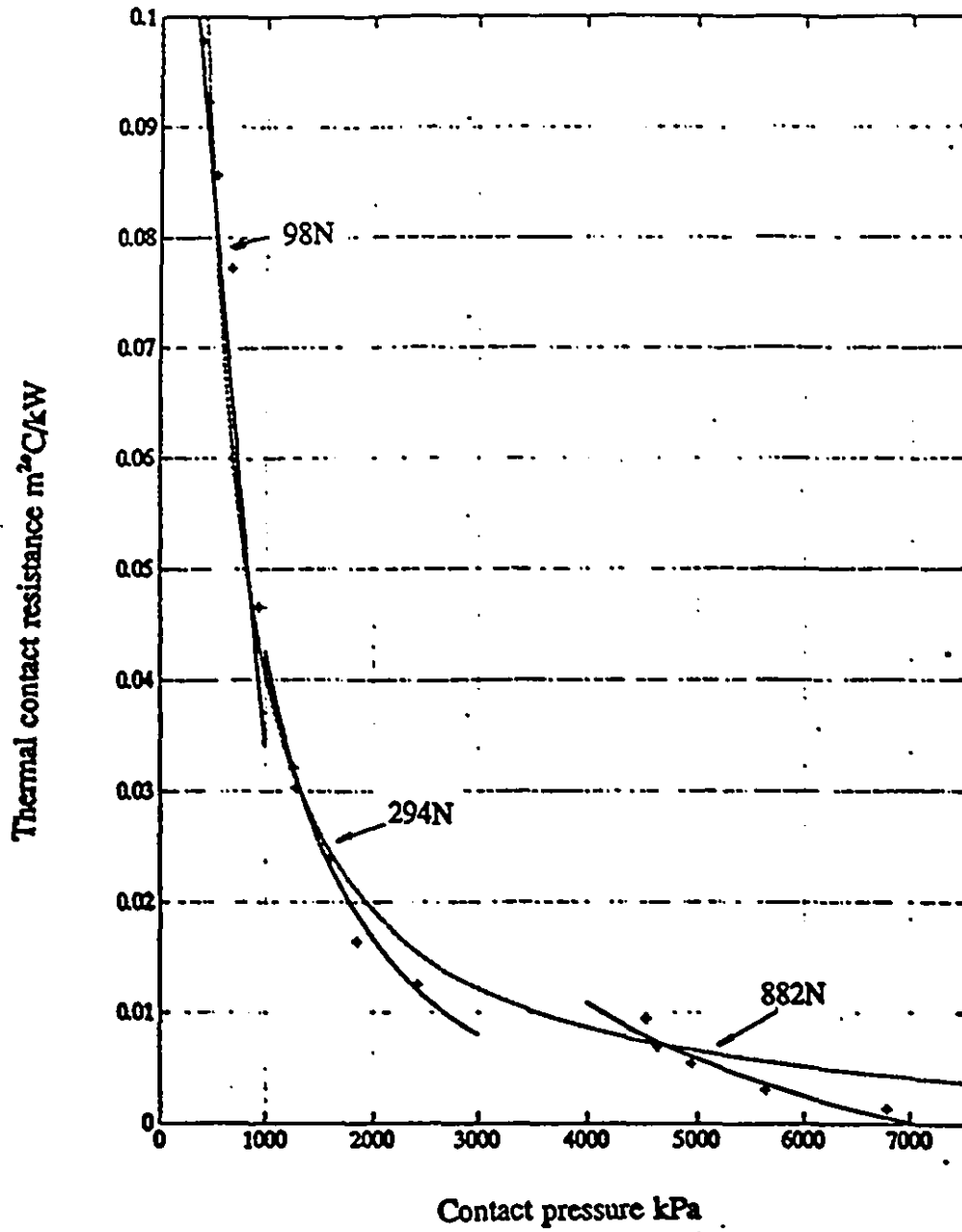


Fig. 5.25 Relationship between the thermal contact resistance and the contact pressure for concave contact pressure distributions, $h/l=2.0$:
 — relationship for each load
 - - - general function for concave $p_c(x)$

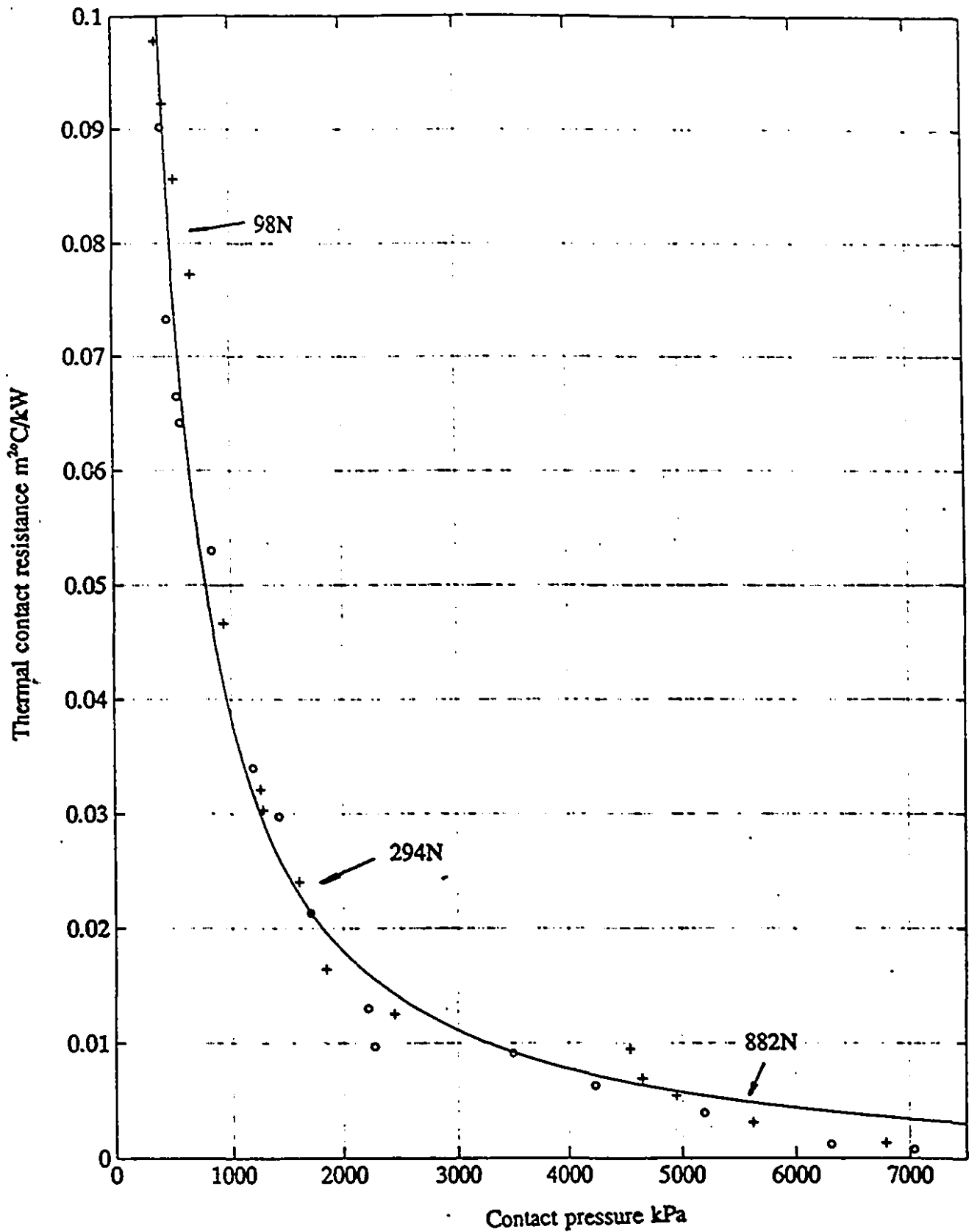


Fig. 5.26 General relationship between the thermal contact resistance and the contact pressure for convex and concave pressure distributions ($h/l=0.5$ and 2.0 respectively):

- o $h/l=0.5$
- + $h/l=2.0$

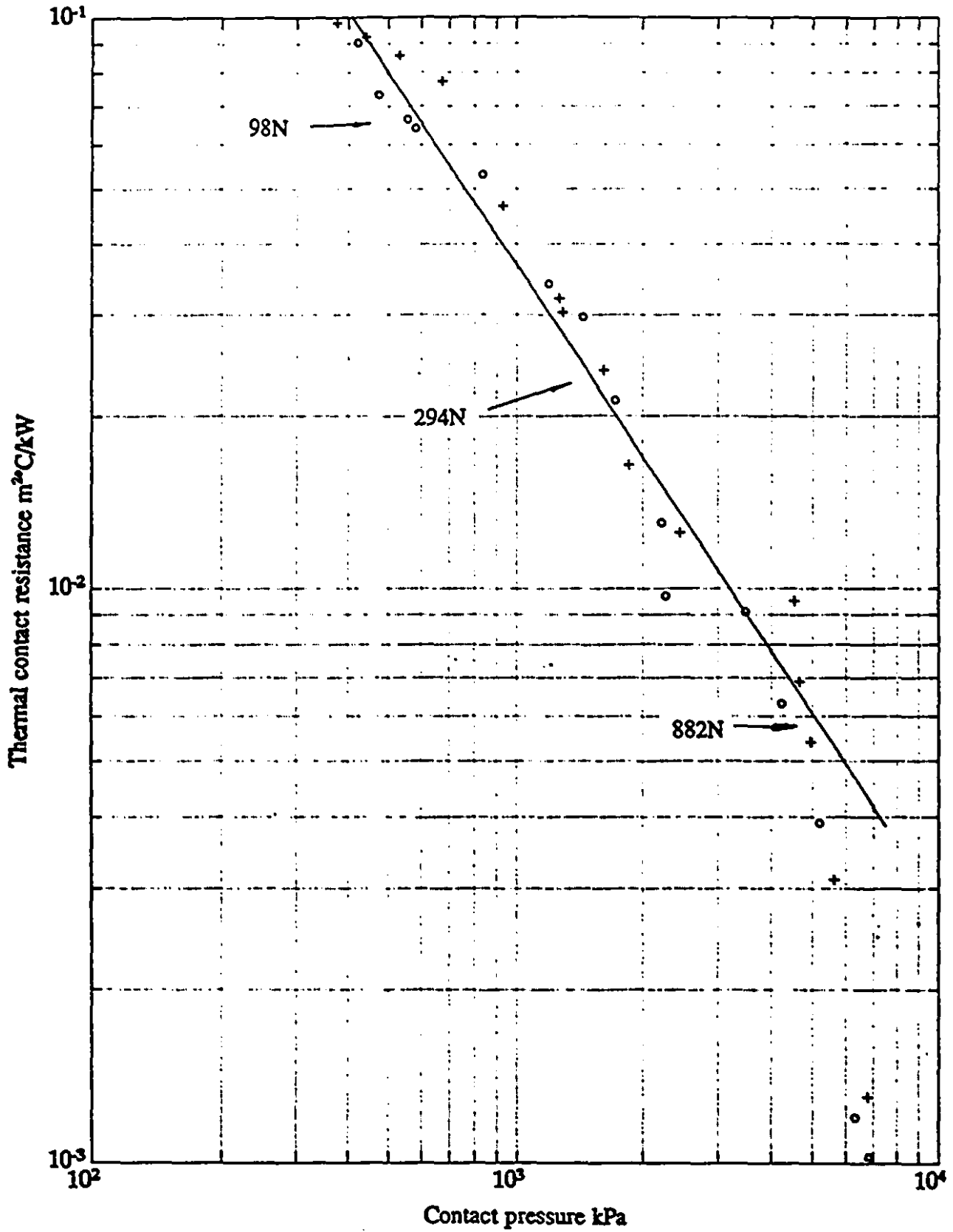


Fig. 5.27 General relationship function in log-log coordinates:
 ○ h/l=0.5
 + h/l=2.0

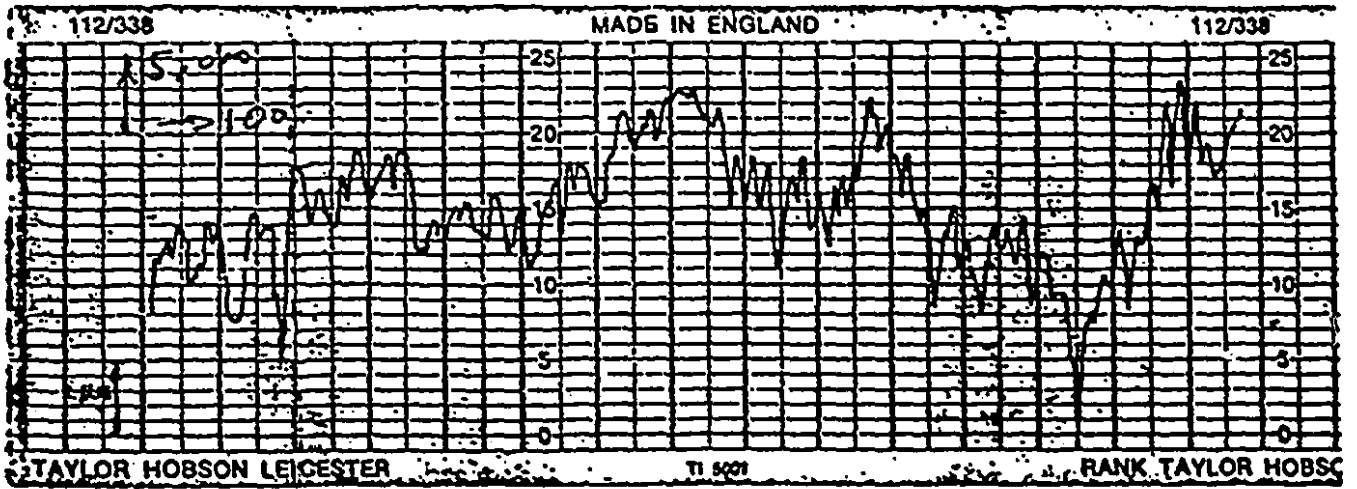


Fig. 5.28 Profile of the contact surface.

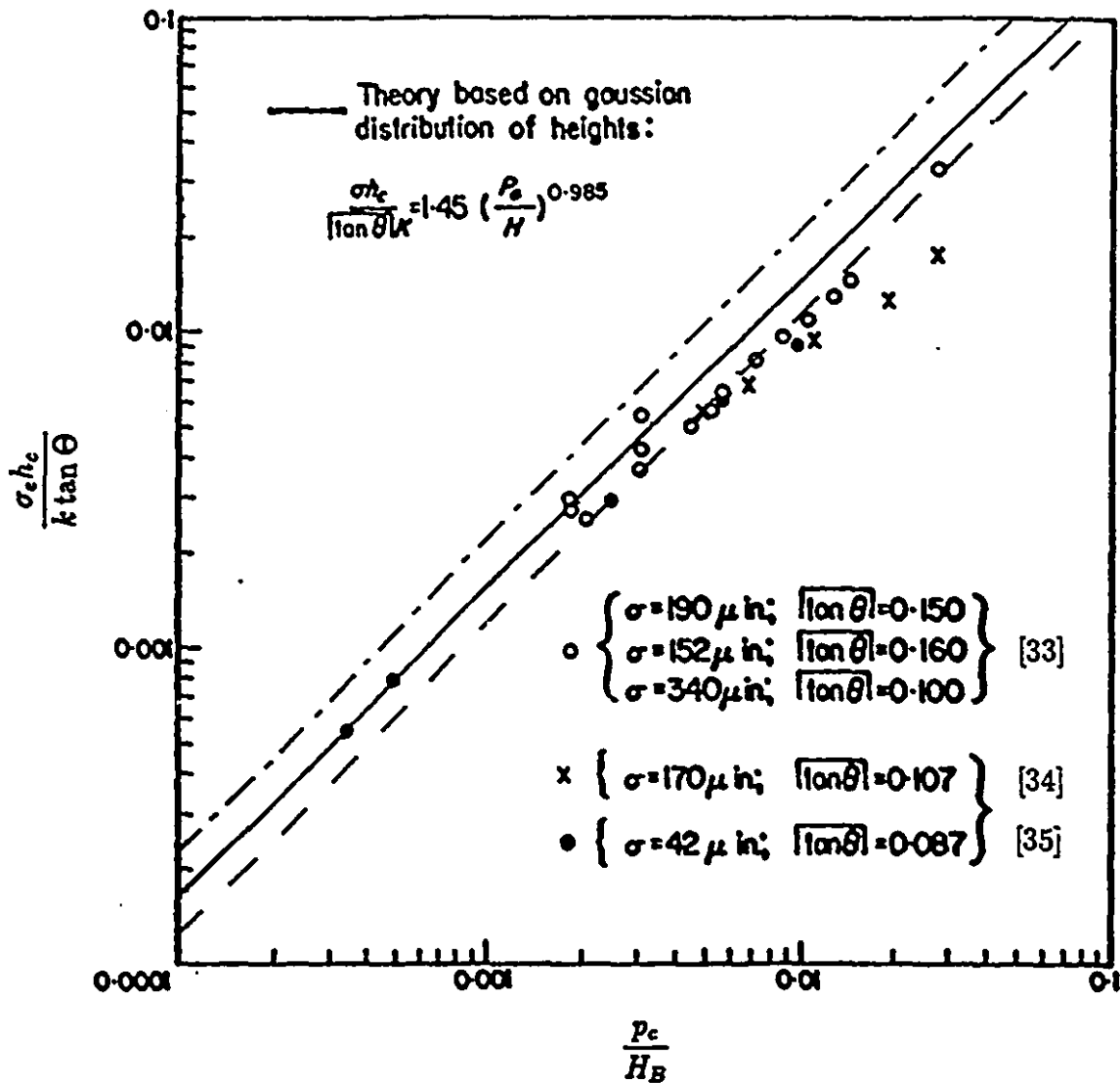


Fig. 5.29 Graph of thermal contact conductance vs. contact pressure in [19] with added general functions obtained in this study for

$$\begin{array}{ll} \text{---} & \sigma_e = 0.66, \quad \tan \theta = 0.14; \quad \frac{\sigma_e h_c}{k \tan \theta} = 1.22 \frac{P_c}{H_B} \\ \text{---} & \sigma_e = 1.20, \quad \tan \theta = 0.14; \quad \frac{\sigma_e h_c}{k \tan \theta} = 2.13 \frac{P_c}{H_B} \end{array}$$

Appendix B

Tables

Table 3.1: Calibration results of the thermocouples (TC) on upper specimen
 $h/l=0.5$; T, °C

Tref	7.9	40.9	59.9	88.7	Tref	7.9	40.9	59.9	88.7
TC#					TC#				
1	7.9	40.9	59.8	88.6	15	7.9	40.8	59.8	88.7
2	7.9	40.9	59.9	88.7	16	7.9	40.8	59.9	88.6
3	8.0	40.8	59.8	88.7	17	8.0	40.9	59.9	88.6
4	7.9	40.9	59.9	88.6	18	7.9	40.9	59.8	88.7
5	8.0	40.8	59.9	88.6	19	7.9	40.9	59.9	88.6
6	8.1	40.9	59.8	88.7	20	7.9	40.8	59.9	88.7
7	8.0	40.8	59.9	88.6	21	8.0	40.8	59.8	88.8
8	8.1	40.9	59.8	88.7	22	8.0	40.9	59.8	88.6
9	8.0	40.8	59.9	88.6	23	7.9	40.9	59.8	88.7
10	8.0	40.9	59.8	88.7	24	8.0	40.9	59.9	88.6
11	7.9	40.9	59.9	88.7	25	7.9	40.8	59.9	88.7
12	7.9	40.9	59.8	88.6	26	8.1	40.9	59.9	88.7
13	8.0	40.9	59.8	88.6	27	7.9	40.9	59.8	88.7
14	7.9	40.8	59.8	88.7					

Table 3.2: Calibration results of the thermocouples (TC) on upper specimen
 $h/l=2.0$; T, °C

Tref TC#	7.9	40.9	59.9	88.7	Tref TC#	7.9	40.9	59.9	88.7
1	7.9	40.9	59.8	88.7	18	7.9	40.9	59.9	88.7
2	7.8	40.8	59.9	88.7	19	7.9	41.0	59.8	88.7
3	7.9	40.9	59.9	88.8	20	8.0	40.9	59.9	88.7
4	7.9	40.9	59.8	88.6	21	8.0	41.0	60.0	88.7
5	7.9	41.0	60.0	88.7	22	8.0	41.0	60.0	88.6
6	8.0	40.9	60.0	88.8	23	7.9	40.9	60.0	88.6
7	8.0	40.8	59.9	88.8	24	8.0	40.9	59.9	88.8
8	7.9	40.9	59.9	88.6	25	7.9	41.0	59.9	88.8
9	8.0	41.0	59.8	88.7	26	7.9	41.0	59.8	88.7
10	8.0	41.0	60.0	88.7	27	7.9	41.0	59.8	88.8
11	7.9	40.9	60.0	88.7	28	7.9	41.0	59.9	88.7
12	7.9	40.9	59.8	88.6	29	8.0	40.9	60.0	88.6
13	7.9	40.9	59.8	88.6	30	7.9	40.9	59.9	88.6
14	8.0	40.9	59.9	88.8	31	8.0	40.9	59.8	88.7
15	8.0	40.8	59.9	88.7	32	8.0	41.0	60.0	88.7
16	8.0	40.9	59.8	88.8	33	8.0	41.0	60.0	88.8
17	8.0	40.9	59.9	88.8					

Table 3.3: Calibration results of the thermocouples (TC) on lower specimen; T, °C

Tref TC#	7.9	40.9	59.9	88.7	Tref TC#	7.9	40.9	59.9	88.7
1	7.9	40.9	59.9	88.8	22	7.9	41.0	59.9	88.6
2	7.9	40.8	59.9	88.8	23	7.9	41.0	59.9	88.6
3	8.0	41.0	59.9	88.7	24	7.9	41.0	59.9	88.7
4	8.0	40.9	59.8	88.7	25	7.9	41.0	60.0	88.8
5	8.0	40.9	59.8	88.6	26	7.8	40.9	60.0	88.7
6	8.0	41.0	60.0	88.8	27	7.9	40.9	60.0	88.6
7	8.0	41.0	60.0	88.6	28	7.8	40.9	59.9	88.7
8	7.8	41.0	60.0	88.7	29	7.8	40.9	60.0	88.8
9	7/9	40.8	59.9	88.7	30	7.8	40.9	60.0	88.8
10	7.9	40.9	59.9	88.8	31	7.9	40.9	59.9	88.7
11	7.8	40.9	59.8	88.8	32	8.0	40.8	60.0	88.6
12	8.0	40.8	59.9	88.7	33	8.0	40.8	59.9	88.7
13	8.0	40.9	60.0	88.7	34	8.0	40.8	59.9	88.7
14	7.9	40.9	60.0	88.7	35	8.0	40.9	60.0	88.8
15	7.9	40.9	60.0	88.6	36	8.0	40.9	59.8	88.8
16	7.9	41.0	59.8	88.6	37	7.9	40.9	59.9	88.6
17	7.9	41.0	59.8	88.7	38	7.9	40.9	59.9	88.7
18	7.8	41.0	59.9	88.8	39	8.0	41.0	60.0	88.6
19	7.8	40.9	59.9	88.8					
20	8.0	40.9	59.9	88.6					
21	8.0	40.9	60.0	88.8					

Table 5.1: Experimental temperature data on the upper specimen,
 $h/l=0.5$, $F=98N$; T , °C

Round TC#	1	2	3	Ave.	Round TC#	1	2	3	Ave.
1	59.2	59.2	59.1	59.2	15	63.6	63.6	63.5	63.6
2	59.7	59.7	59.7	59.7	16	63.6	63.5	63.5	63.5
3	59.9	59.9	60.0	59.9	17	63.6	63.6	63.6	63.6
4	59.9	59.9	59.9	59.9	18	63.5	63.4	63.4	63.4
5	59.8	59.7	59.8	59.8	19	67.6	67.6	67.6	67.6
6	59.8	59.7	59.8	58.8	20	67.7	67.6	67.7	67.7
7	59.8	59.8	59.8	59.8	21	67.6	67.5	67.6	67.6
8	59.8	59.8	59.7	59.8	22	67.2	67.2	67.1	67.2
9	59.3	59.2	59.3	59.3	23	67.0	67.0	67.0	67.0
10	63.5	63.4	63.5	63.5	24	67.2	67.1	67.2	67.2
11	63.5	63.5	63.5	63.5	25	67.5	67.5	67.6	67.5
12	63.5	63.5	63.4	63.5	26	67.6	67.7	67.6	67.6
13	63.6	63.5	63.5	63.5	27	67.6	67.5	67.6	67.6
14	63.6	63.4	63.6	63.5					

Table 5.2: Experimental temperature data on the lower specimen,
 $h/l=0.5$, $F=98N$; T , °C

Round TC#	1	2	3	Ave.	Round TC#	1	2	3	Ave.
1	51.3	51.3	51.2	51.3	21	44.3	44.2	44.2	44.2
2	52.2	52.1	52.2	52.2	22	43.1	43.1	43.1	43.1
3	52.8	52.8	52.8	52.8	23	41.8	41.9	41.8	41.8
4	53.2	53.1	53.1	53.1	24	39.1	39.0	39.0	39.0
5	53.4	53.4	53.3	53.4	25	35.4	35.4	35.4	35.4
6	53.2	53.2	53.2	53.2	26	35.6	35.6	35.6	35.6
7	52.8	52.9	52.9	52.9	27	36.6	36.7	36.7	36.7
8	52.1	52.0	52.2	52.1	28	36.5	36.5	36.5	36.5
9	51.4	51.4	51.4	51.4	29	36.4	36.3	36.3	36.3
10	48.7	48.7	48.7	48.7	30	36.5	36.5	36.4	36.5
11	49.4	49.5	49.5	49.5	31	36.6	36.6	36.6	36.6
12	49.9	50.0	49.9	49.9	32	35.6	35.4	35.6	35.6
13	50.1	50.1	50.1	50.1	33	35.4	35.4	35.3	35.4
14	50.2	50.3	50.3	50.3	34	39.1	39.0	39.2	39.1
15	50.0	50.1	50.2	50.1	35	41.8	41.8	41.8	41.8
16	49.9	49.9	49.9	49.9	36	43.1	43.0	43.2	43.1
17	49.4	49.3	49.4	49.4	37	44.3	44.3	44.3	44.3
18	48.7	48.7	48.7	48.7	38	48.4	48.4	48.4	48.4
19	50.2	50.1	50.1	50.1	39	50.2	50.1	50.1	50.1
20	48.4	48.5	48.5	48.5					

Table 5.3: Experimental temperature data on the upper specimen,
 $h/l=0.5$, $F=294N$; T , °C

Round TC#	1	2	3	Ave.	Round TC#	1	2	3	Ave.
1	58.7	58.7	58.7	58.7	15	63.3	63.3	63.2	63.3
2	59.1	59.1	59.0	59.1	16	63.2	63.1	63.2	63.2
3	59.3	59.3	59.3	59.3	17	63.2	63.1	63.2	63.2
4	59.4	59.5	59.4	59.4	18	63.2	63.1	63.1	63.1
5	59.5	59.6	59.5	59.5	19	67.5	67.5	67.6	67.5
6	59.4	59.4	59.4	59.4	20	67.6	67.6	67.6	67.6
7	59.2	59.2	59.2	59.2	21	67.4	67.4	67.4	67.4
8	59.1	59.1	59.1	59.1	22	67.1	67.0	67.1	67.1
9	58.8	58.7	58.8	58.8	23	66.9	66.9	66.8	66.9
10	63.2	63.1	63.1	63.1	24	67.1	67.0	67.0	67.0
11	63.2	63.2	63.2	63.2	25	67.4	67.2	67.4	67.4
12	63.3	63.1	63.2	63.2	26	67.6	67.5	67.7	67.6
13	63.3	63.3	63.2	63.3	27	67.5	67.5	67.5	67.5
14	63.3	63.3	63.3	63.3					

Table 5.4: Experimental temperature data on the lower specimen,
 $h/l=0.5$, $F=294N$; T , °C

Round TC#	1	2	3	Ave.	Round TC#	1	2	3	Ave.
1	52.1	52.1	52.0	52.1	21	44.9	44.9	44.8	44.9
2	53.2	53.3	53.2	53.2	22	43.6	43.6	43.5	43.6
3	53.8	53.8	53.9	53.8	23	42.3	42.3	42.1	42.3
4	54.2	54.1	54.2	53.2	24	39.6	39.5	39.6	39.6
5	54.4	54.4	54.4	54.4	25	35.8	35.7	35.8	35.8
6	54.2	54.1	54.2	54.2	26	36.0	36.0	36.0	36.0
7	53.8	53.8	53.8	53.8	27	37.1	37.1	37.2	37.2
8	53.1	53.1	53.1	53.1	28	36.9	36.9	36.9	36.9
9	52.0	52.0	51.9	52.0	29	36.8	36.9	36.8	36.9
10	49.4	49.3	49.4	49.4	30	37.0	37.0	37.1	37.0
11	50.2	50.2	50.2	50.2	31	37.2	37.1	37.2	37.2
12	50.7	50.6	50.8	50.7	32	36.0	36.1	36.1	36.1
13	50.9	50.9	50.9	50.9	33	35.8	35.8	35.8	35.8
14	51.0	51.0	51.0	51.0	34	39.6	39.7	39.7	39.7
15	50.9	51.0	50.9	50.9	35	42.3	42.3	42.3	42.3
16	50.7	50.7	50.7	50.7	36	43.6	43.6	43.6	43.6
17	50.2	50.4	50.2	50.2	37	44.9	44.9	44.8	44.9
18	49.3	49.3	49.3	49.3	38	48.9	48.9	48.9	48.9
19	51.5	51.5	51.4	51.5	39	51.4	51.4	51.4	51.4
20	48.9	48.9	49.0	48.9					

Table 5.5: Experimental temperature data on the upper specimen,
 $h/l=0.5$, $F=882N$; T , °C

Round TC#	1	2	3	Ave.	Round TC#	1	2	3	Ave.
1	59.1	59.1	59.0	59.1	15	63.3	63.3	63.2	63.3
2	59.3	59.3	59.3	59.3	16	63.4	63.4	63.4	63.4
3	59.5	59.5	59.4	59.5	17	63.4	63.3	63.2	63.3
4	59.5	59.5	59.5	59.5	18	63.4	63.3	63.3	63.3
5	59.4	59.3	59.3	59.4	19	67.5	67.5	67.6	67.5
6	59.4	59.4	59.4	59.4	20	67.6	67.5	67.6	67.6
7	59.5	59.5	59.4	59.5	21	67.5	67.5	67.5	67.5
8	59.4	59.3	59.4	59.4	22	67.2	67.2	67.1	67.2
9	59.2	59.2	59.2	59.2	23	66.9	66.8	66.9	66.9
10	63.4	63.4	63.3	63.3	24	67.2	67.1	67.2	67.2
11	63.4	63.4	63.4	63.4	25	67.5	67.6	67.6	67.6
12	63.4	63.4	63.3	63.4	26	67.6	67.5	67.5	67.5
13	63.4	63.3	63.3	63.3	27	67.5	67.4	67.4	67.4
14	63.4	63.4	63.4	63.4					

Table 5.6: Experimental temperature data on the lower specimen,
 $h/l=0.5$, $F=882\text{N}$; T , $^{\circ}\text{C}$

Round TC#	1	2	3	Ave.	Round TC#	1	2	3	Ave.
1	52.8	52.7	52.8	52.8	21	45.5	45.6	45.7	45.6
2	53.9	53.9	53.9	53.9	22	44.2	44.2	44.1	44.1
3	54.4	54.5	54.4	54.4	23	42.8	42.7	42.7	42.7
4	54.8	54.8	54.8	54.8	24	40.0	40.0	40.0	40.0
5	54.9	54.9	54.9	54.9	25	36.2	36.1	36.1	36.1
6	54.8	54.8	54.8	54.8	26	36.4	36.3	36.4	36.4
7	54.4	54.3	54.4	54.4	27	37.4	37.4	37.4	37.4
8	53.9	53.8	53.9	53.9	28	37.3	37.2	37.2	37.2
9	52.8	52.8	52.8	52.8	29	37.2	37.2	27.1	37.2
10	49.9	49.9	49.9	49.9	30	37.3	37.3	47.4	37.3
11	50.6	50.4	50.5	50.5	31	37.4	37.5	37.4	37.4
12	51.1	51.1	51.2	51.1	32	36.4	36.4	36.5	36.4
13	51.4	51.4	51.3	51.4	33	36.2	36.2	36.2	36.2
14	51.5	51.5	51.3	51.5	34	40.0	40.0	39.9	40.0
15	51.4	51.3	51.4	51.4	35	42.8	42.8	42.7	42.8
16	51.1	51.0	51.0	51.0	36	44.3	44.4	44.4	44.4
17	50.5	50.5	50.5	50.5	37	45.6	45.4	45.5	45.5
18	49.8	49.8	50.0	49.8	38	49.7	49.8	49.8	49.8
19	51.9	52.0	51.9	51.9	39	51.9	51.8	51.9	51.9
20	49.7	49.8	49.7	49.7					

Table 5.7: Experimental temperature data on the upper specimen,
 $h/l=2.0$, $F=98N$; T , °C

Round TC#	1	2	3	Ave.	Round TC#	1	2	3	Ave.
1	42.0	42.0	42.0	42.0	18	44.4	44.4	44.3	44.4
2	42.3	42.3	42.2	42.2	19	48.9	48.8	48.9	48.9
3	42.6	42.6	42.6	42.6	20	55.5	55.5	55.4	55.5
4	42.7	42.7	42.6	42.7	21	62.0	62.0	62.0	62.0
5	42.8	42.8	42.7	42.8	22	68.8	68.6	68.7	68.7
6	42.7	42.7	42.7	42.7	23	68.8	68.8	68.7	68.8
7	42.7	42.6	42.7	42.7	24	68.7	68.7	68.6	68.7
8	42.3	42.3	42.3	42.3	25	68.4	68.5	68.5	68.5
9	42.0	41.9	42.0	42.0	26	68.2	68.1	68.2	68.2
10	44.5	44.5	44.5	44.5	27	68.4	68.5	68.4	69.4
11	44.5	44.4	44.4	44.4	28	68.7	68.8	68.7	68.7
12	44.6	44.5	44.6	44.6	29	68.8	68.8	68.8	68.8
13	44.7	44.7	44.7	44.7	30	68.8	68.7	68.6	68.7
14	44.7	44.8	44.8	44.8	31	62.0	62.0	62.1	62.0
15	44.6	44.7	44.8	44.7	32	55.4	55.4	55.4	55.4
16	44.6	44.6	44.6	44.6	33	48.8	48.8	48.8	48.8
17	44.5	44.5	44.5	44.5					

Table 5.8: Experimental temperature data on the lower specimen,
 $h/l=2.0$, $F=98N$; T , °C

Round TC#	1	2	3	Ave.	Round TC#	1	2	3	Ave.
1	37.6	37.6	37.7	37.6	21	33.7	33.6	33.5	33.6
2	38.1	38.0	38.1	38.1	22	32.9	32.7	32.8	32.8
3	38.3	38.3	38.3	38.3	23	32.2	32.1	32.1	32.1
4	38.5	38.5	38.5	38.5	24	30.7	30.8	30.8	30.8
5	38.5	38.5	38.4	38.5	25	28.7	28.7	28.9	28.7
6	38.4	38.5	38.4	38.4	26	28.8	28.8	28.8	28.8
7	38.3	38.2	38.3	38.3	27	29.3	29.3	29.2	29.3
8	38.1	38.0	38.1	38.1	28	29.2	29.4	29.2	29.2
9	37.6	37.5	37.6	37.6	29	29.2	29.1	29.1	20.1
10	36.0	35.9	35.9	35.9	30	29.3	29.4	29.3	29.3
11	36.3	36.4	36.3	36.3	31	29.3	29.1	29.1	29.1
12	36.5	36.5	36.5	36.5	32	28.9	28.8	28.7	28.8
13	36.6	36.5	36.6	36.6	33	28.7	28.6	28.7	28.7
14	36.7	36.6	36.6	36.6	34	30.6	30.7	30.7	30.7
15	36.6	36.7	36.7	36.7	35	32.2	32.2	32.2	32.2
16	36.5	36.4	36.4	36.4	36	32.9	32.9	32.9	32.9
17	36.4	36.3	36.4	36.4	37	33.8	33.8	33.8	33.7
18	36.1	36.2	36.1	36.1	38	36.1	36.1	36.1	36.1
19	37.1	37.0	37.1	37.1	39	37.0	36.8	36.9	36.9
20	36.0	36.0	35.9	36.0					

Table S.9: Experimental temperature data on the upper specimen,
 $h/l=2.0$, $F=294N$; T , °C

Round TC#	1	2	3	Ave.	Round TC#	1	2	3	Ave.
1	41.5	41.3	41.5	41.5	18	43.9	43.8	43.7	43.8
2	41.7	41.7	41.7	41.7	19	48.5	48.5	48.5	48.5
3	41.9	41.8	41.9	41.9	20	55.2	55.2	55.2	55.2
4	42.0	42.0	42.1	42.0	21	61.9	61.9	61.7	61.9
5	42.1	42.1	42.2	42.1	22	68.7	68.8	68.7	68.7
6	42.0	42.0	42.0	42.0	23	68.8	68.8	68.8	68.8
7	41.9	41.9	41.8	41.9	24	68.6	68.7	68.7	68.7
8	41.6	41.6	41.5	41.6	25	68.4	68.4	68.5	68.5
9	41.4	41.4	41.2	41.4	26	68.2	68.2	68.2	68.2
10	43.9	43.9	43.6	43.9	27	68.4	68.4	68.3	68.3
11	43.9	43.7	43.8	43.8	28	68.6	68.5	68.7	68.6
12	44.0	44.0	43.9	44.0	29	68.8	68.7	68.7	68.7
13	44.1	44.1	44.2	44.1	30	68.7	68.7	68.6	68.6
14	44.1	44.2	44.2	44.2	31	61.9	61.9	61.8	61.9
15	44.1	44.1	44.2	44.1	32	55.2	55.2	55.1	55.2
16	44.0	44.0	44.0	44.0	33	48.5	48.6	48.5	48.5
17	44.0	44.1	44.0	44.0					

Table 5.10: Experimental temperature data on the lower specimen,
 $h/l=2.0$, $F=294N$; T , °C

Round TC#	1	2	3	Ave.	Round TC#	1	2	3	Ave.
1	38.0	38.0	38.0	38.0	21	34.0	34.1	34.0	34.0
2	38.5	38.5	38.6	38.5	22	33.2	33.2	33.3	33.3
3	38.8	38.7	38.8	38.8	23	32.5	32.5	32.5	32.5
4	39.0	39.0	39.1	39.0	24	31.0	31.0	30.9	31.0
5	39.0	39.0	39.0	39.0	25	28.9	28.9	28.9	28.9
6	39.0	39.0	38.2	39.0	26	29.0	29.0	28.9	29.0
7	38.7	38.8	38.7	38.7	27	29.5	29.4	29.3	29.4
8	38.5	38.4	38.5	38.5	28	29.4	29.4	29.4	29.4
9	38.1	38.0	38.1	38.1	29	29.4	29.3	29.3	29.3
10	36.4	36.5	36.5	36.5	30	29.5	29.4	29.4	29.4
11	36.8	36.8	36.8	36.8	31	29.6	29.6	29.5	29.6
12	37.0	37.0	37.0	37.0	32	29.0	29.0	29.1	29.0
13	37.2	37.3	37.2	37.2	33	28.8	28.8	28.7	28.8
14	37.2	37.1	37.1	37.1	34	31.1	31.1	31.0	31.1
15	37.1	37.2	37.2	37.2	35	32.5	32.4	32.5	32.5
16	37.0	37.1	37.2	37.1	36	33.3	33.3	33.2	33.3
17	36.7	36.5	36.5	36.5	37	34.0	34.0	34.0	34.0
18	36.4	36.4	36.4	36.4	38	36.3	36.3	36.3	36.3
19	37.0	37.0	37.1	37.0	39	36.9	36.8	36.8	36.8
20	36.3	36.4	36.4	36.4					

Table 5.11: Experimental temperature data on the upper specimen,
 $h/l=2.0$, $F=882N$; T , °C

Round TC#	1	2	3	Ave.	Round TC#	1	2	3	Ave.
1	41.2	41.2	41.2	41.2	18	43.5	43.6	43.5	43.5
2	41.4	41.4	41.5	41.4	19	48.2	48.2	48.4	48.2
3	41.6	41.6	41.7	41.6	20	55.0	55.0	54.9	55.0
4	41.8	41.7	41.8	41.8	21	61.8	61.7	61.7	61.7
5	41.8	41.8	41.8	41.8	22	68.7	67.9	68.7	68.7
6	41.7	41.6	41.7	41.7	23	68.8	68.8	68.8	68.8
7	41.5	41.5	41.5	41.5	24	68.6	68.6	68.6	68.6
8	41.4	41.4	41.5	41.4	25	68.3	68.3	68.3	68.3
9	41.1	41.1	41.1	41.1	26	68.2	68.2	68.2	68.2
10	43.6	43.7	43.7	43.7	27	68.3	68.3	68.3	68.4
11	43.7	43.7	43.8	43.7	28	68.5	68.6	68.6	68.6
12	43.8	43.8	43.8	43.8	29	68.7	68.7	68.9	68.7
13	43.9	43.8	43.9	43.9	30	68.7	67.9	68.8	68.8
14	43.9	43.8	43.8	43.8	31	61.9	61.9	61.7	61.7
15	43.8	43.8	43.7	43.8	32	55.0	55.0	55.1	55.0
16	43.8	43.7	43.9	43.8	33	48.3	48.4	48.3	48.3
17	43.6	43.6	43.7	43.6					

Table 5.12: Experimental temperature data on the lower specimen,
 $h/l=2.0$, $F=882N$; T , °C

Round TC#	1	2	3	Ave.	Round TC#	1	2	3	Ave.
1	38.1	38.1	38.2	38.1	21	34.1	34.1	34.2	34.1
2	38.7	38.6	38.7	38.7	22	33.4	33.4	33.4	33.4
3	39.0	39.0	38.9	39.0	23	32.6	32.7	32.6	32.6
4	39.1	39.1	39.2	39.1	24	31.1	31.2	30.9	31.1
5	39.2	39.2	39.2	39.2	25	29.0	29.0	29.1	29.0
6	39.1	39.2	39.1	39.1	26	29.1	29.0	29.1	29.1
7	39.0	39.0	38.9	39.0	27	29.6	29.6	29.5	29.6
8	38.7	38.6	38.6	38.6	28	29.5	29.5	29.4	29.5
9	38.0	38.0	38.0	38.0	29	29.5	29.5	29.5	29.5
10	36.5	36.5	36.5	36.5	30	29.6	29.7	29.7	29.7
11	36.9	36.8	36.8	36.8	31	29.6	29.6	29.7	29.6
12	37.2	37.1	37.2	37.2	32	29.0	28.9	28.9	28.9
13	37.3	37.2	37.3	37.3	33	29.0	29.0	29.1	29.0
14	37.4	37.4	37.3	37.4	34	31.2	31.2	31.3	31.2
15	37.4	37.5	37.4	37.4	35	32.7	32.6	32.6	32.6
16	37.3	37.2	37.2	37.2	36	33.4	33.5	33.4	33.4
17	36.9	36.9	36.8	36.9	37	34.1	34.1	34.2	34.1
18	36.5	36.4	36.4	36.4	38	36.4	36.4	36.4	36.4
19	37.6	37.7	36.8	37.7	39	37.5	37.6	37.6	37.6
20	36.5	36.6	36.5	36.5					

Table 5.13: Temperature distribution below the heated surface,
 $h/l=0.5$; $T, ^\circ\text{C}$

Position Load F, N	1	2	3	4	5	Average
98	67.0	67.2	67.6	67.7	67.6	67.4
294	66.9	67.2	67.5	67.6	67.5	67.3
882	66.9	67.1	67.4	67.6	67.5	67.3

Table 5.14: Temperature distribution below the heated surface,
 $h/l=2.0$; $T, ^\circ\text{C}$

Position Load F, N	1	2	3	4	5	Average
98	68.2	68.4	68.7	68.8	68.8	68.6
294	68.1	68.2	68.5	68.8	68.8	68.5
882	68.1	68.3	68.7	68.8	68.7	67.5

Table 5.15: Temperature drop caused by the interface,
 $h/l=0.5$; ΔT , °C

Position Load F, N	1	2	3	4	5	Average
98	2.0	2.5	3.0	3.4	3.6	2.9
294	0.4	0.8	1.3	1.7	2.6	1.4
882	0.1	0.1	0.3	0.6	0.3	0.3

Table 5.16: Temperature drop caused by the interface,
 $h/l=0.5$; ΔT , °C

Position Load F, N	1	2	3	4	5	Average
98	2.0	1.9	1.9	1.7	1.8	1.8
294	0.7	0.6	0.7	0.7	1.0	0.7
882	0.2	0.3	0.1	0.1	0.4	0.2

Table 5.17: Mechanical contact pressure distribution of nodes along the interface,
 $h/l=0.5$; p_{mech} , kPa

Node Load F, N	1	2	3	4	5	6	Average
98	783	731	620	487	368	560	592
294	2348	2190	1858	1461	1102	1675	1771
882	7042	6570	5572	4381	3306	5023	5316

Table 5.18: Mechanical contact pressure distribution of nodes along the interface,
 $h/l=2.0$; p_{mech} , kPa

Node Load F, N	1	2	3	4	5	6	Average
98	546	548	554	571	620	693	589
294	1631	1637	1654	1709	1850	2074	1759
882	4885	4897	4960	5113	5552	6202	5268

Table 5.19: Mechanical contact pressure distribution of elements along the interface,
 $h/l=0.5$; p_{mech} , kPa

Element Load F, N	1	2	3	4	5	Average
98	756	676	554	428	465	576
294	2348	2190	1858	1461	1103	1787
882	7042	6570	5572	4381	3306	5373

Table 5.20: Mechanical contact pressure distribution of elements along the interface,
 $h/l=2.0$; p_{mech} , kPa

Element Load F, N	1	2	3	4	5	Average
98	547	551	563	596	657	582
294	1634	1645	1682	1800	1962	1740
882	4891	4928	5036	5332	5877	5213

Table 5.21: Combined mechanical and thermal contact pressure distribution of nodes along the interface, $h/l=0.5$; p_c , kPa

Node Load F, N	1	2	3	4	5	6	Average
98	568	539	408	435	727	943	604
294	2288	2253	1792	1642	1261	1169	1735
882	7418	6675	5932	4472	4005	2992	5249

Table 5.22: Combined mechanical and thermal contact pressure distribution of nodes along the interface, $h/l=2.0$; p_c , kPa

Node Load F, N	1	2	3	4	5	6	Average
98	386	409	475	587	760	1106	616
294	1250	1274	1298	1721	1984	2901	1738
882	4489	4606	4822	5200	6068	7517	5450

Table 5.23: Combined mechanical and thermal contact pressure distribution of elements along the interface, $h/l=0.5$; p_c , kPa

Element Load F, N	1	2	3	4	5	Average
98	554	473	421	581	835	577
294	2271	2022	1717	1432	1196	1727
882	7046	6303	5202	4239	3499	5258

Table 5.24: Combined mechanical and thermal contact pressure distribution of elements along the interface, $h/l=2.0$; p_c , kPa

Element Load F, N	1	2	3	4	5	Average
98	375	442	531	673	933	591
294	1262	1286	1607	1852	2442	1690
882	4547	4655	5952	5634	6792	5317

Table 5.25: Thermal stress distribution along the interface,
 $h/l=0.5$; s_{θ} , kPa

Element Load F, N	1	2	3	4	5	Arith. Mean
98	-204	-203	-132	153	370	-15.7
294	-77.4	-99.0	-141	-29.4	93.1	-50.0
882	4.0	-267	-370	-142	189	-118

Table 5.26: Thermal stress distribution along the interface,
 $h/l=2.0$; s_{θ} , kPa

Element Load F, N	1	2	3	4	5	Arith. Mean
98	-172	-109	-31.3	77.4	276	8.8
294	-469	-458	-172	25.5	382	-138
882	-344	-273	-84.3	302	933	107

Table 5.27: The effect of thermal stress on mechanical pressure along the interface, $h/l=0.5$;

Element Load F, N	1	2	3	4	5	Average
98	33.8%	33.7%	22.0%	25.4%	61.5%	35.1%
294	4.3%	5.5%	7.8%	1.6%	5.1%	4.9%
882	0.0%	4.9%	6.8%	2.6%	3.5%	3.4%

Table 5.28: The effect of thermal stress on mechanical pressure along the interface, $h/l=2.0$;

Element Load F, N	1	2	3	4	5	Average
98	28.5%	18.0%	5.20%	12.8%	45.9%	22.4%
294	26.0%	25.3%	9.5%	1.4%	21.1%	17.2%
882	6.3%	5.0%	1.6%	5.6%	17.2%	7.1%

Table 5.29: First assumption of thermal conductivity distribution along the interface,
 $h/l=0.5$; k , $W/m^{\circ}C$

Element Load F, N	1	2	3	4	5	Average
98	36.9	34.6	29.4	26.5	52.2	35.9
294	50.0	46.9	39.0	32.2	29.0	40.7
882	52.8	49.4	41.0	36.2	31.6	42.9

Table 5.30: First assumption of thermal conductivity distribution along the interface,
 $h/l=2.0$; k , $W/^{\circ}C$

Element Load F, N	1	2	3	4	5	Average
98	23.0	23.0	26.0	33.0	49.0	30.8
294	42.5	42.7	44.5	48.5	60.9	48.7
882	50.6	51.1	52.4	56.1	63.9	54.8

Table 5.31: Thermal conductivity distribution along the interface,
 $h/l=0.5$; k , $W/m^{\circ}C$

Element Load F, N	1	2	3	4	5	Average
98	31.5	30.2	27.4	26.4	34.4	30.0
294	49.0	47.5	44.0	41.0	39.6	44.2
882	53.7	53.5	52.0	50.7	49.3	51.8

Table 5.32: Thermal conductivity distribution along the interface,
 $h/l=2.0$; k , $W/^{\circ}C$

Element Load F, N	1	2	3	4	5	Average
98	26.3	27.1	28.1	29.5	36.0	29.4
294	40.2	40.8	43.0	46.0	47.7	43.5
882	49.1	50.4	51.2	52.4	53.4	51.3

Table 5.33: Thermal contact resistance distribution along the interface,
 $h/l=0.5$; R_c , m^2C/kW

Element Load F, N	1	2	3	4	5	Average
98	0.067	0.073	0.090	0.064	0.053	0.069
294	0.010	0.013	0.021	0.030	0.034	0.022
882	0.001	0.001	0.004	0.006	0.009	0.004

Table 5.34: Thermal contact resistance distribution along the interface,
 $h/l=2.0$; R_c , m^2C/kW

Element Load F, N	1	2	3	4	5	Average
98	0.098	0.092	0.086	0.077	0.047	0.080
294	0.032	0.030	0.024	0.016	0.013	0.023
882	0.010	0.007	0.005	0.003	0.001	0.005